Continuum analysis of sharp indentation experiments in metallic materials: theory and finite element simulations

Marta Mata Burgarolas

Supervisor: Jorge Alcalá Cabrelles

Department of Materials Science and Metallurgical Engineering

Universitat Politècnica de Catalunya

December 2004

A la meva mare,

i a les nenes.

A la memòria del meu pare.

Agraïments

El meu sincer agraïment pel Professor Jorge Alcalá per guiar-me com a mentor i com a amic. El teu entusiasme, la perseverància, la paciència, els consells, i les llargues hores de converses han estat clau per arribar fins aquí. Gràcies Jorge.

Sens dubte, gràcies Ovidi per haver-me acompanyat durant el viatge i ajudat en les turbulències del doctorat. També a la resta de nois de la Work Station -Jan, Sylvain, Guillermo, Marcos, i tots els que han compartit el nostre castell- , ningú com vosaltres m'ha animat els dies grisos; sempre he trobat un amic darrera de cada pantalla :-). M'heu alegrat l'existència. I gràcies Juangra per la clau d'aquesta tesi, no sé què hauria fet sense el teu arxiu d'input. I no em podria deixar el Prof. Enrique Fernández, que amablement ha compartit" el seu despatx amb mi tantes hores durant quatre anys; amb més gent com tu el món aniria molt millor.

També voldria agrair a tots el components del grup de Fatiga i Fractura del pel seu suport i el seu afecte, especialment al Prof. Marc Anglada que sempre està allà per nosaltres. Però he de reconèixer que aquest doctorat no hauria sigut el mateix si no fos per molta gent del departament que m'ha envoltat durant aquests anys. Gràcies Àngels per la teva ajuda durant les meves breus estades al laboratori, María, Jessica, Víctor, Nayar, Sergio, Elena, Luca, Griselda, Prof. Jordi Tartera, Ferran, i un llarg etcètera en el qual hi esteu tots i cadascun de vosaltres.

Finalment donar les gràcies més profundes a la meva mare, la Núria, l'Imma i l'Eulàlia per donar-me el vostre suport incondicional, i l'Alexandra i a la

Claudia per regalar-me la seva alegria perenne. En vosaltres he trobat la força i l'empenta per seguir endavant fins l'últim moment, no només com a mare i germanes, sinó com les millors conselleres i editora (gràcies Eu) que mai hauria pogut tenir.

Molta gent ha estat al meu costat durant l'escriptura d'aquesta tesi, i em temo que no us ho puc agrair com pertoca. En resposta al mal humor, una broma. Per una mala cara, un somriure. A canvi d'un mal moment, una abraçada. Gràcies als qui us sentiu al·ludits per haver-me animat durant les hores baixes.

Voldria agrair el suport econòmic del Ministerio de Educación, Cultura y Deporte per haver-me atorgat la beca de Formació de Personal Universitari. Aquesta tesi s'ha realitzat amb finançament del Ministerio de Ciencia y Tecnología en el marc dels projectes MAT 2002-00368 i PETRI No. 95-0763.OP.

Abstract

This thesis provides a sound physical rationale to the analysis of indentation experiments. First, it extends the concept of the contact deformation regimes to metallic materials exhibiting strain hardening effects. The main outcome along these lines is the development of a contact deformation map, which predicts the active contact regime for a given combination of mechanical properties of the indented material. The map is based upon extensive finite element simulations, elucidating the fundamental features of the plastic flow patterns and plastic zone shape in metals deforming within the elasto-plastic and the fully plastic contact regimes. General relations are then found between hardness and the amount of material pileup or sinking-in developing at the contact boundary with uniaxial mechanical properties. These relations are central in devising a novel methodology for mechanical property extraction based on direct assessments of the imprint's topography and instrumented indentation applied load (P)-penetration depth (h_{s}) curves. Then, a general framework to the analysis of frictional effects between indenter and material is developed. This knowledge allows us to extend the aforementioned methodology when dealing with frictional contacts. Finally, a detailed analysis is made on the analogy between indentation experiments and the problem of the expansion of a spherical cavity. Closed-form solutions for the expansion of the cavity in strain hardening solids are first derived. The finite element simulations are used to provide a strict parametrical analogy between contact variables and those from expanding cavity formulations. The main outcome of this analysis is the development of new formulations

which evaluate the plastic zone size in sharp indentation experiments of strain hardening metallic materials.

Contents

List of Figures

List of Tables

Motivation

There is an increasing interest to design materials whose microstructures are tailored for mechanical functionality. Fabrication of composite structures comprising, for instance, multilayers, homogeneous and compositionally graded coatings, requires a detailed knowledge of the mechanical response of their constituents to ensure that the overall structure fulfills the required macroscopic behavior. Processing of such new materials fosters scientific and technological developments on specific techniques for the assessment of the mechanical response at local (microstructural) scales. Furthermore, the capacity for evaluating the mechanical response using small volumes of material plays an important role when integrity assessments of structural components are at issue.

Uniaxial tests continue to be widely used in the evaluation of the mechanical response of materials. However, when it comes to characterize small volumes of material, these tests are difficult to perform so that one has to recourse to alternative procedures. Indentation experiments allow one to probe the local mechanical response of the material when it is pressed against an indenter of known shape. The magnitude of the applied load or, alternatively, the penetration depth of the indenter into the material, sets the length scale under evaluation. Thus, one can potentially probe the behavior of single grains and, by increasing applied load, evaluate the global mechanical response of the solid.

Indentation experiments are extremely dependent upon indenter's geometry (a blunt sphere or sharp three- or four-sided pyramidal tips are the most commonly used shapes). The deformation state induced by the indenter may thus undergo different stages; namely, elastic deformation, elasto-plastic transition, and fully plastic regime depending

on the mechanical properties of the material and tip sharpness. While spherical indenters are instrumental in studying the evolution through these stages of deformation, sharp tips (such as cones and pyramids) induce a severe geometrically-similar deformation state which is in steady-state during complete load application.

In indentation experiments, the magnitude of the applied load determines the volume of material under study. As the results depend upon such volume, one can readily classify indentation experiments according to the applied load or penetration depth. That is, nano-indentation covers the low-load range (applied loads usually smaller than 500 mN), where the active deformation mechanisms are dislocation emission and discrete dislocation glide, and the imprint is fully embedded within a single grain. The micro-indentation range is reached for applied loads of, say, between 0.5 N to less than 20 N, where the deformation mechanisms in the material are mesoscopic, involving interaction of a small number of grains or constituents. Finally, at the macro-indentation range (loads typically greater than 100 N), one can evaluate the global response of the indented material as a continuum, where deformation is averaged over a representative number of micro-constituent units.

Although knowledge of the aforementioned length scales is central to the analysis of indentation experiments, the present work was undertaken at a point where considerable work was still needed to understand indentation experiments even within the macroscopic (continuum) level. Computational power was becoming increasingly available as to allow one to perform systematic analysis of the contact response of materials with distinct mechanical properties. Also, with the advent of instrumented indentation techniques (which allowed one to obtain continuous recordings of applied load (P)-penetration depth (h_{s}) curves down to the pico-Newton) as well as with the excitement brought by emerging fields in materials science which required tools to perform local assessments of mechanical properties, indentation was becoming again a scientifically appealing subject. While research opportunities were clear, a solid foundation to the analysis of indentation experiments was already available because (i) contact mechanics was a mature area, and (ii) a large body of experimental work was available. In light of

these considerations, we decided to perform computational analysis of indentation experiments backed by some experimental work, which we hoped would provide new insights into a number of fundamental issues that, over the years, eluded analysis with more conventional tools. In particular, we sought to obtain general "hardness equations" which, in the line of the pioneering work conducted by Tabor in the 1950s, allow one to predict mechanical properties from indentation experiments. Since an important drawback in instrumented indentation is that it does not account for the deformation around the contact boundary (i.e., the development of pileup or sinking-in of the material), we had the belief that this piece of information might become central to mechanical property extractions from indentation experiments. This feeling came out to be correct.

This thesis is arranged following a deductive approach, which illustrates the way present research came to fruition. Basic concepts in the application of contact mechanics to indentation are first given §1. The objectives of the work are lain in §2. §3 is devoted to describe the computational and experimental tools used in this investigation. The remaining chapters provide discussions on the topics constituting the scientific backbone of our findings. §4 gives an extensive description on the plastic flow features developing underneath a sharp indenter. The results allow us to build a contact deformation map which extends the prior work conducted by Johnson in the 1970s to the case of strain-hardening solids. Based upon these findings, a comprehensive methodology for mechanical property extractions from indentation experiments is devised in §5. The influence of friction upon the current analysis is covered in §6. A fundamental approach is regained in §7, which deals with the development of a general equation for predicting the plastic zone size around sharp indentations. Some critical considerations are made in this chapter regarding the pioneering work conducted, among others, by Johnson and by Hill, on the analogy between indentation and the inflation of a spherical cavity.

Chapter 1

Introduction

The contact response between solids of different nature has long been a topic of study from theoretical and experimental standpoints. The theoretical background to the analysis of indentation experiments is strongly rooted in the field of Contact Mechanics. This discipline provides a description of the stress and strain fields underneath the indenter as well as of the contact pressure distribution existing between the indenter and the material. In short, contact mechanics gives a mechanistic interpretation of the intrusion of an indenter into a solid which is extremely relevant to the analysis of experimental results. Attention is given in this chapter to the parameters from indentation and contact mechanics describing the salient features of the contact response.

1.1 Aspects from indentation and contact mechanics

Since the early work by Hertz on the elastic contact between two spherical bodies [41; 46], considerable research efforts have been devoted to study the behavior of a wide range of solids brought into contact against different indenter geometries. Contact mechanics thus has evolved considerably, providing general descriptions on the link between indentation parameters and mechanical properties. For instance, Sneddon [70] derived a theoretical framework for the contact response attained between an elastic solid and axisymmetric punches (e.g., sphere, cone, or flat-ended punch). He obtained correlations of indentation parameters (such as pressure distribution p, hardness H, and the amount of surface

deformation around the indenter) in terms of the elastic properties of the solid and the indenter. On the other hand, the slip-line field theory allowed one to examine the contact response of rigid–*perfectly-plastic* solids. Characterization of the indentation response of elastic–perfectly-plastic solids was undertaken by Johnson [47] through the analogy between indentation and the expansion of a spherical cavity, which was originally conceived in [10; 21; 28; 42; 46]. In spite of the limitations in such an analogy, the results from Johnson's analysis provided important guidelines to the analysis of indentation experiments. Alternatively, a powerful tool to examine the contact response of elasto-plastic materials is found in the similarity approach adopted in [6; 11; 14; 43; 62]. This approach is illustrated in the final part of this chapter.

1.1.1 Indentation parameters

The contact response in a conventional hardness test is described with two quantities: hardness, and the upwards or downwards deformation that develops at the periphery of the imprint (i.e., the occurrence of the so-called pileup or sinking-in of material).

Hardness (H) is calculated as the ratio between the applied load (P) and the projected area of the residual imprint (A), namely,

$$H = \frac{P}{A} \ . \tag{1.1}$$

Although hardness is a rather elusive concept, the above equation suggests that it is indicative of the resistance of the material to deform plastically under the action of the indenter.

The deformation that is induced at the contact boundary is assessed through inspection of the imprint's topography. Bulging at the sides of a pyramidal imprint indicates development of material pile-up whereas pincushion effects at the imprint suggests attainment of sinking-in, Fig. 1.1. To estimate the amount of pileup and sinking-in, one may recourse to techniques such as profilometry, interferometrical microscopy, or atomic force microscopy (AFM) which provide a topographical map the residual imprint. A simple parameter quantifying the amount of surface deformation is

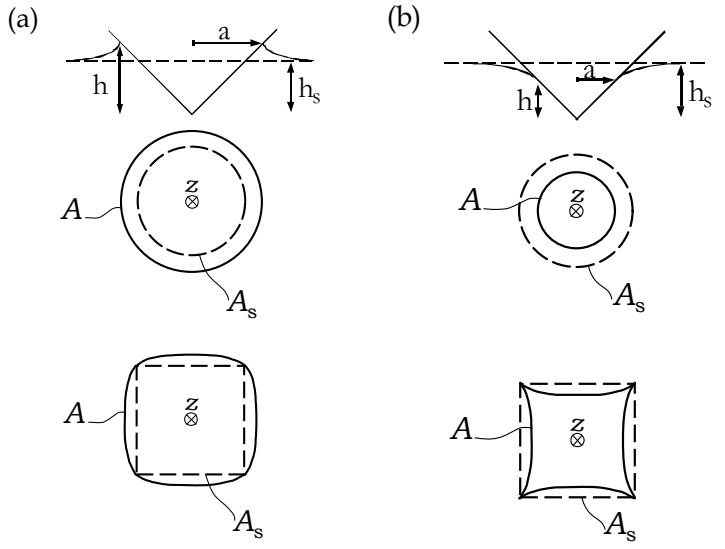

Figure 1.1: Schematic of the (a) piling-up and (b) sinking-in responses and associated nomenclature.

$$\alpha = \frac{A}{A_s} \tag{1.2}$$

where A is the true projected contact area and A_s is the geometrical area that measures the imprint as if the surface would remain flat (i.e., ignoring the development of pileup or sinking-in), see Fig.1.1. By simple geometrical arguments, A_s is determined as

$$A_s = f {h_s}^2 \tag{1.3}$$

where h_s the penetration depth of the indenter, as measured from the undeformed surface of the material, and f a geometrical factor which depends on the indenter's shape ($f =$ 24.5 for the Vickers four-sided indenter; 24.562 for the Berkovich trigonal indenter; and $f = \pi \tan^2\theta$ for a cone with arbitrary half-apex angle θ). By virtue of the axisymmetry of the conical tip, it follows that it is possible to substitute A_s by A and h_s by h in Eq. (1.3). Thus, in accordance with Eq. (1.2), one can measure the amount of pileup

or sinking-in using the true height of the contact surface (h) and the penetration depth from the undeformed surface to the indenter's tip (h_s). That is,

$$\sqrt{\alpha} = \frac{h}{h_\mathrm{s}} \ . \tag{1.4}$$

Pileup occurs when $\alpha > 1$, and sinking-in develops for $\alpha < 1$.

Notice that Eq.(1.2) and Eq.(1.4) are equivalent because the apical angle in a conical indentation remains constant around the z-axis so that pileup and sinking-in are homogeneous throughout the contact boundary. Vickers and Berkovich pyramidal indentations, however, have uneven heights along the periphery as a result of the different constraints imposed to the material by the sharp edges of the indenter and its sides. Hence, α varies throughout the contact boundary. In such cases, it becomes necessary to estimate a mean value for the amount of surface deformation through the ratio of contact areas Eq.(1.2) rather than with Eq.(1.4).

Although the occurrence of the above surface deformation modes (i.e., pileup and sinking-in) is indicative of the mechanical response of the material, α cannot be taken as an intrinsic material property because, in the same way as hardness, it is the result of a combination of elastic and plastic uniaxial mechanical properties. Hardness H and surface deformation parameter α are also dependant of the indenter's geometry. It is known that perfectly-elastic solids exhibit large sinking-in effects ($\alpha = 0.41$), while rigid–perfectly-plastic materials tend to develop pile-up [46; 70]. Investigations by Matthews [61] and Alcalá *et al.* [3] also demonstrated that the amount of surface deformation is linked to the strain hardening capacity of the solid. Materials exhibiting large strain-hardening effects (where constant n in Eq. (A.21) is large) undergo sinking-in, whereas pileup develops when the material presents little strain hardening effects ($n \to 0$, see Appendix A).

Instrumented indentation experiments evaluate the *evolution* of the contact response along the loading and the unloading stages of the experiment, providing a complementary knowledge to that given through measurement of hardness H and parameter α. This

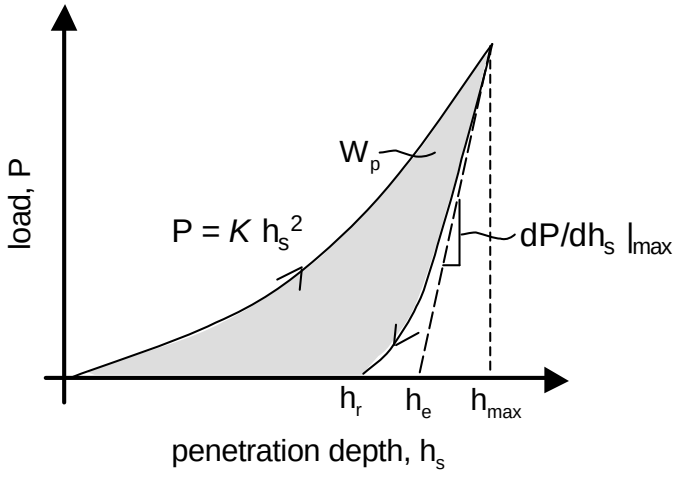

Figure 1.2: Schematic of an instrumented indentation applied load (P)–penetration depth (h_s) curve. Arrows indicate the loading and unloading paths. Note that the material exhibits plastic deformation because $h_\mathrm{r} \neq 0$. Variables describing the curve are also given in the figure (see Section 5.5).

technique thus provides continuous recordings of applied load (P)–penetration depth (h_s) curves of the indenter against the material (see Fig. 1.2).

Analysis of an instrumented indentation P–h_s curve provides an indication of the the elastic and plastic responses of the material. The elastic response, characterized through the Young's modulus E, can be directly obtained from the early unloading stage [65; 70]. The following closed-form solution for elastic contacts with punches of arbitrary shape is used for the purpose of extracting Young's modulus:

$$E^* = \frac{1}{c^* \sqrt{A_\mathrm{max}}} \frac{\mathrm{d}P}{\mathrm{d}h_\mathrm{s}}\bigg|_{h_\mathrm{max}} \quad ; \tag{1.5}$$

with

$$E^* = \left(\frac{1-{\nu_\mathrm{m}}^2}{E_\mathrm{m}} + \frac{1-{\nu_\mathrm{i}}^2}{E_\mathrm{i}} \right)^{-1} \quad , \tag{1.6}$$

where E_m and ν_m are the Young's moduli and the Poisson's ratio of the material, and E_i and ν_i are the Young's moduli and the Poisson's ratio of the indenter, $\mathrm{d}P/\mathrm{d}h_\mathrm{s}$ is the slope of the P–h_s curve in the first part of the unloading segment, Fig. 1.2, c^* is a geometrical constant that depends on indenter's geometry ($c^* = 1{,}142$ for the Vickers indenter; 1,167 for the Berkovich indenter; and 1.128 for a cone with 70.3° of included half-angle), and A_max is the true contact area A at maximum load [3; 71]. Obviously, since only A_s and not A is inferred from the P–h_s curve, an important limitation in instrumented indentation experiments becomes evident as the use of this formulation requires a prior knowledge on the amount of pileup or sinking-in. The so-called Oliver and Pharr method provides an empirical approach for finding true contact area A from penetration depth h_s measurements [65; 71].

The loading segment of the P–h_s curve reflects the elasto-plastic response of the material. In the absence of length scales which may be induced, for instance, by microstructural features, the relation between applied load and penetration depth is prescribed through Kick's law

$$P = K {h_\mathrm{s}}^2 \ , \tag{1.7}$$

where K is a material constant which, through equations (1.3), (1.1) and (1.7), is related to hardness H and surface deformation parameter α as

$$K = fH\alpha \ . \tag{1.8}$$

This relation demonstrates the link between parameter K from instrumented indentation experiments and hardness H. Thus, it is considered that the contact response is completely defined by a reduced number of independent variables: hardness H, surface deformation parameter α, and unloading slope $\mathrm{d}P/\mathrm{d}h_\mathrm{s}$. The first two parameters (H and α) result from the elasto-plasticity developing at the contact surface (that is, they are anticipated to be functions of yield strength σ_ys, hardening coefficient n, and Young's modulus E), while $\mathrm{d}P/\mathrm{d}h_\mathrm{s}$ only concerns the elastic behavior of the indented material.

The above discussion opens the question of whether it is possible to gain a complete knowledge of uniaxial mechanical properties through P–h_s curves analysis or, alternatively, through measurements of H and α. To answer this question, it becomes necessary to derive specific correlations between independent contact parameters and uniaxial mechanical properties (i.e., $H = H(E, \sigma_\mathrm{ys}, n)$ and $\alpha = \alpha(E, \sigma_\mathrm{ys}, n)$). Along these lines, several investigations have been published focusing on novel methodologies for mechanical property extraction through analysis of indentation experiments. [2; 3; 4; 25; 26; 30; 32; 39; 50; 51; 69; 76].

1.1.2 General background

A central quantity in contact mechanics is the pressure distribution p at the contacting interface. When two solids become in contact, a set of punctual forces are induced along the interface. By definition, pressure is given by the ratio between the applied load and the load-bearing contact area. Therefore, such local forces divided by the corresponding load-bearing surface differentials give the overall contact pressure distribution. The schematic in Fig.1.3 shows a generic contact pressure distribution for conical indentation.

The geometry and mechanical properties of the contacting surfaces govern the pressure distributions. A remark is thus to be made regarding the assumption of the indenter

(a)

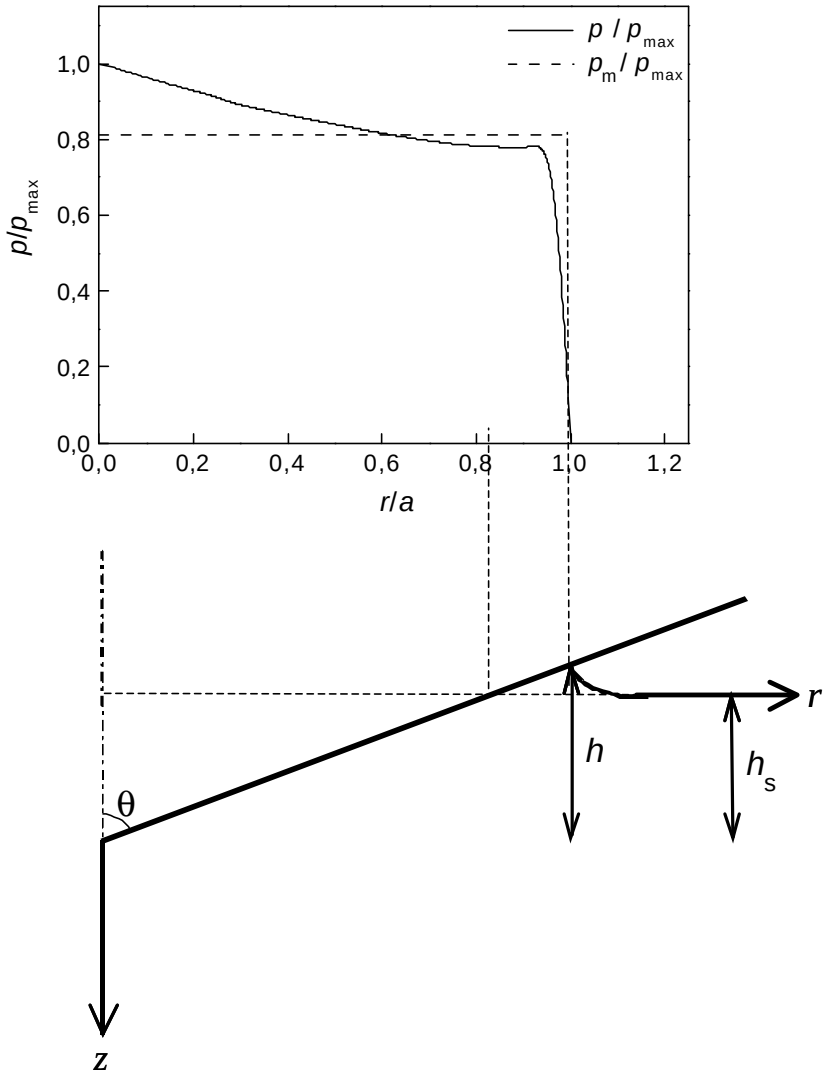
p / p_max
p_m / p_max
1,0
0,8
0,6
0,4
0,2
0,0
p/p_max
0,0
0,2
0,4
0,6
0,8
1,0
1,2
r/a
r
h
h_s
θ
z

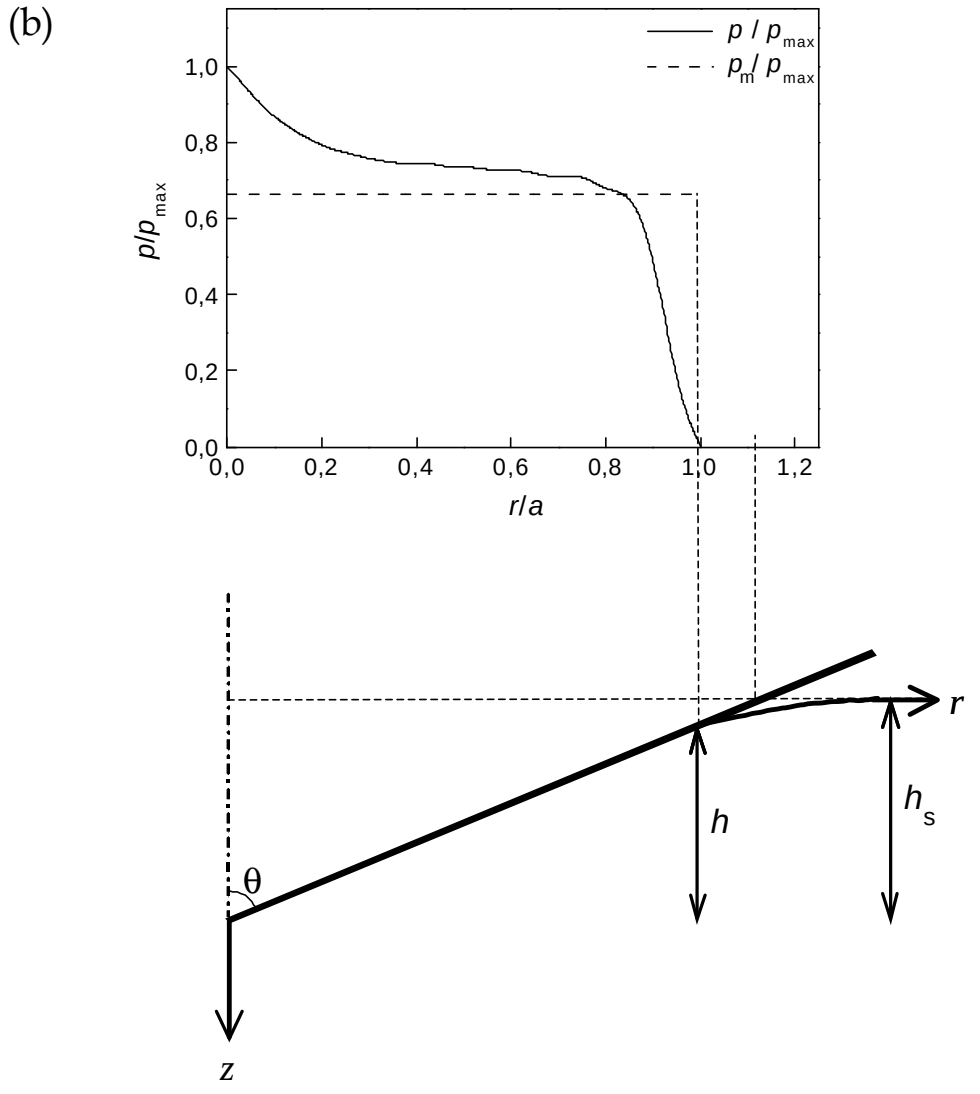

Figure 1.3: Normalized pressure distribution $p/p_{\max}$ and normalized mean pressure $p_{\mathrm{m}}/p_{\max}$ for cone indentations in (a) a solid undergoing pileup ($E = 200$ GPa, $\sigma_{\mathrm{ys}} = 100$ MPa, $n = 0.1$), and (b) a solid exhibiting sinking-in ($E = 70$ GPa, $\sigma_{\mathrm{ys}} = 400$ MPa, $n = 0.4$). These results are from the current finite element simulations described in §3.

being a rigid tip, where the mechanical properties influencing the contact response are taken to be exclusively those of the indented solid. While such an approximation is generally valid provided the indenter is a much harder solid than the indented material, indenter's deformation is still to be considered when a detailed analysis of the experiment is at issue (see Eq.(1.6), Section 1.1.1), [41].

Sneddon [70] thoroughly established governing relationships between indentation parameters and the *elastic* properties of the indenter and the material. Among other issues, Sneddon derived integral equations for the pressure distribution, and relationships between applied load and penetration depth of the indenter into the solid. He also provided celebrated analysis for the elastic recovery induced upon unloading (which is widely used in the assessment of instrumented indentation experiments, see Eq. (1.5) and the work by King [48]). The overall features of the pressure distribution in *elastic* contacts are shown in Figure 1.4, which illustrates the variation of normalized pressure distribution (p/p_{m}) as a function of the normalized contact radius (r/a) for a conical indenter whose semi-apical angle θ is 70.3° (where mean contact pressure p_{m} is the averaged value of the distribution through the contact surface). It is noted that pressure at $r/a = 0$ is infinite because the sharp tip of the cone introduces a mathematical singularity. Figure 1.4 is clearly different to that found for the elastic contact of a spherical body into a half-space, where the hertzian solution for p/p_{m} is a bounded quantity equal to 3/2 at $r/a = 0$ [41].

Linear elastic contact mechanics no longer applies when it comes to examine the contact response between a rigid indenter and a plastic solid. An approximation to this problem is obtained through the slip-line theory [42], which provides pressure distributions at the contacting surfaces. Notice that the slip-line method provides discrete values of stresses and contact pressures; however, explicit closed-form solutions cannot be derived on the basis of this theory. An important limitation of the slip-line theory is that it only applies to *rigid–perfectly-plastic* solids. Therefore, it allows one to evaluate the contact response in "highly plastic" solids, where such restriction is a sensible approximation.

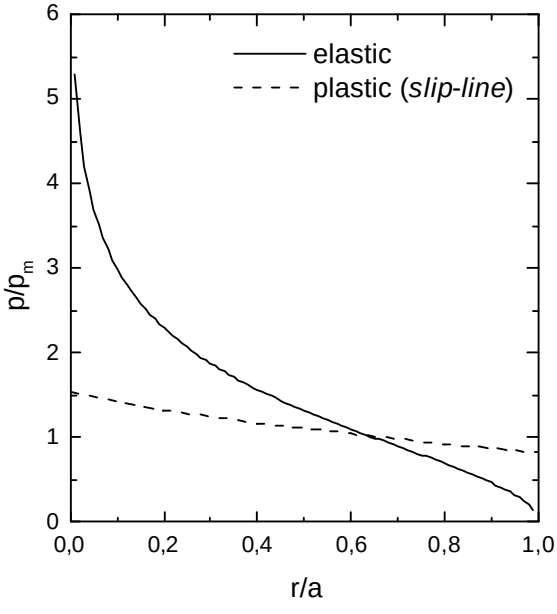

Figure 1.4: Normalized pressure distribution p/p_{m} for cone indentations in an elastic solid (solid line) and in a rigid–perfectly plastic solid (dashed line). The results pertain to a conical indenter with half-apex angle θ of 70°.

Figure 1.4 shows the normalized pressure distribution obtained through the slip-line analysis of conical indentation given in [55]. The same tendencies as in elastic contacts are preserved: (i) the pressure is distributed over the whole surface, which in such plastic solids includes the pileup region at the contact boundary, and (ii) the pressure is maximum at the indenter's tip, where in this case plastic flow removes the singularity of the stress field. It thus follows that while in elastic contacts the stress distribution gradually decays from infinite to almost zero, rigid–perfectly plastic solids exhibit a quasi-constant value of pressure from the indenter's tip to the pileup height, where pressure falls abruptly to zero.

In light of the ongoing discussion, it is important to bear in mind that although perfectly elastic solutions and slip-line analyses pertain to solids with extreme contact responses, the study of linear elastic–strain hardening plastic solids is out of the scope of these theories. Alternative techniques involving finite element simulations are however available to provide insights into such more realistic contact responses.

A key variable that characterizes the pressure distribution is its mean value p_{m}. Notice that such contact pressure exactly matches the definition of hardness provided in Section 1.1.1:

$$H \equiv p_{\mathrm{m}} = \frac{1}{A}\int_A p(\mathbf{s})\mathrm{d}\mathbf{s} \tag{1.9}$$

where A is the true projected contact area, and $\mathbf{s}$ is the surface differential supporting pressure $p(\mathbf{s})$. Hardness is thus linked to the mechanical properties of the indented solid. Integration of the pressure distribution obtained by Sneddon in elastic contacts leads to the following expression

$$H = p_{\mathrm{m}} = \frac{E\ \mathrm{cotan}\theta}{2(1-\nu^2)}\ , \tag{1.10}$$

where E is the Young's modulus and ν is the Poisson's ratio of the material, and θ is the semi-apical angle of the conical indenter. Alternatively, dimensional analysis readily suggests that hardness of rigid–perfectly plastic solids has to be proportional to the only material length scale of the problem. That is, the yield strength of the solid σ_{ys}. Hence,

$$H = p_{\mathrm{m}} = C_{\mathrm{sl}}\sigma_{\mathrm{ys}} \ , \tag{1.11}$$

where proportionality constant C_{sl} only depends on the geometry of the indenter in accordance to the slip-line analysis. For the conical indenter whose semi-angle $\theta = 70.3°$, constant C_{sl} is found to be 2.73 [55; 80], whereas for a wedge with the same angle C_{sl} = 3 [42].

Slip line analysis takes into account the fact that in most strain hardened metals, plastic flow extends outwards from the contact boundary leading to pileup effects. This result is due to the large capacity of these solids to accumulate plastic deformations, as $n = 0$ (see Fig. 1.5 and Eq. (A.21)).

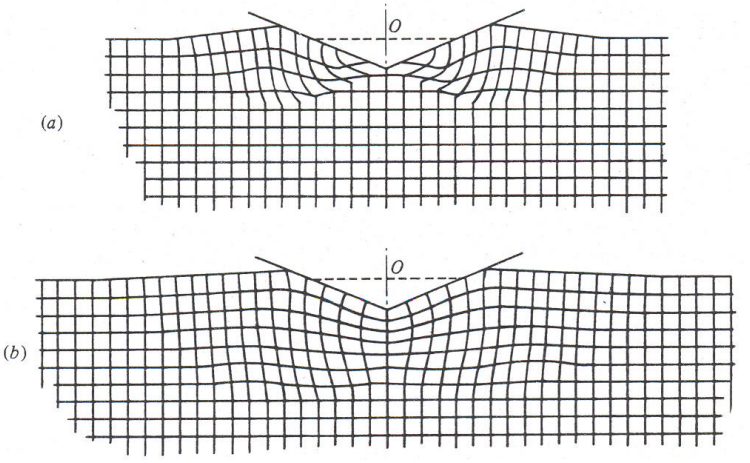

Figure 1.5: Deformation patterns induced with a blunt wedge in rigid–perfectly plastic solids for (a) frictionless contact conditions, and (b) adhesive contact conditions [from [46]].

The experimental work by Tabor indicated that, in the spirit of Eq.(1.11), there exists a simple relation between hardness and the uniaxial stress-strain response of *strain-hardening* metals [73]. An important concept introduced by Tabor is the existence of a material-independent *characteristic strain* ϵ_{r}, whose associated uniaxial stress level σ_{r} is proportional to hardness. That is,

$$H = p_{\mathrm{m}} = C\sigma_{\mathrm{r}} \ . \tag{1.12}$$

For a Vickers indenter, Tabor found that regardless of the material under analysis, characteristic strain ϵ_{r} was 0.08 and constant C was about 3. These values were obtained from experimental results in pure copper and mild steel, both in the annealed state and strain-hardened to different amounts.

It is emphasized that Tabor's equation holds true in the absence of strain hardening effects ($n = 0$), where Eq. (1.12) converges to the results of the slip line theory for *rigid*–perfectly plastic materials, Eq. (1.11). Notice that the validity of Tabor's approach pends on the concept of the characteristic strain. Due to the potential use of Eq.(1.12) in the evaluation of the uniaxial stress-strain curve, a debate on the general validity of such concept grew over the years. Along these lines, numerical and experimental studies focused on the determination of the plastic deformations induced at the periphery of the imprint, leading to inconsistent conclusions concerning the actual value of ϵ_{r} and its uniqueness. From experiments performed in copper, Chaudhri [22] advocated values of ϵ_{r} that ranged from 0.25 to 0.36 depending on the strain-hardening coefficient of the material. Finite element simulations of indentation experiments in highly plastic solids led to the conclusion that Tabor's equation was fulfilled when the characteristic strain was taken to be 0.29 [39; 50; 51]. Finite element simulations on a wide variety of solids obeying different mechanical responses showed that the characteristic strain was constant and equal to 0.10 while the value of C varied from 1.5 to 2.5 [27].

To take into account the combined influence of elasticity and plasticity in hardness values, an analogy between indentation and the problem of a spherical cavity expanding in an infinite medium was attempted by Bishop *et al.* [10]. Using Hill's governing equations for cavity inflation [42], experimental investigations of Vickers indentation [58] and wedge indentation [44] provided a correlation between hardness H, Young's modulus E, and yield strength σ_{ys}:

$$\frac{H}{\sigma_{\mathrm{ys}}} = A + B\ln\left(\frac{E}{\sigma_{\mathrm{ys}}}\right) \ , \tag{1.13}$$

where constants A and B exclusively depend on indenter's geometry.

The influence of elasticity on hardness can be readily found comparing the hardness equation for rigid–perfectly plastic solids (Eq.(1.11)) with that for elastic–perfectly plastic ones (Eq.(1.13)). Ratio $E/\sigma_{\rm ys}$ is thus indicative of the sensitivity of the material to exhibit plastic flow rather than elastic deformation. When $E/\sigma_{\rm ys}$ is small, the contact response is considered elastic and hardness is related to the yield strength as $H/\sigma_{\rm ys} = 1.1$ (linear elastic solution). On the other hand, higher values of $E/\sigma_{\rm ys}$ lead to a fully-plastic contact regime, which is described by the slip-line theory. Three contact regimes thus emerge as $E/\sigma_{\rm ys}$ increases: a purely elastic response, an elasto-plastic transition, and the fully-plastic regime, see Fig. 1.6. In §4 we analyze the distinctive features of such contact deformation regimes in strain hardening solids ($n \neq 0$).

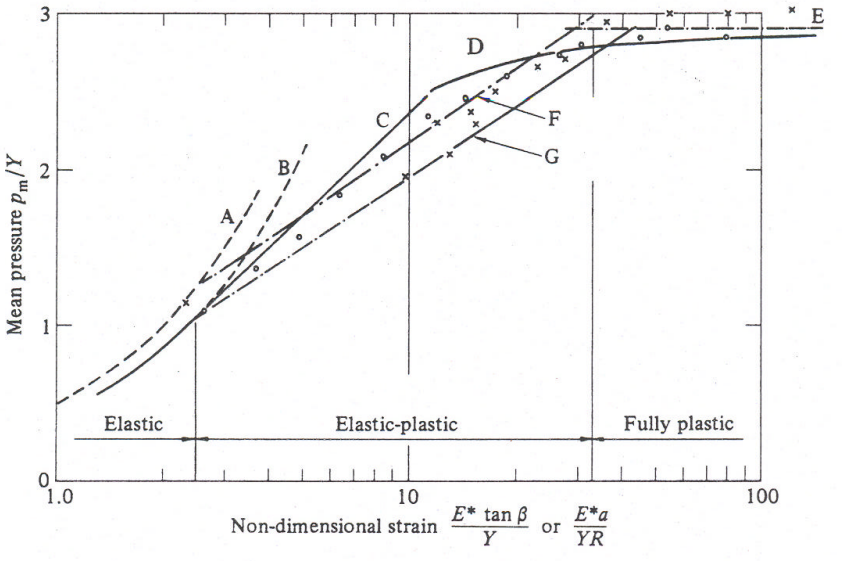

Figure 1.6: Contact deformation regimes in elastic–perfectly plastic solids indented with cones and spheres [from [46]].

A brief discussion on the influence of friction on the contact response is given in the following. Qualitatively, it is known that friction leads to an increase in the value of

hardness [42; 46; 73]. Slip-line analyses performed considering friction between indenter and material provided a first estimate on the influence of friction coefficient μ in wedge indentation. As a first approximation, hardness of rigid–perfectly plastic solids is related to that existing under frictionless contact conditions ($H_\circ$) as

$$H = H_\circ \left(1 + \mu \ \mathrm{cotan}\theta\right) \ , \tag{1.14}$$

where θ is the included half-apex angle. Also slip-line analysis for the extreme case of adhesive contacts showed that pressure distributions smoothed as compared to those attained under frictionless conditions, Fig.1.7.

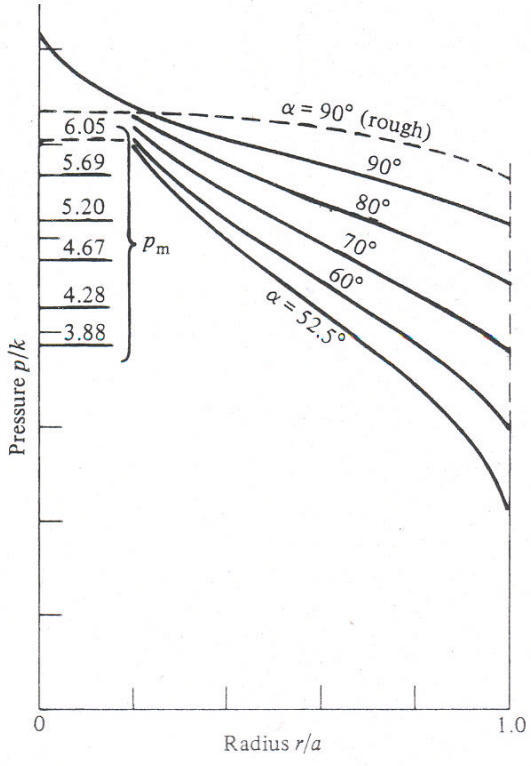

Figure 1.7: Normalized pressure distribution for frictionless contact conditions with different conical indenters [55] (solid lines), and for an adhesive 90° rigid cone (dashed line) [from [46]].

More recently, the influence of friction in spherical indentation was studied by means of finite element simulations [17; 19; 62]. Comparison between frictionless and adhesive contacts showed that friction has a considerable effect in the value of surface deformation parameter α. These investigations also pointed out that friction mainly affects the contact response of solids deforming according to Tabor's fully-plastic regime. Notice that these results are qualitative and only apply to spherical indentation. In §6 we extend such analysis to sharp indentation, providing explicit formulae from where the influence of μ on the contact response can be assessed.

1.2 Similarity analysis

A physical phenomenon is prescribed through a set of variables and their evolution in time scale. If the problem under study has recognizable patterns, it may be possible to define a *scaling law*, which prescribes the manner in which the phenomenon reproduces itself over some time, space, or predetermined scale. This leads to the general definition of *self-similar* phenomena, where "the spatial distributions of its properties at various different moments of time can be obtained from one another by a similarity transformation" [6]. [It is noteworthy that the independent variable of time has no specific significance, as any scale that is meaningful to describe the evolution of the phenomena could be used instead.]

Recognition of self-similar patterns is usually linked to *dimensional analysis*. Provided the parametrical dependencies of the phenomenon are known, dimensional analysis allows one to simplify such dependencies using sensible dimensionless parameters. If such analyses are correctly performed, the number of experiments required to solve the problem could be significantly minimized. Dimensional analysis pends upon a complete knowledge of the governing parameters of the physical phenomenon. Since dimensionless dependencies may remain hidden, application of dimensional analysis to complex problems may not capture the complete nature of the solution.

The Π-*theorem* from dimensional analysis states [6; 14]:

"If a physical law is written as a relationship between some dimensional quantity and several dimensional governing parameters, then it is possible to rewrite this relationship as a relationship between some dimensionless parameter and several dimensionless products of the governing parameters; and the number of dimensionless products is equal to the total number of the governing parameters minus the number of governing parameters with independent dimensions."

Or, equivalently, "every physically meaningful equation involving k variables can be rewritten as an equation of $k - m$ dimensionless parameters, where m is the number of the fundamental units used" [18].

The recipe for the resolution of a problem reduces to find relationships for a generic quantity a of the form

$$a = f(a_1, \ldots, a_k, b_1, \ldots, b_m) \ , \tag{1.15}$$

where $a_1, \ldots, a_k, b_1, \ldots, b_m$ are the *governing parameters* which are assumed to be given. The set of parameters a_i have independent dimensions, while the dimensions of set b_i can be expressed as products of powers of the parameters in set a_i. Notice that for $m = 0$ all the parameters are dimensionally independent, and if $k = 0$ all the governing parameters are dimensionless. Then, the parameters are translated to dimensionless variables, Π_i, which are defined as

$$\Pi_i = \frac{b_i}{{a_1}^{p_i} \ldots {a_k}^{r_i}} \ , \tag{1.16}$$

where exponents $p_i, \ldots, r_i$ are chosen so that all the parameters Π_i are dimensionless; and the quantity a also converts to the dimensionless function $\Pi = a/({a^p}_1 \ldots {a^r}_k)$. Thus, Eq.(1.15) can be rewritten as a dimensionless function of the dimensional variables (a_i) and the dimensionless ones (Π_i)

$$\Pi = F(a_1, \ldots, a_k, \Pi_1, \ldots, \Pi_m) \ . \tag{1.17}$$

Since each of the dimensional parameters is independent of any other variable, it is demonstrated that function F is in fact independent of the set of parameters a_i. Then, Π is expressed as a function Φ of m dimensionless variables

$$\Pi = \Phi(\Pi_1, \ldots, \Pi_m) \ , \tag{1.18}$$

so that if the normalization of variables b_i is known, quantity a in Eq.(1.15) becomes a function of a smaller number of variables,

$$a = f = {a_1}^p \ldots {a_k}^r \ \ \Phi\left(\frac{b_1}{{a_1}^{p_1} \ldots {a_k}^{r_1}}, \ldots, \frac{b_m}{{a_1}^{p_m} \ldots {a_k}^{r_m}}\right) \ . \tag{1.19}$$

Obviously, the key to the analysis lies in finding a set of dimensionless parameters which makes the problem scale. Again, it is emphasized that the concept of time-similar or geometrically-similar phenomenon already indicates that the phenomenon is a *physically*-similar one. Physical phenomena often exhibit a so-called "intermediate-asymptotic" response, where the solution is unaffected by specific initial and final boundary conditions. Extensive similarity analysis can be found in the comprehensive book by Barenblatt [6].

1.2.1 Application to spherical indentation experiments

The characteristic features of indentation experiments (see Section 1.1.2 and [46; 73]), leads one to consider that indentation could be treated as a self-similar phenomenon. The studies on sharp indentation in an isotropic continuum demonstrate that this process is completely self-similar as all features scale with penetration depth h_s [14; 43; 51; 73]. Hardness is therefore constant irrespective of applied load or penetration depth. This is not so in spherical indentation, where self-similarity seems to give an intermediate solution which only applies within a certain range of penetration depths in ideal rigid–plastic solids [73].

In a phenomenological sense, the contact response in spherical (Brinell) indentation evolves from an early elastic stage, to an intermediate fully-developed plastic steady-

state, to a large deformation regime. The steady state solution is thus regarded as an intermediate one. From the early work by Tabor [73], scaling law

$$H = 2.8\ \sigma_\circ \left(0.4\frac{a}{D}\right)^n \tag{1.20}$$

has been shown to govern the relationship between hardness and uniaxial mechanical properties of the solid (i.e., n and $\sigma_\circ$ in Eq. (A.21)) for indentation strains a/D of, say, between 0.1 to 0.2 (where D is the ball diameter and a is the contact radius). Numerical constants 2.8 and 0.4 in Eq.(1.20) were found from experiments in highly plastic solids.

A rationale to Eq.(1.20) was given by Hill *et al.* [43], Borodich [14], and Mesarovic *el al.* [62] through theoretical analysis. Hill *et al.* [43] simplified the constitutive response of the solid to apply self-similarity over the whole range of a spherical indentation. This was performed assuming that the solid ideally behaves as nonlinear elastic (as prescribed by the stress-strain relation $\sigma = \sigma_\circ \epsilon^n$) where the dual potentials Φ and Ψ were taken to be homogeneous functions of their arguments (see Section A.1.1). In addition, Hill *et al.* [43] represented the geometry of the spherical indenter with a parabolic shape. This assumption, valid for $a/D \leq 0.2$, also provides a homogeneous function for describing indenter's shape. Finally, straining was taken to be infinitesimal, and induced quasi-statically. Choosing an appropriate scale, they found that the overall solution had the property of self-similarity; that is, the geometrical features of the problem as well as the stress and strain fields were derivable from the solution in a previous stage. Essentially, formulation of the reduced (scaled) problem followed from the consideration that at any stage during loading, parameter

$$c^2 = \frac{a^2}{D h_{\mathrm{s}}}\ , \tag{1.21}$$

is constant; this assumption is in agreement with the early experimental results of Norbury and Samuels [64]. (Notice that from such definition, c^2 gives the amount of pileup or sinking-in occurring around the spherical indenter). As the boundary-value problem varies with penetration, successive configurations scale from the original ones as

$$a\tilde{x}_i = x_i, \quad a\tilde{r}_i = r_i, \quad a\tilde{u}_i = (D/a)\, u_i(x_k, a, D),$$
$$\tilde{\epsilon}_{ij} = (D/a)\, \epsilon_{ij}(x_k, a, D)\ , \quad \sigma_\circ \tilde{\sigma}_{ij} = (D/a)^n\, \sigma_{ij}(x_k, a, D)\ ; \tag{1.22}$$

where $\sim$ indicates scaled variables. Since from these relations the contours of displacements (u_i), stresses (σ_{ij}), and strains (ϵ_{ij}) grow uniformly with contact radius a, their patterns are preserved as indentation proceeds.

The relation between applied load P and contact radius a was obtained through similarity transformations. Following the definition of hardness in Eq. (1.9),

$$\frac{P}{\pi a^2} = -\int_0^a \sigma_{zz}(r)\ \mathrm{d}\left(\frac{r^2}{a^2}\right) = -\sigma_\circ \left(\frac{a}{D}\right)^n \int_0^1 \tilde{\sigma}_{33}(\tilde{r})\mathrm{d}(\tilde{r}^2)\ . \tag{1.23}$$

To link Eq. (1.23) with Tabor's hardness equation (Eq.(1.20)), one has to assume that the integral in the right hand side of Eq. (1.23) can be written as $\alpha\beta^n$ (where α and β depend on the shape of the energy density contours, [43]). Hence, it follows that

$$\frac{P}{\pi a^2} \approx \alpha\sigma_\circ \Big(\beta \frac{a}{D}\Big)^n\ . \tag{1.24}$$

The finite element simulations in [43] suggest that the above assumption regarding product $\alpha\beta^n$ is consistent with Tabor's experimental findings, Eq.(1.20), as $\alpha \approx 2.8$ and $\beta \approx 0.4$.

The above results are valid only within the intermediate well-developed plastic steady state. When elasticity comes into play, some of the assumptions made by Hill and coworkers [43] are violated. The effect of elasticity on the self-similarity conditions was studied in [11; 14; 62; 72]. The results allowed the authors to develop maps of indentation regimes where the range of validity of the geometrical self-similarity was given depending on the mechanical properties of the solid. At this point it is still uncertain whether spherical indentation could be ever treated within a single scaling law, providing a unified treatment of the problem that covers the elastic regime, steady state response, as well as the large deformation regime where the parabolic description of the spherical indenter breaks down (for, say, $a/D > 0.2$).

Chapter 2

Objectives

To acquire a detailed comprehension of the plastic flow features setting the contact regimes in sharp indentation experiments

We attempt to perform finite element simulations in materials exhibiting a wide range of mechanical properties to establish the limits where Tabor's fully plastic regime rules the contact response. We thus seek to develop a detailed understanding of the flow features around the imprint from which, depending on yield strength, Young's modulus, and strain hardening response, it becomes possible to predict if the indented material deforms according to the elasto-plastic transition or if Tabor's fully plastic regime dominates. Furthermore, we aim at establishing the validity of the concept of the characteristic strain, which allows one to estimate hardness values based on the uniaxial stress-strain curve of a material indented within the fully plastic regime. Based on the analogy of the expanding cavity, we finally seek to derive an equation providing hardness estimates for solids whose contact response lies within the elasto-plastic transition.

To devise a novel methodology to extract the uniaxial stress-strain curve from measurements of hardness and surface deformation phenomena

This objective requires derivation of relationships between uniaxial mechanical properties, hardness H, and surface deformation parameter α. The relationships we seek to find have to be sufficiently general as to capture the contact response of solids deforming within both the fully plastic regime and the elasto-plastic transition. Attention is given to the consistency of the proposed methodology in the context of instrumented indentation P–h_s curves.

To evaluate the role of friction on the contact response

The purpose of this investigation is to perform detailed finite element simulations and analysis to compare the contact response attained under frictional conditions with that induced in the absence of friction between a conical indenter and the material. We thus aim at simulating the contact response of strain hardening solids whose friction coefficient μ varies from 0 to 0.2, as well as to establish the influence of such variations on hardness H and on the value of surface deformation parameter α. A theoretical framework is to be derived which enables analysis of the simulations in the context of continuum mechanics. This knowledge is pertinent to the experimental application of the proposed methodology for mechanical property extraction, as it allows one to evaluate the influence of μ on inferred values of yield strength σ_{ys} and hardening parameter n.

To derive a general framework for the prediction of the plastic zone size in indentation experiments

The approach adopted herein to find expressions between the plastic zone size and uniaxial mechanical properties, resorts to the analogy between indentation and the expansion of a spherical cavity in an infinite medium. We thus seek to derive closed-form solutions for the inflation of a cavity in strain hardening solids, as well as to find a strict parametrical analogy between this problem and indentation experiments. Consideration of the active regime governing the contact response of the solid is central to the present analysis.

Chapter 3

Computational and experimental procedures

A multidisciplinary approach is adopted in this thesis as it combines finite element simulations, continuum mechanics analysis, and experiments to bring an overall perspective to the study of indentation experiments. The simulations allow one to evaluate the contact response in terms of measurable quantities such as hardness, the amount of surface deformation, and the parameters extracted from instrumented indentation P–h_s curves. They also provide the stress and strain fields, pressure distributions, and plastic flow patterns during contact. Indentation experiments, on the other hand, validate the applicability of the results to metallic materials. Comparison between experiments and simulations is therefore a necessary step in demonstrating, for instance, the applicability of a simplified conical model to the study of pyramidal indentation, which has a truly three-dimensional character. Finally, there is a need to develop a sound theoretical background incorporating the knowledge gained through simulations and experiments.

3.1 Finite Element simulations

3.1.1 Definition of the model

The finite element simulations were conducted with the commercial code ABAQUS [1]. Two fundamental hypothesis were made in the simulations. First, the indenter was taken

as a rigid solid. Secondly, the material was modelled as a homogeneous and isotropic solid obeying continuum mechanics. For spherical indentations ball radius R is the only parameter needed to define the indenter whereas, for conical indentations, one has to define a semi-apical angle θ. In the present simulations, θ is taken as 70.3° as it provides the same ratio of contact area (A_s) – penetration depth (h_s) as the Vickers and Berkovich pyramidal indenters (see Section 3.2).

The indented solid is assumed to deform according to the J_2 flow theory of plasticity, which consists of a von Mises yield criterium, and a flow rule associated to this yield condition (see Appendix A). The concepts of the von mises equivalent stress and strain are thus used to extend a uniaxial elastic–power law plastic stress-strain behavior (whose key parameters are Young's modulus E, yield strength σ_{ys}, and power-law strain hardening coefficient n) to a generic three-dimensional state. Large strains and rotations were accounted for in the analysis.

The mechanical properties of the solids comprised all combinations of Young modulus $E = 70$, 110 and 200 GPa; yield strength $\sigma_{ys} = 50$, 100, 400 and 1000 MPa; and strain-hardening coefficient $n = 0$, 0.1, 0.2 and 0.4. In addition to these combinations, solids with intermediate properties were considered (see Table 5.1 in §5, Table 3.1 in Section 3.2, and Table 3.2). Overall, 68 solids with a wide range of mechanical properties were used in the simulations.

The finite element mesh employed in the simulations of conical and spherical indentation comprised four regions of decreasing element density, where the indenter was located on top of the denser region. Such density-region hierarchy owes to the need of having a refined mesh at the contact zone, to improve accuracy and convergence, as well as to minimize the total number of elements for the purpose of reducing computational expense. The transition between regions of different element density is gradual so that the stress and strain fields are rather continuous (see the detail of the transition from 3 elements to 1 in Fig. 3.1). The elements were chosen to be quadratic and axisymmetric with eight integration points. The denser zone right in contact with the indenter had 52×52 elements. In total, 11.905 elements were used in the full mesh.

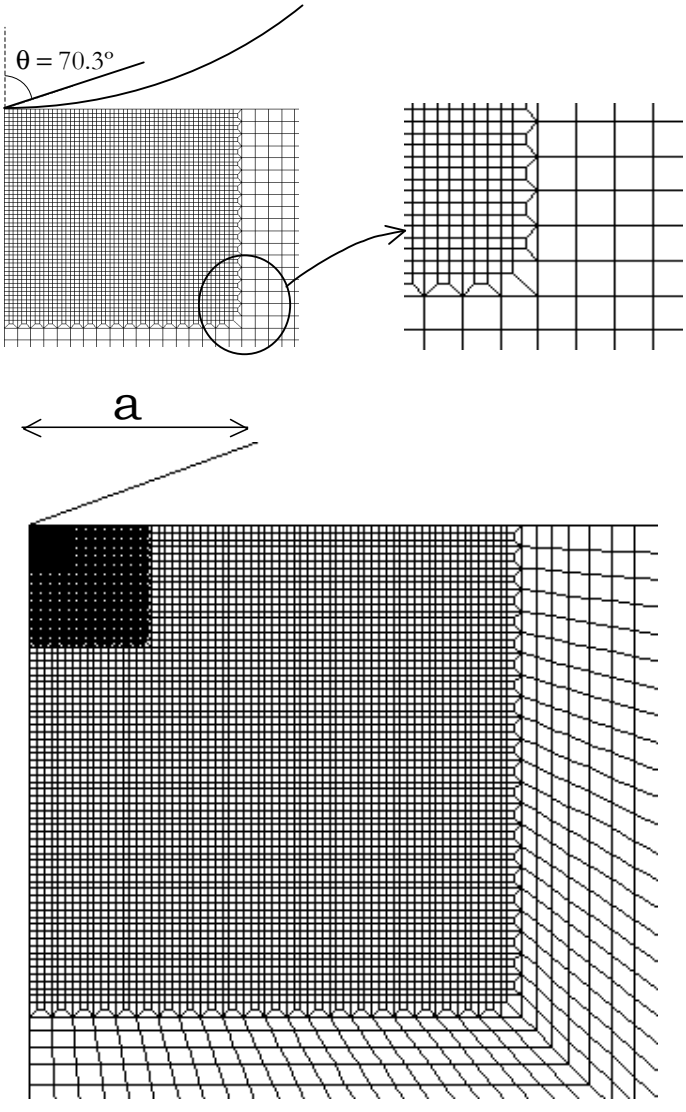

Figure 3.1: Finite element mesh used in the simulations. Attention is given to the transition from three elements to one element between consecutive mesh zones.

Following the considerations by Giannakopoulos *et al.* [39] suggesting violation of the Saint-Venant's principle in contact problems, the extension of the mesh was sufficiently large as to ensure that the outer free-boundaries do not affect the solution of the problem. Consequently, total mesh length was set to be at least 50-times greater than maximum contact radius. Mesh independency was verified for perfectly elastic solids through comparison with Herztian solution for spherical indentation and Sneddon's solution for conical indentation (see §1 and Section 3.1.2).

Imposed boundary conditions are shown in Fig. 3.2. Nodes at the axis of symmetry can only move in direction 2. All nodes at the base are prevented to move in such vertical direction as they are only allowed to slide freely along the horizontal direction. The indentation process is conducted imposing a fixed displacement in the 2-direction at the reference node of the indenter. The contact interaction is modelled as *hard*, meaning that there is no allowance of the nodes at the material surface to penetrate indenter's surface. Although some allowance of interpenetration of the contacting surfaces (*overclosure*) may facilitate convergence, this strategy was not used to improve the accuracy in the simulations. Convergence is herein improved through current mesh refinement approach and by carefully imposing suitable indenter displacements between two consecutive computational increments.

3.1.2 Validation of the model

As indicated above, the finite element simulations were confronted against linear elastic solutions. For conical indentation, Sneddon's theoretical solution for hardness H in elastic solids was used [70]

$$p_{\mathrm{m}} = \frac{E\mathrm{cotan}\theta}{2(1-\nu^2)} \ . \tag{3.1}$$

For the spherical indentations, we compare the simulations against the theoretical equation by Hertz [41]

$$p_{\mathrm{m}} = \frac{4Ea/R}{3\pi(1-\nu^2)} \ . \tag{3.2}$$

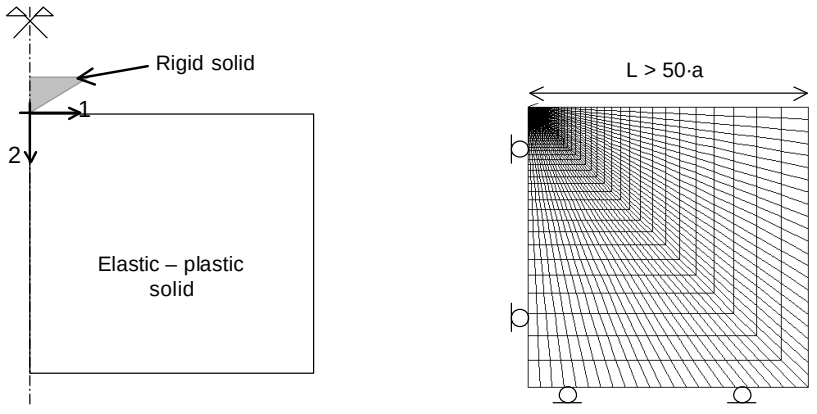

Figure 3.2: Reference axis, boundary conditions and total mesh length L.

As Hertz theory applies under small deformations, it may be taken to be valid only for $a/R < 0.4$, where the spherical tip can be truly approximated through a parabolic description.

Comparison between the value of hardness obtained in the simulations and the theoretical one allowed us to determine the minimum number of elements in contact with the indenter to obtain reliable data. The plots in Fig. 3.3 show the relative error in hardness in terms of the number of elements, where it is readily seen that the average error decreases to 4.4% and to 3% when more than 15 elements become in contact in conical and spherical indentation, respectively. Notice that the optimum number of elements in contact in spherical simulations depends on tip radius R. For small values of R, 15 elements in contact may violate the condition of $a/R < 0.4$. On the other hand, large values of R may require more than 15 elements to become in contact to capture the complete elastic solution up to $a/R \sim 0.4$. In addition, R has to be small enough to fulfill the requirement of having a total mesh length which is at least 50-times larger than maximum contact radius a. The simulations in Fig. 3.3 are for the spherical indenter employed in the present simulations, whose ratio of ball radius to finer element

size is 114 elements. In view of the relative error in Figs. 3.3(a) and (b), analysis of the simulations was performed with at least 20 elements in contact. Along these lines, it is worth noting that the elastic finite element simulations involved a small strain formulation, whereas large strains were accounted for in the computations performed with the J_2-flow theory. Differences between the strict linear elastic solutions and the simulations may thus be attributed to the role of large strains on the contact response.

3.2 Indentation experiments

3.2.1 Materials

The J_2-associated flow plasticity theory used in the simulations is known to give a good description of the elastoplastic response of metallic materials. To ensure that the indented solid fulfills the hypothesis of the model, the former shall have well defined values of E and σ_{ys} as well to strain harden according to a unique power law hardening exponent. The latter assumption is an important one in the sense that strain hardening parameter n is found to depend slightly on imposed deformation level in metallic materials [31]. However, a constant value of n is usually reached at intermediate levels of uniaxial deformation. The main mechanism for plastic deformation shall be dislocation slip which is taken to be pressure independent following the postulates of the plasticity model. Deformation through void coalescence and twinning thus has to be negligible as compared to dislocation slip mechanisms.

The mechanical properties of the materials used in the indentation experiments are given in Table 3.1. The materials comprise annealed copper (99.9% pure), an AISI329 duplex stainless steel, and a SAF2507 superduplex stainless steel. Prior to indentation, the materials were sectioned and polished using diamond paste. A final polishing step with a 1-micron alumina suspension was applied to all materials. A suspension of colloidal silica was employed as final polishing step in the annealed copper.

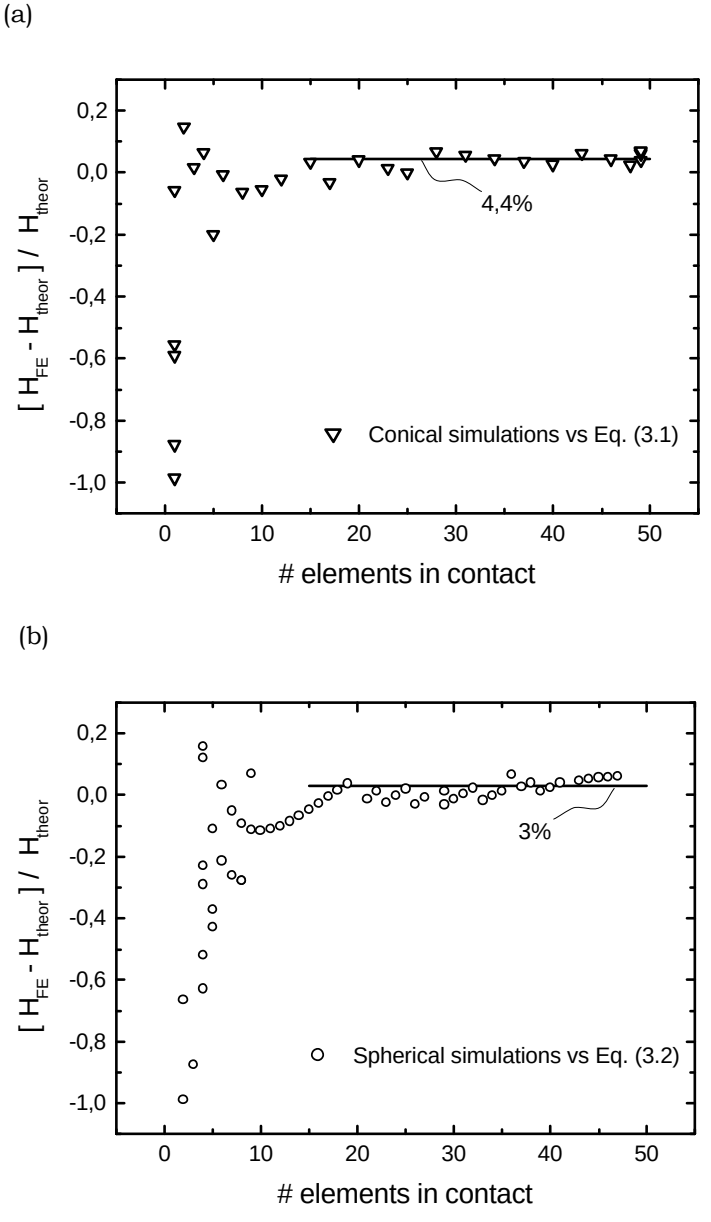

Figure 3.3: Relative error in hardness in terms of the number of elements in contact with the indenter. (a) conical indentation with $\theta = 70.3°$, and (b) spherical indentation to $a/R < 0.4$. Simulations are for $E = 200$ GPa.

	E (GPa)	σ_{ys} [†] (MPa)	n	Grain size (μm)
Annealed copper	110	20	0.52	60
AISI 329 duplex stainless steel	190	525	0.17	ferrite (62%): 9 μm, austenite: 6 μm
SAF 2507 superduplex stainless steel	200	675	0.19	ferrite (44%): 9 μm, austenite: 9 μm

[†] measured directly in the uniaxial stress-strain curve. It is noted that these values may not exactly lie within the power-law fit to this curve.

Table 3.1: Materials used in the indentation experiments.

3.2.2 Conventional hardness testing

Indentation experiments were performed with a Vickers pyramidal tip. This indenter was selected as it could provide some insights into the extension of current axisymmetric (cone) simulations to three-dimensional (pyramidal) tips.

As explained in the following discussion, the apex angle of the cone was set at 70.3° as its contact area–penetration depth relation is the same as that of the Vickers pyramid. From Fig. 3.4, the value of the equivalent cone angle θ is determined by equating areas A_s for the pyramid and the cone at fixed penetration depth h_s. The nominal area of the Vickers imprint is given by

$$A_s = (2c_s)^2 \tag{3.3}$$

or, in terms of the penetration depth,

$$A_s = (2h_s \tan 68^\circ)^2 \ . \tag{3.4}$$

Equivalently, A_s in conical indentation is expressed as

$$A_s = \pi \, (h_s \tan\theta)^2 \ . \tag{3.5}$$

Therefore, the equivalent cone angle is obtained as

$$\theta = \arctan\sqrt{\left(\frac{2\tan 68^\circ}{\pi}\right)} = 70.3^\circ \ . \tag{3.6}$$

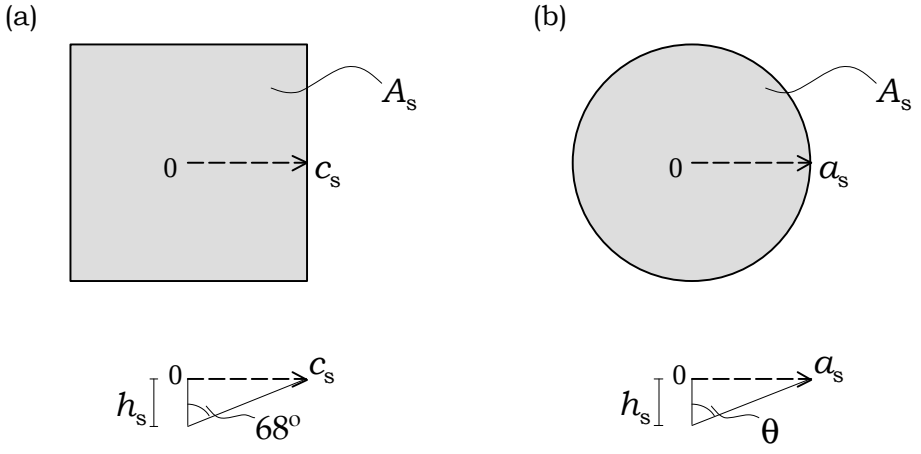

Figure 3.4: Equivalent cone angle θ between the Vickers indenter (a) and a conical tip (b).

Hardness values were computed as the ratio between applied load P and true projected contact area A of the imprint,

$$H = \frac{P}{A} \ , \tag{3.7}$$

where contact area A includes the pileup or the sinking-in effects of the material as indicated in Section 1.1.1. Also, nominal hardness H_s was calculated taking the imprint as a perfect square. That is, estimating contact area A_s from opposite vertices of the the imprint and assuming that bulging (pileup) or pincushion (sinking-in) effects do not appear at the sides, Fig. 1.1 and Fig.3.5. Differences between H and H_s are shown in Table 3.2, Section 3.3. The micrographs in Fig. 3.5 are top views of Vickers imprints obtained through conventional optical microscopy with Nomarski interferometry, where bulging and pincushion effects are illustrated.

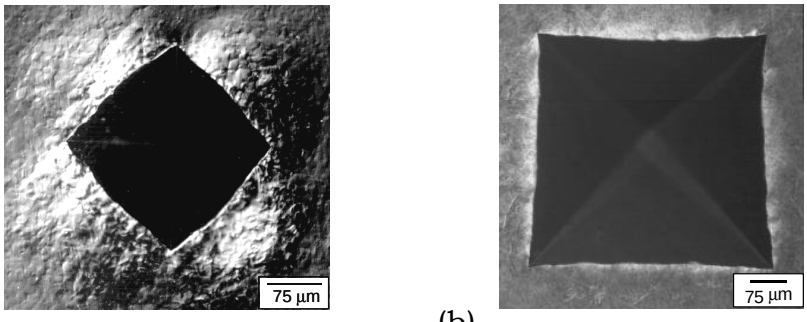

Figure 3.5: Indentation imprints on (a) AISI329 duplex stainless steel and (b) annealed copper. Note the bulging and the slight pincushion shapes, respectively.

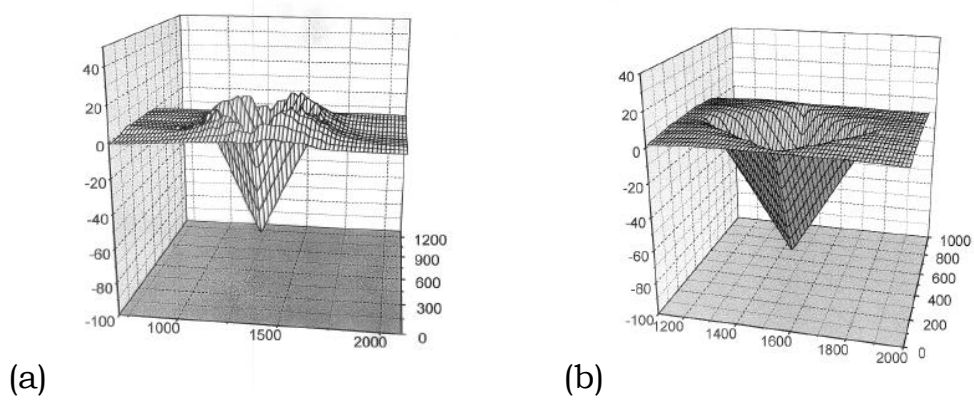

Figure 3.6: Profilometry of a Vickers indentation in (a) work-hardened copper and (b) annealed copper. Note the development of (a) pileup and (b) sinking-in. From [3].

Following Section 1.1.1, the amount of pileup or sinking-in at the contact boundary is evaluated through parameter α, where

$$\alpha = \frac{A}{A_\mathrm{s}} \tag{3.8}$$

Nominal area A_s is directly inferred from imprint diagonals $\bar{d}$ as,

$$A_\mathrm{s} = \frac{\bar{d}^2}{2} \ ; \tag{3.9}$$

whereas contact area A is obtained through optical measurements with the aid of an image analysis software.

The applied load in the experiments was selected to be sufficiently large to rule out possible indentation size effects. In this regard, P was varied from 1 N to 150 N to evaluate constancy of hardness H. A size effect was found in all materials since for small loads, hardness increased with decreasing load. Such indentation size effects elude continuum analysis since, for small loads, the indentation process becomes representative of the deformation of a discrete number of grains or microstructural features. The critical load above which hardness remains constant was of about 5 N for copper and 10 N for the stainless steels. The micrograph in Fig. 3.7 illustrates that when applied load is sufficiently large, microstructural length scales become an order of magnitude smaller than imprint size, so that the contact response can be taken to represent the behavior of the continuum.

3.2.3 Instrumented Indentation

In addition to conventional hardness testing, instrumented indentation experiments were performed to obtain *in situ* recordings of applied load (P)–penetration depth (h_s) curves. The instrumented technique captures the progress of the experiment in time so that, for instance, it allows one to examine the evolution of the contact response in light of self-similarity analysis.

Again, the experiments shall satisfy the conditions assumed in the finite element simulations. Hence, the applied load shall be sufficiently large as to enable a continuum

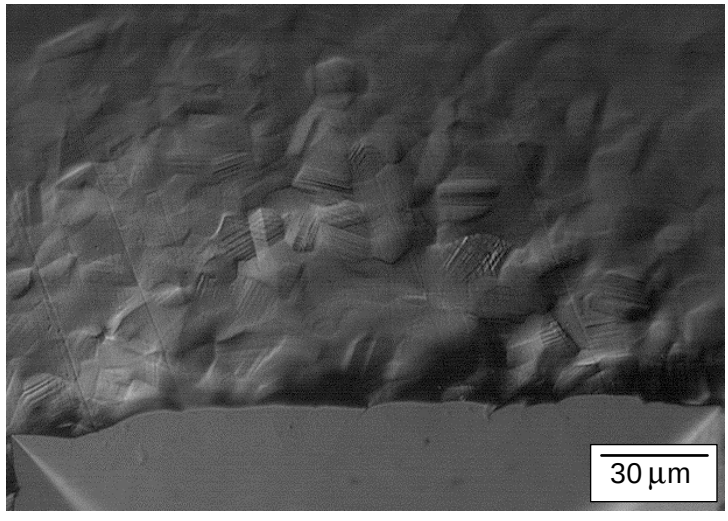

Figure 3.7: Micrograph of one side of the Vickers indentation imprint in the SAF2507 superduplex stainless steel. Ferrite and austenite grains are revealed due to anisotropy in plastic flow. Notice the development of pileup as bulging effects occur in the material located between the corners.

mechanics treatment of the indentation process. An instrumented indenter was set up during the course of this work to perform the required measurements to maximum applied loads in the range of 5–100 N. Again, a Vickers pyramidal tip was used in the instrumented indentation experiments.

Description of the instrumented indentation device and experimental procedure

A schematic of the instrumented indentation device is depicted in Fig. 3.8. The vertical displacement of crosshead (A) induces penetration of indenter (B) into specimen (C). Measurement of penetration depth, h_s, is performed with respect to the surface of the material using three-legged reference table (D). Capacitive sensor (E) is employed in such measurements of h_s. Load cell (F) is used to continuously measure applied load. The maximum load and penetration depth of the system were 300 N and 100 μm, respectively. Load and displacement resolutions were 0.01 N and 0.01 μm.

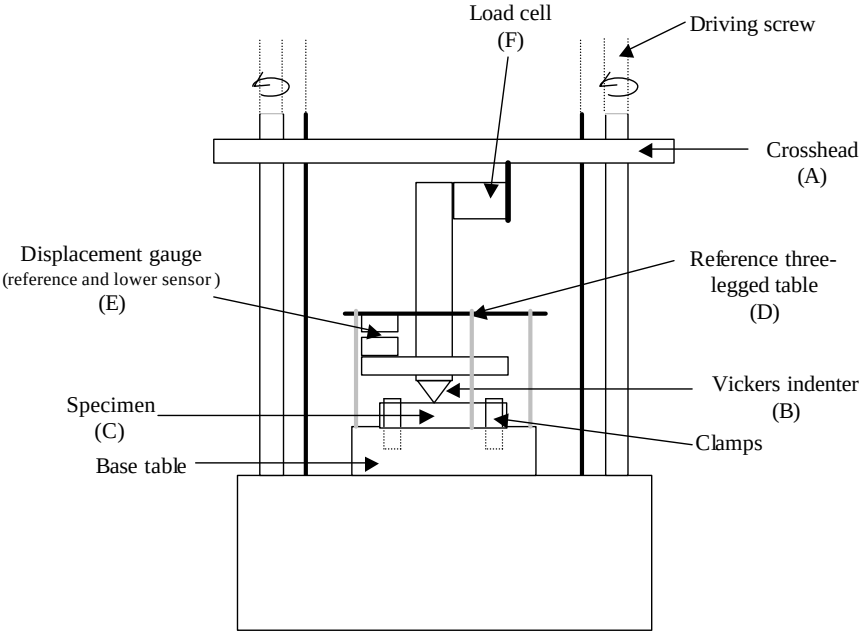

Figure 3.8: Schematic of the instrumented indentation device.

The P–h_s curves were corrected for machine compliance to obtain accurate measurements of penetration depth [32; 65]. Following Eq. (1.5), this was accomplished by numerical fitting of the unloading segment of the P–h_s curves between P_max and $0.9P_\mathrm{max}$ to the following equation [69]

$$\left(\frac{1-\nu_\mathrm{m}^2}{E_\mathrm{m}}+\frac{1-\nu_\mathrm{i}^2}{E_\mathrm{i}}\right)^{-1}=\frac{1}{1.142\sqrt{A_\mathrm{max}}}\left.\frac{\mathrm{d}P}{\mathrm{d}h_\mathrm{s}}\right|_{h_\mathrm{max}}, \tag{3.10}$$

where E_m and ν_m are the Young's modulus and Poisson's ratio of the indented material, A_max is the area of the imprint, and E_i and ν_i are introduced to account for the Young's modulus and Poisson's ratio of the Vickers diamond (i.e., $E_\mathrm{i}=1000$ GPa and $\nu_\mathrm{i}=0.22$). The correction factor for machine compliance is then given by the difference between experimentally measured values of $\mathrm{d}h_\mathrm{s}/\mathrm{d}P$ in both the copper specimen and in the 2.8 mol% yttria-stabilized tetragonal zirconia (Y-TZP) in [4], and the theoretical ones computed with Eq. (3.10). In such calculations, the values of E and ν reported in [3], and the corresponding A_max estimated through optical microscopy were employed. This procedure is similar to the one used in nano-indentation experiments where the plot of the total compliance (specimen plus loading frame) in terms of ${h_\mathrm{max}}^{-1}$ is found to be linear [69]. The influence of machine compliance upon the P–h_s curve is significant as illustrated in Fig. 3.9.

Upon correction for machine compliance, analysis of the loading segments of the P–h_s curves was performed fitting them to the parabolic relation, $P=K{h_\mathrm{s}}^2$ (see Kick's law in Eq.(1.7)). It was found that after the initial low-load range, where the contact response is affected by indentation size effects, the value of K remained relatively constant. This finding is consistent with the fact that, according to continuum analysis, hardness and surface deformation parameter shall take constant values irrespectively of applied load or penetration depth. As $K=f\alpha H$, Section 1.1.1, K turns out to be a material parameter for a fixed indenter's geometry.

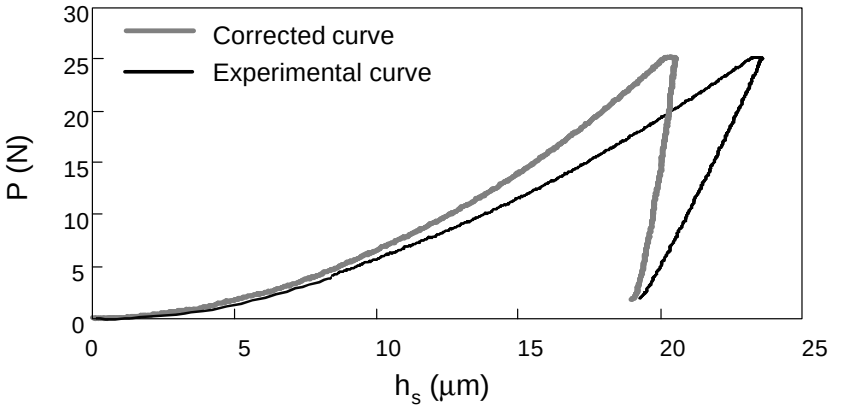

Figure 3.9: Effect of machine compliance on an instrumented indentation P–h_s curve of the AISI329 duplex stainless steel.

3.3 Comparison between experiments and finite element simulations

In this section, we compare the experimental results obtained in the metallic materials with those from the finite element simulations performed with their uniaxial mechanical properties (Table 3.1). Additional simulations were carried out considering properties of other metallic materials referenced in the literature [22; 39; 73].

Overall, Vickers hardness values are in good agreement with those from the finite element simulations of conical indentation, where the differences lie in the range of 2–8%, Table 3.2. These differences could be attributed to the role of friction on the contact response (as friction may increase contact pressure up to 7% [34; 46]). The complementary simulations with the materials in the literature [22; 73] are also in good accord with the conical simulations. Finally, we compared our conical simulations against the three-dimensional Vickers simulations performed by Giannakopoulos *et al.* [39] with the properties of a 6061-T6 aluminium alloy. Again the difference in hardness values was smaller than 6 %.

	H (cone) * present simulations (GPa)	H (Vickers) considering pileup and sinking-in (GPa)	H_s (Vickers) regarding the imprint as a perfect square (GPa)	K (cone) present simulations (GPa)	K (Vickers) instrumented indentation (GPa)	$\sqrt{\alpha}$ - 1 present simulations	$\sqrt{\alpha}$ - 1 [3]
Annealed copper	0.47	0.52	0.48	9.60	10	- 6 %	- 5 % [r]
AISI 329 duplex stainless steel	2.10	2.21	2.38	55.55	60	9.5 %	8 %
SAF 2507 duplex stainless steel	2.45	2.57	2.63	66.44	68.4	8.5 %	6 %
Strain hardened copper, Ref. [3]	0.90	0.85	1.02	–	–	17.5 %	16 %
Annealed copper, Ref. [22]	0.45	0.48[§]	0.44	–	–	–	–
Aluminium 6061-T6, Ref. [39]	1.17	1.10	–	–	–	–	–
Annealed copper, Ref. [73]	0.46	0.47*	0.42	–	–	–	–
Mild Steel, Ref. [73]	1.56	1.47*	1.68	–	–	–	–

[§] calculated with the sinking-in shown in Fig. 4b of Ref. [22].

* calculated considering piling-up and sinking-in from present simulations.

[r] calculated from present indentation experiments.

Table 3.2: Comparison of the values of hardness and surface deformation obtained from the simulations and the indentation experiments.

The value of surface deformation parameter α was obtained through the ratio of contact areas in Vickers imprints (Eq. 3.8). The results, given in Table 3.2, are in good accord with those from the simulations of conical indentation obtained under the maximum applied load. This finding seems to suggest an equivalency between the average value of α measured as indicated above for the Vickers pyramid, and the constant value attained around the contact boundary in conical indentation. Overall, the results of parameter α are similar to those obtained by Alcalá *et al.* through surface profilometry measurements in the same materials [3].

The finite element simulations confirm that while $\sqrt{\alpha}$ is greatly affected by surface rebound upon unloading, the projected area of the imprint remains constant throughout the entire unloading process [65]. This is due to the fact that the elastic rebound produces a vertical displacement along the imprint while negligible radial displacement occurs. The change of the imprint size between the loaded and unloaded states can thus be neglected as it leads to a variation in hardness that is smaller than 0.5% for the present stainless steels and copper specimens. In this regard, the results from the overall simulations performed with a wide variety of uniaxial stress–strain curves show that the maximum increase of the imprint size due to unloading in solids that develop

pileup is 0.6%, and that this value increases to 1.9% in solids exhibiting sinking-in.

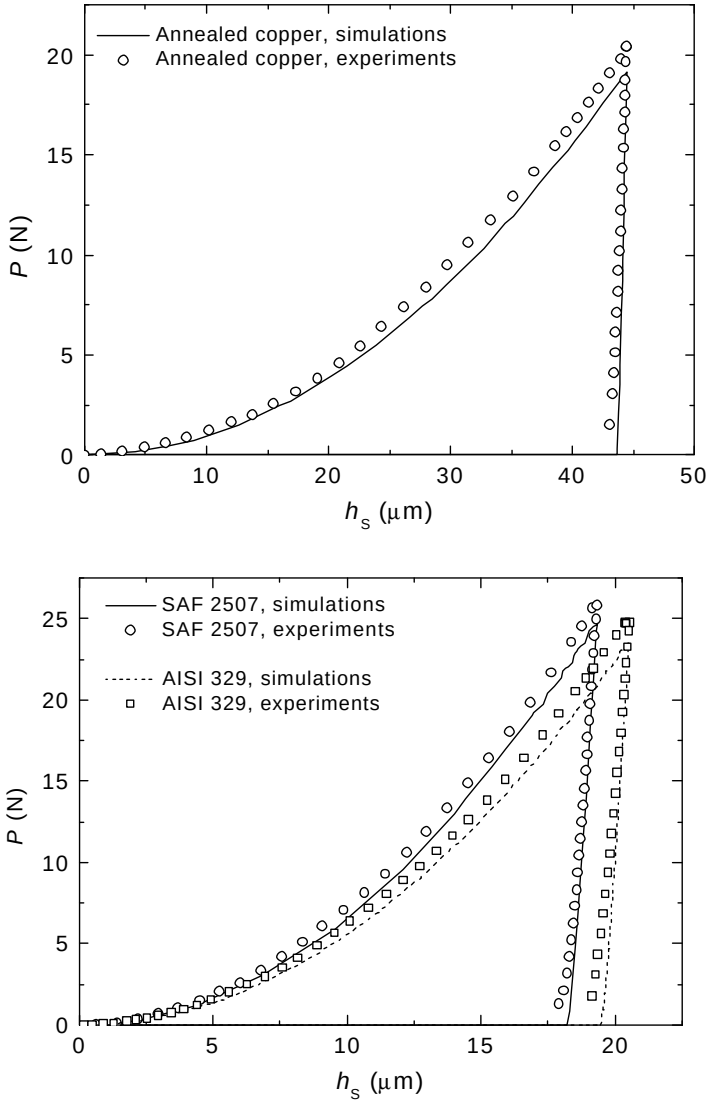

Figure 3.10: Instrumented indentation P–h_s curves for annealed copper CuAR, and stainless steels AISI329 and SAF2507.

Figure 3.10 shows that the experimentally measured P–h_s curves are also in good accord with those from the finite element simulations. Variations in K between experiments and simulations were about 5 % at loads that are sufficiently large as to rule out indentation size effects (Table 3.2).

Chapter 4

Contact deformation regimes and the concept of the characteristic strain

A fundamental characterization of the mechanical response by means of indentation experiments requires to gain a precise understanding of the correlation between hardness and the uniaxial properties of the material. As described in Section 1.1.2, relations are given in the literature for different idealized material responses. We direct special attention to the hardness equation proposed by Tabor [73] for metallic materials,

$$H = C\sigma_{\mathrm{r}} \ , \tag{4.1}$$

which is assumed to rule indentation of elastic–strain-hardening solids. Such equation, determined upon Vickers indentation experiments in annealed copper and a mild steel that had been strain-hardened to different stages, indicates that hardness H is proportional to a representative uniaxial stress σ_{r}. This stress level is associated with a constant characteristic strain ϵ_{r} located within the uniaxial stress-strain curve of the material, whose value depends exclusively on indenter's shape. Tabor found that irrespectively of the indented material, $\epsilon_{\mathrm{r}} = 0.08$ for the Vickers pyramid. The concept of the characteristic stress transpires from slip-line analysis, where hardness is necessarily proportional

to the only material length scale, i.e., yield strength σ_{ys}. Thus, in the absence of strain hardening effects, $\sigma_r = \sigma_{ys}$.

In recent years, several numerical and experimental investigations on sharp indentation experiments of strain-hardening solids have been conducted with the aim of correlating hardness with the uniaxial mechanical response [22; 26; 27; 30; 36; 39; 50; 51; 53]. However, a systematic investigation on the limit between the elasto-plastic transition and Tabor's fully-plastic regime (see Section 1.1.2) was still unavailable when present work was initiated.

4.1 The concept of the characteristic strain

In contrast to Tabor's findings, simulations and indentation experiments performed by several authors lead to different conclusions about the value and uniqueness of characteristic strain ϵ_r. The works by Giannakopoulos *et al.* [39] on Vickers indentation, and by Larsson *et al.* [50] on Berkovich indentation, advocated a value of $\epsilon_r = 0.3$. They justified this value considering that the shape of the equivalent plastic strain contours underneath the indenter exhibited a transition at about 0.3. The experimental work by Chaudhri [22] also revealed that the maximum plastic strain level reached beneath a Vickers indentation varied from 0.25 to 0.36 depending on the strain hardening behavior of the material. Variations from Tabor's concepts were proposed by Cheng and Li [27] from finite element simulations of conical indentation. They considered a constant characteristic strain of 0.10 allowing C in Eq. (4.1) to change from 1.5 to 2.5 depending on the plastic response of the material.

In this section, we examine the validity of Tabor's equation and the uniqueness of the characteristic strain through the hardness values and strains fields obtained by recourse to the present finite element simulations of conical indentation in Section 3.1. The simulations performed in strain hardening solids, $n > 0$, confirm the applicability of Eq.(4.1) where $C = 2.70 \pm 0.03$ and $\epsilon_r = 0.10 \pm 0.01$. Fig. 4.1 shows the fluctuation in the constant C when ϵ_r is allowed to vary in the vicinity of 0.10. (Notice that present analysis pertains to *total* strains —i.e., ϵ_r is taken to be the sum of elastic and plastic

components—) For the value of 0.08 proposed by Tabor, it can be readily seen that C becomes slightly dependent of the strain-hardening parameter n; the same trend is found by increasing ϵ_r to 0.12. Thus, it is only when $\epsilon_r = 0.10$ that C becomes 2.7 regardless of the value of n. Present results thus confirm the accuracy of Tabor's approach as the influence of strain hardening on hardness is captured within a 1 % error through the concept of a unique characteristic strain, which takes a similar value as that proposed by Tabor. Note that following Section 1.1.2, the applicability of Tabor's equation is limited to the fully plastic contact mode, where the contact response is plastically dominated (see Sections 4.2 and 4.3).

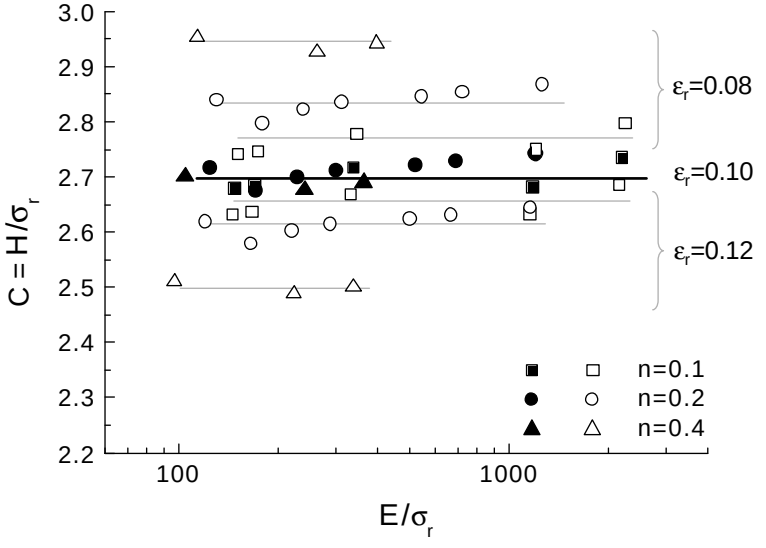

Figure 4.1: Validity of Tabor's hardness equation in elastic–power-law plastic materials lying within the fully plastic contact regime. Note that a constant value of H/σ_r is attained only when the characteristic strain ϵ_r is taken as 0.1. Slightly different values of ϵ_r (i.e., 0.08 and 0.12) start to indicate a dependency of H/σ_r on strain hardening coefficient n.

In view of the difference between the present characteristic strain and that obtained by Giannakopoulos *et al.* [39] and Chaudhri [22], we examined the equivalent plastic strain isocontours from our finite element simulations in an attempt to provide a physical

interpretation for such strain level. Following the considerations by Giannakopoulos *et al.*, ϵ_r may be associated with a strain isocontour whose shape is in transition from that existing directly underneath the tip to that present slightly away. Nevertheless, present simulations indicate that this transition may occur for equivalent plastic strain levels ranging from 0.3 to 0.05 depending on Young modulus E, yield strength σ_{ys}, and strain-hardening coefficient n (Fig. 4.2 illustrates a solid where this transition occurs below 0.10). The work by Chaudhri provides experimental data for the plastic strain levels that are attained underneath the indenter. From detailed micro-hardness measurements beneath a macro Vickers indentation, Chaudhri showed that the maximum plastic strain is located close to the indenter's tip and that its value lies within the range 0.25 – 0.36, which is consonant with the ϵ_r given by Giannakopoulos *et al.* Present simulations, however, indicate that the plastic strains can reach a value of 2 directly under the indenter's tip, which is well above Chaudhri's values (Fig. 4.2). In light of the present discussion, it follows that while the simulations demonstrate the validity of Tabor's hardness equation and the uniqueness of the characteristic strain, it is not possible to substantiate these findings on the basis of the plastic strain fields induced underneath the indenter.

In addition to the present materials, we also evaluated Tabor's hardness equation ($H = 2.7\ \sigma_{0.10}$) in the solids whose properties were taken from the literature (Table 3.2). These simulations were performed considering point-by-point the experimentally measured uniaxial stress-strain curves (i.e., without the approximation of power-law hardening). The results show that within a 2% error, hardness values are in agreement with those obtained multiplying 2.70 by the actual uniaxial stress measured at a total deformation of 0.1. This suggests that slight experimental modifications in the power-law stress-strain relation may not significantly affect the values of C and ϵ_r. Further simulations performed on elastic–linear strain hardening solids, where σ_{ys} ranges from 50 to 400 MPa and hardening slope m varies from 400 to 5000 MPa (see Appendix A), show that the characteristic strain increased from 0.10 to 0.18 in the most critical cases. To a first approximation, however, Tabor's equation was found to be accurate for linear

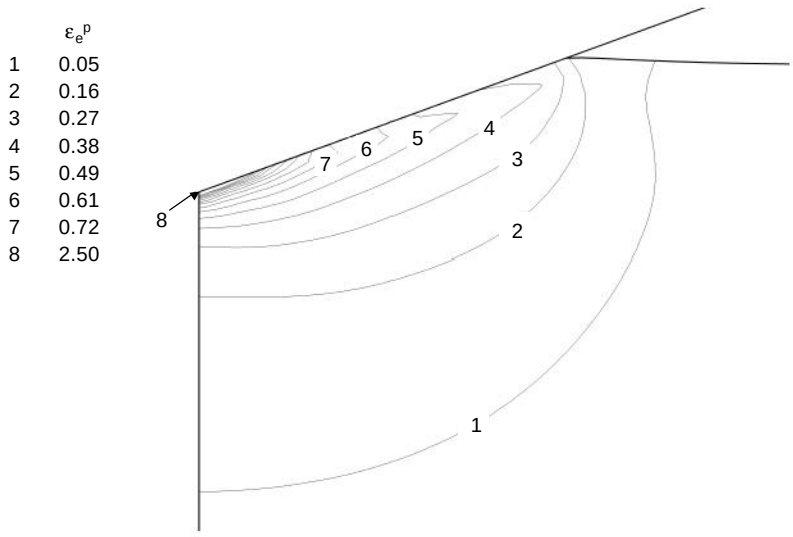

Figure 4.2: Equivalent plastic strain isocontours around the indenter's tip for a solid with $E = 70$ GPa, $\sigma_{\text{ys}} = 400$ MPa and $n = 0.1$.

hardening provided (i) $\sigma_{0.10}/\sigma_{\rm ys} \geq 4$, and (ii) hardening slope and yield strength are relatively small so that $\epsilon_{\rm r}$ takes a similar value regardless the hardening model.

In an independent work, a comprehensive study on Tabor's equation and on the influence of the strain hardening response was published by Larsson [51]. His investigation mainly dealt with finite element simulations of *rigid*–power-law hardening solids, Fig. A.4(c), concluding that Tabor's equation was accurate when $\epsilon_{\rm r}$ was taken at about 0.18, which is considerably greater than present value for *elastic*–power-law hardening solids.

A remark is made concerning applicability of Tabor's equation to elastic–perfectly plastic solids, $n = 0$. The simulations in Fig. 4.3 indicate that constant C is 2.57 for $n = 0$, which is slightly smaller than the value of 2.70 obtained in strain-hardening solids. This result is in good accordance with the simulations by Larsson [51], who obtained $C = 2.55$ for conical indentation of rigid–power-law hardening solids, where elasticity is neglected. Turning to the slip-line analyses for cone indentation, which are strictly applicable to rigid–perfectly plastic solids, it is found that $C = 2.73$ for $\theta = 70.3°$ [55; 80] (Section 1.1.2). Interestingly, this value is much closer to that obtained herein for elastic–strain-hardening solids than that for elastic–perfectly plastic ones.

4.2 Contact deformation map

The early experimental work by Marsh [58] and by Hirst and Howse [44] already suggested that hard materials do not follow Tabor's equation. In the 1970's, based upon these results and using an analogy between indentation and the problem of an expanding spherical cavity in an infinite solid, Johnson [47] identified three contact modes, namely: elastic, elasto-plastic, and fully plastic. These regimes were considered to rule the contact response depending on the value of dimensionless parameter $E\ \mathrm{cotan}\theta/\sigma_{\rm ys}$. For extremely low values of this parameter, hardness is governed by linear elasticity. When $H/\sigma_{\rm ys} > 0.5$, plasticity commences and the material deforms within an elasto-plastic transition. Finally, when $H/\sigma_{\rm ys} \approx 3$ and $E\ \mathrm{cotan}\theta/\sigma_{\rm ys} \approx 35$, the solid is taken to deform as fully-plastic (Tabor's equation). The inclusion of the apex angle in the

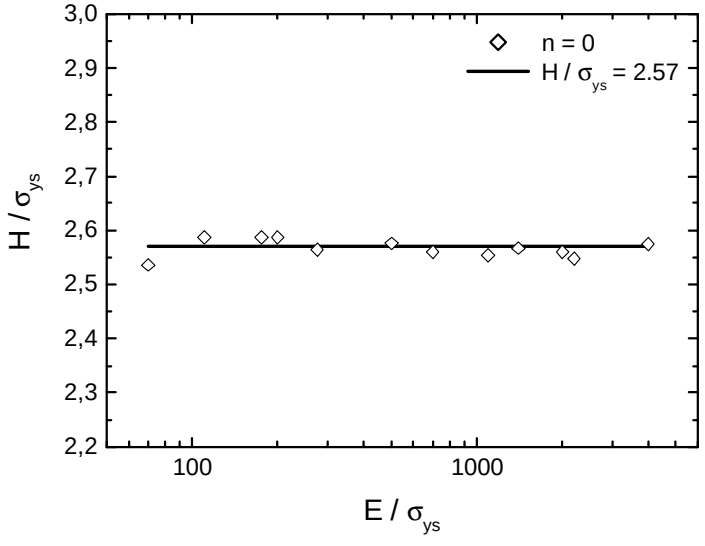

Figure 4.3: Correlation between hardness and yield strength σ_{ys} for elastic–perfectly plastic solids. Notice that H/σ_{ys} takes a constant value of 2.57.

above dimensionless parameter indicates that Tabor's fully-plastic regime is more likely to occur for acute indenters, where θ is small.

The present finite element simulations allow one to incorporate the role of strain hardening in setting the active contact regime. Solids fulfilling Tabor's hardness equation are identified as fully plastic, while those where hardness cannot be considered proportional to the representative stress are regarded to deform within the elasto-plastic transition. The results from the simulations allow us to build a *contact deformation map* that prescribes the contact mode in terms of the elastic (E) and plastic (σ_{ys} and n) properties. The map is given in Fig. 4.4, where each band corresponds to a different strain-hardening coefficient n setting the limit between the two contact regimes. Note that $n = 0$ does not appear in the map, since all perfectly-plastic solids are found to be fully plastic within the ranges of mechanical properties under study. Since the simulations pertain to $\theta = 70.3°$, the role of tip angle on the active contact regime is not considered here. As present tip angle induces the same contact area – penetration depth relation as pyramidal tips, the contact deformation map may be regarded to apply to Vickers and Berkovich indentation. Interpretation of the contact deformation map is given next on the basis of the plastic flow patterns induced underneath the indenter.

4.3 Plastic flow patterns underneath conical indenters

Important features underlying the active contact regime are the plastic flow patterns induced around the imprint. The slip-line analysis for rigid–perfectly-plastic solids already accounted for the experimental findings in strain-hardened pure metals, where plastic flow extends outwards from the center of the imprint generating a pileup effect at the contact periphery. On the other hand, elastic contacts are characterized by large sinking-in effects, exhibiting a deformation pattern that is embedded underneath the contact surface. While the above represent limiting cases of pileup and sinking-in effects, the development of a detailed understanding of the influence of strain hardening and yield strength in the plastic flow patterns is non-trivial.

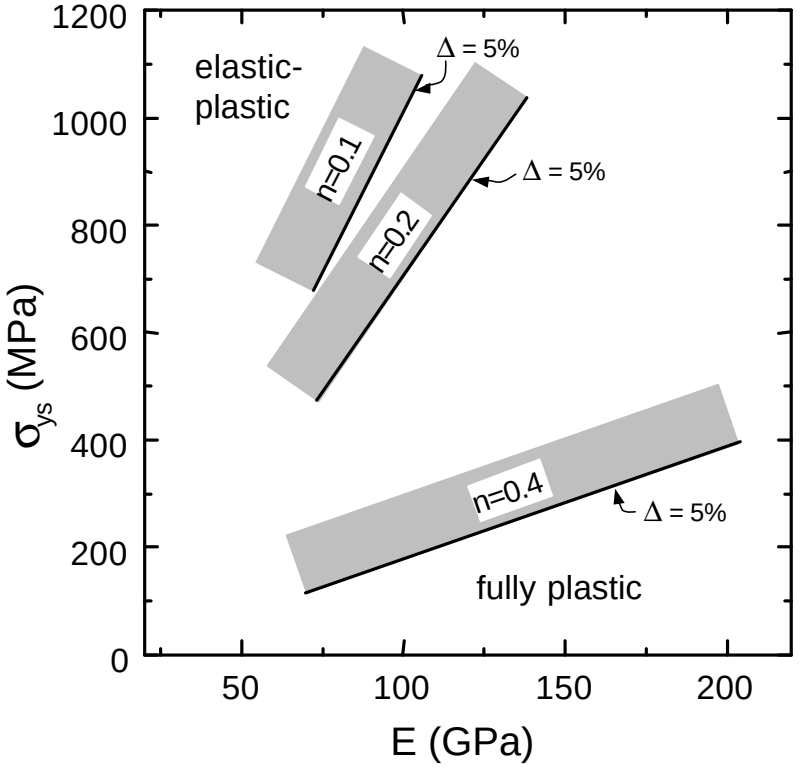

Figure 4.4: Contact deformation map setting the boundaries between the elasto–plastic transition and the fully plastic contact regime for elastic–power-law strain hardening solids. Materials below each of the bands, representing different values of the strain hardening coefficient n, exhibit a fully plastic contact response. Materials above each of the bands undergo an elasto-plastic transition. The solid lines below the bands mark the commencement of a fully plastic response where sinking-in still occurs. Δ is the relative error between the value of hardness obtained from the simulations and the value of hardness predicted with Tabor's equation ($H = 2.7\sigma_{0.1}$). Solids located right below the bands exhibit $\Delta < 5\%$. As σ_{ys} is further decreased, Δ tends to 1 % and the solids exhibit pileup effects rather than sinking-in. The map exclusively pertains to a conical indenter with included half-apex angle of 70.3°.

The distinctive features of the equivalent plastic stress fields, which define the plastic zone size and shape, show that the evolution towards the fully plastic mode is gradual when moving along the map in Fig. 4.4. In the following, we describe the general trends of this evolution.

(i) For large values of n and $\sigma_{\rm ys}$, the equivalent stress fields are concentrated right beneath the indenter's tip, and have a rather hemispherical shape which resembles that in elastic contacts (see Figs. 4.5(a) and 4.6(a)). Also the effect of elasticity is demonstrated in the flow patterns, as they are found to be considerably radial as in purely elastic solids (Fig. 4.7(a)). The solids exhibit a tendency to sink-in, and ratio $H/\sigma_{\rm ys}$ lies well below 2.70. The contact regime is thus regarded as elasto-plastic.

(ii) As n and $\sigma_{\rm ys}$ decrease, the plastic zone breaks out to the free surface leading to an uncontained deformation mode. Under such contact conditions, the plastic zone does not bend towards the indenter close to the free surface, as in the case of the above elastic-plastic regime (see Fig. 4.5(b) and the transition from Fig. 4.6(a) to 4.6(b)). Furthermore, a slight tendency of the plastic zone to bend outwards from the tip is exhibited in most solids. Since Tabor's hardness equation becomes valid with an accuracy better than 5%, the above plastic features are regarded to set the domain for the fully plastic contact regime. (This is the case of solids located at the lower side of the bands in the contact deformation map —label $\Delta = 5\%$ in Fig. 4.4—.) The contact deformation mode is still one where sinking-in occurs regardless of the uncontained plastic flow features exhibited by the solid. The flow patterns reveal that the elasto-plastic mode is evolving to a fully plastic one as the flow direction gradually looses its radiality (consider solids evolving from Fig. 4.7(a) to 4.7(b)). Indeed, only the material points lying close to the z-axis maintain a certain radial flow.

(iii) For even lower values of n and $\sigma_{\rm ys}$, the material at the contact boundary flows primarily towards the free surface thus leading to the development of pileup (see Fig. 4.7(b)). As a result of such deformation mode, the plastic zone presents a marked tendency to bend outwards from the indenter close to the free surface (see Figs. 4.5(c) and 4.6(c)). In such fully plastic contact regime where sinking-in is no longer detected,

the difference between hardness values from the finite element simulations and those from Tabor's equation is reduced to 1%. These trends are consistent with those assumed in fully-plastic analysis made by recourse to the slip-line theory.

The above findings, predicated by gradually changing yield strength σ_{ys} and hardening coefficient n, are also observed as Young modulus E is varied and the remaining properties are kept constant. In this sense, the fully-plastic regime predominates for large values of E, underlying small elastic contributions to the overall contact response. The stress fields in Fig. 4.8 illustrate the evolution of the contact regimes with E for fixed values of σ_{ys} and n.

Using the concept of the characteristic stress and strain, one may readily replace σ_{ys} by σ_r in the aforementioned dimensionless parameter $E\ \mathrm{cotan}\theta/\sigma_{ys}$ to evaluate the contact response in strain hardening solids ($n > 0$). The simulations used to build the contact deformation map thus indicate that $E/\sigma_r > 110$ ensures the prevalence of the fully-plastic regime for $\theta = 70.3°$. Interestingly, Johnson anticipated that the fully plastic regime shall commence at $E\ \mathrm{cotan}\theta/\sigma_{ys} > 50$ (which is approximately 135 for a cone with $\theta = 70.3°$). Nevertheless, this limit was not confirmed through the present simulations as all perfectly-plastic solids exhibited a fully plastic regime, fulfilling $H = 2.57\sigma_{ys}$. Finally, $E/\sigma_r > 400$ ensured development of the fully-plastic regime where pileup effects prevail.

4.4 Summary

Systematic finite element simulations in elastic-strain hardening solids allowed us to examine the distinctive features of the contact deformation regimes proposed by Johnson for perfectly plastic media. The stress fields developing underneath the indenter indicate that each contact deformation regime is associated with a particular flow pattern. The analysis of the size and shape of the plastic zone characterizes the evolution from an elasto-plastic mode, to a fully-plastic one where sinking-in occurs, to a fully-plastic regime where material pileup prevails. Such evolution occurs as Young modulus E is increased or, alternatively, as yield strength σ_{ys} and hardening coefficient n are decreased.

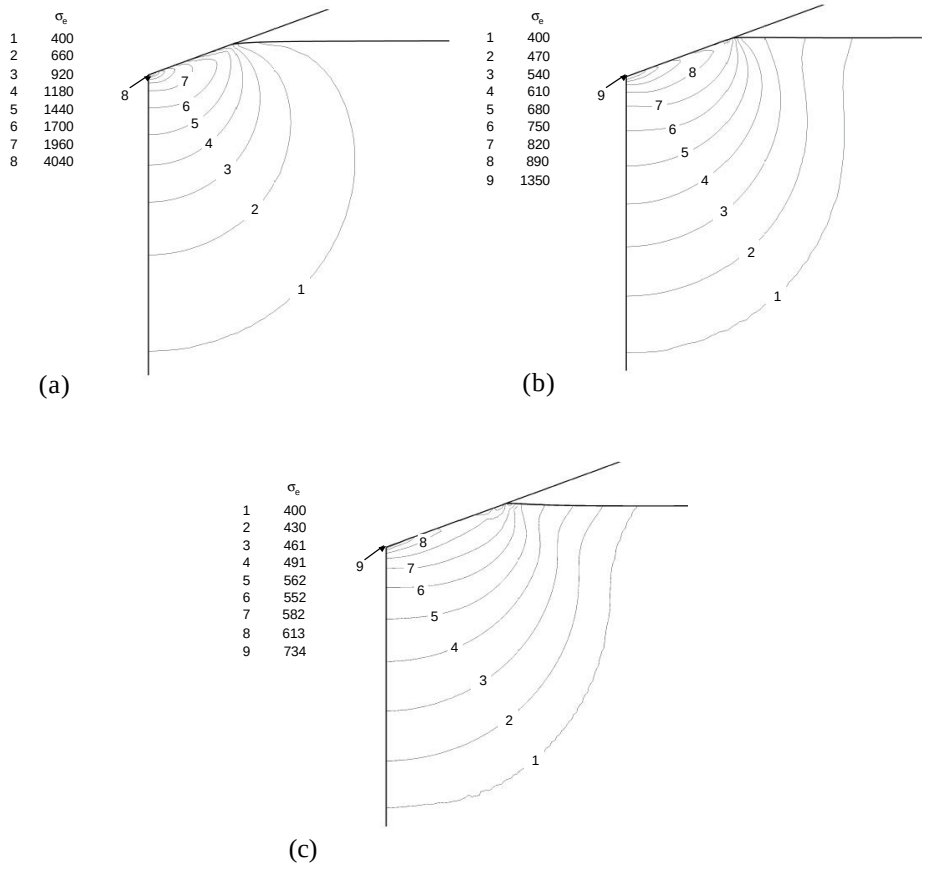

Figure 4.5: Isocontours of equivalent plastic stress for solids with with $\sigma_{\mathrm{ys}} = 400$ MPa and $E = 70$ GPa: (a) elasto-plastic transition for $n = 0.4$; (b) fully plastic contact response for $n = 0.2$; (c) fully plastic regime where piling-up predominates for $n = 0.1$.

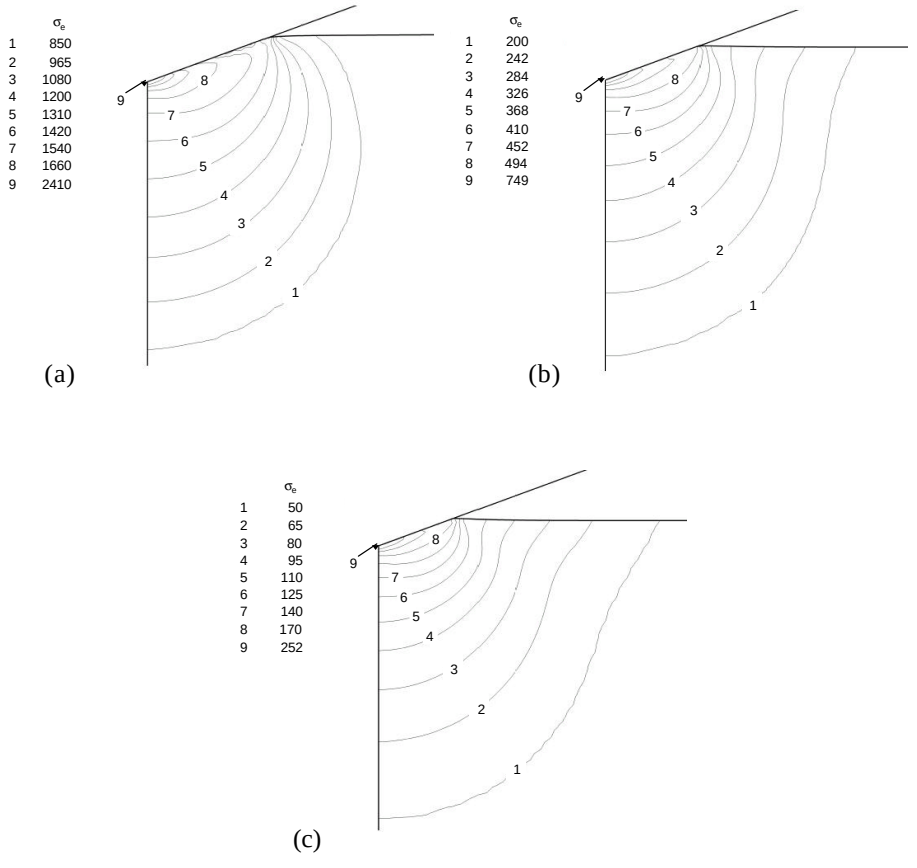

Figure 4.6: Isocontours of equivalent plastic stress for solids with $E = 70$ GPa and $n = 0.2$: (a) elasto-plastic transition for $\sigma_{\text{ys}} = 850$ MPa; (b) fully plastic contact response for $\sigma_{\text{ys}} = 200$ MPa; (c) fully plastic regime where piling-up predominates for $\sigma_{\text{ys}} = 50$ MPa.

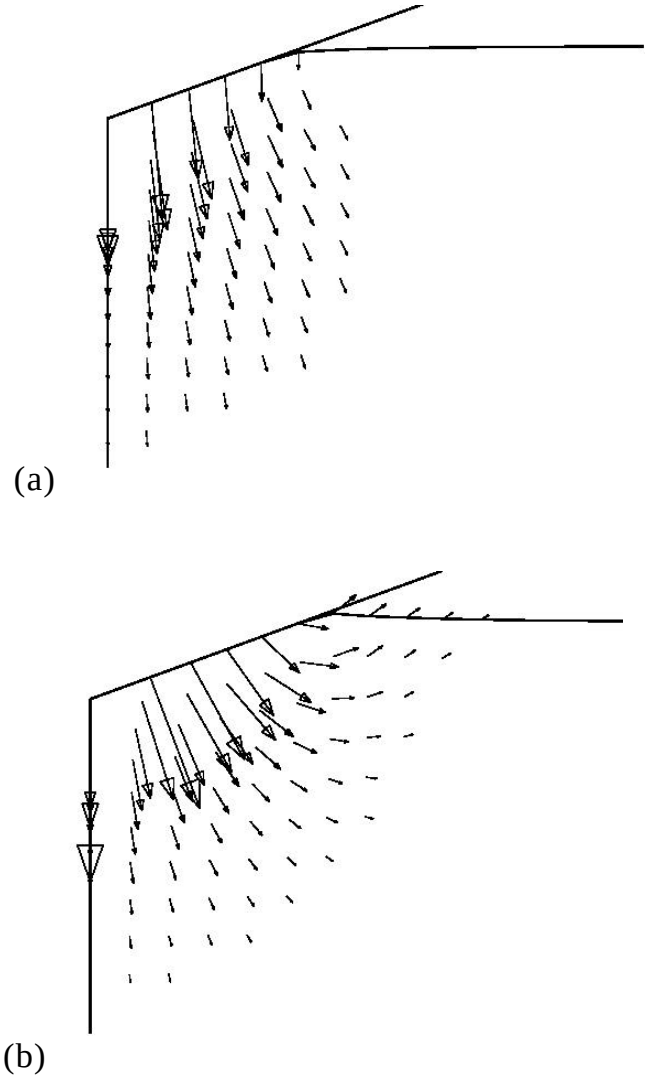

Figure 4.7: Flow patterns for (a) a solid deforming within the elasto-plastic transition with $E/\sigma_{\mathrm{ys}} = 36$, and (b) a fully plastic solid where $E/\sigma_{\mathrm{ys}} = 521$.

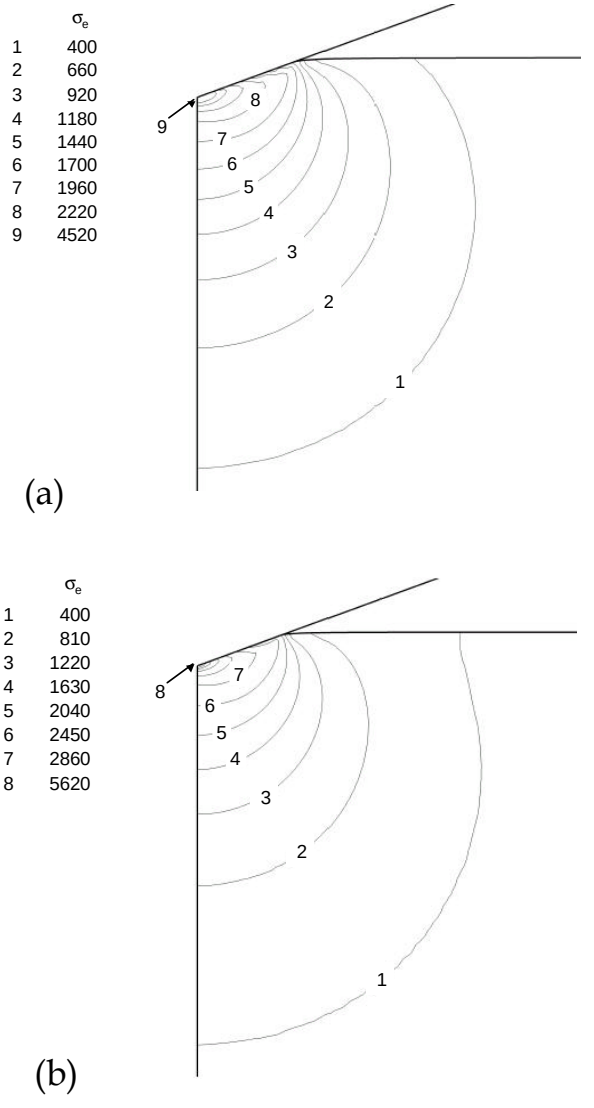

Figure 4.8: Isocontours of equivalent plastic stress for solids with $\sigma_{\rm ys} = 400$ MPa and $n = 0.4$: (a) elasto-plastic transition for $E = 110$ GPa ; (b) fully plastic contact response for $E = 200$ GPa.

These findings are the backbone of the contact deformation map developed in this chapter, which predicts the actual contact regime for a given set of mechanical properties. The map is strictly valid for conical indentation with a tip whose apical angle is 70.3°. Since this tip has the same penetration depth to contact area relation as Vickers and Berkovich indenters, the results are hopefully valid to such pyramidal tips.

The plastic zone within the elasto-plastic transition is found to be contained underneath the indenter and to have a rather spherical shape, resembling that in elastic contacts. Fully plastic materials obeying Tabor's hardness equation exhibit a spreading of the plastic zone. Thus, while elasticity governs the elasto-plastic transition, extensive plastic flow controls the fully plastic regime. The flow patterns in the elasto-plastic mode are almost radial, leading to the development of sinking-in effects. However, the material flows outwards within the fully plastic regime, usually leading to pileup development at the contact periphery.

Hardness is found to correlate well with to the uniaxial mechanical properties through Tabor's equation, which is an accurate extension of slip-line analysis to strain-hardening solids. Thus, slip-line hardness equation $H = C_{\mathrm{sl}}\ \sigma_{\mathrm{ys}}$ is modified as $H = 2.7\ \sigma_{\mathrm{r}}$ to account for the strain-hardening effects (where uniaxial stress σ_{r} corresponds to a material independent uniaxial strain ϵ_{r} of 0.10). It is remarked that neither C nor ϵ_{r} depend on the mechanical properties of the material.

Using the concept of the representative stress σ_{r}, dimensionless parameter E/σ_{ys} is modified as E/σ_{r} to establish the limit between the fully plastic and the elasto-plastic contact regimes. According to present simulations, $E/\sigma_{\mathrm{r}} < 110$ comprises all solids deforming within the elasto-plastic transition, and $E/\sigma_{\mathrm{r}} > 400$ ensures that the contact response is fully plastic where large pileup effects develop around the indenter. Intermediate values of E/σ_{r} are representative of solids which, while fulfilling Tabor's fully plastic hardness equation within a 5% error, exhibit slight sinking-in effects. It is remarkable that all perfectly-plastic materials used in the simulations deformed within the fully plastic regime, so that the bounds anticipated by Johnson for $n = 0$ could not be confirmed. This indicates that in elastic–perfectly plastic solids, the elasto-plastic

transition shall occur for extremely large values of σ_{ys} or small values of E, which are not realistic to metallic materials.

Chapter 5

Methodology for mechanical property extraction

In the previous chapter we have established that the contact response of materials can be evaluated through hardness measurements and the assessment of the amount of vertical deformation (pileup or sinking-in) occurring around the imprint. With the advent of instrumented indentation, continuous measurements of the applied load (P)–penetration depth (h_s) of the indenter into the material can be routinely performed. Although a significant amount of research efforts have been devoted to find correlations between the parameters describing the $P - h_s$ curves and the uniaxial mechanical properties of the solid [2; 4; 5; 23; 24; 25; 26; 30; 32; 60; 65; 74; 78], little attention has been given to conduct a similar line of analysis in the context of hardness H and surface deformation parameter α. Such investigation is increasingly relevant as it is now possible to measure contact area and the topographic features of the imprint even in the nano-indentation range by recourse to AFM (atomic force microscopy) techniques. Knowledge of physically-based parameters describing the imprint's size and shape (such as H and α) may thus provide a complementary information central to the analysis of instrumented indentation P–h_s curves.

In §4 we found that the simple hardness equation proposed by Tabor prescribes the contact response in strain-hardening materials whose deformation features are plastically

dominated. However, when elasticity plays a fundamental role in the contact response, hardness deviates from this simple fully plastic relation. Hence, in this chapter we first aim at deriving an equation which, within the elasto-plastic transition, correlates hardness with the uniaxial stress-strain curve. In doing so, we rely on the findings by Johnson for elastic–perfectly plastic solids. Based on a best fit function to the present finite element simulations, a general hardness equation is then derived which covers both Tabor's regime and the elasto-plastic transition. Attention is then given to the dependency of surface deformation parameter α with uniaxial mechanical properties. (Note that in §4 we already found that pileup and sinking-in characterize the deformation regime developing underneath the indenter, as pileup is exclusively indicative of a fully plastic mode and sinking-in denotes the effect of elastoplasticity.) Finally, derived formulations are used to develop a methodology for the extraction of the yield strength σ_{ys} and hardening parameter n using H, α, and the Young's modulus E as input variables. On the final part of the chapter, a discussion is given on the complementarity between present line of thought and methodologies where the mechanical properties are exclusively obtained through P–h_{s} curve analysis.

5.1 The role of elasticity in hardness

A general framework to evaluate the effect of elasticity on indentation experiments was given by Johnson [47]. Based upon the experimental investigations by Bishop [10], Marsh [58], and Hirst and co-workers [44], along with the theoretical developments by Hill [42], Johnson found that for solids deforming within the elasto-plastic transition hardness is given by

$$\frac{H}{\sigma_{\mathrm{ys}}} = \frac{4}{3} + \frac{2}{3}\ln\left(\frac{1}{3}\frac{E}{\sigma_{\mathrm{ys}}}\mathrm{cotan}\theta\right) . \tag{5.1}$$

Ratio H/σ_{ys} thus increases with E/σ_{ys} until saturation occurs at a value of about 3 in accordance to Tabor's findings. To derive Eq. (5.1), Johnson used an analogy between indentation and the expansion of a spherical cavity in an infinite medium, originally formulated in [10; 21; 28; 42; 47]. Johnson's indentation model considers a *core* of

radius a_s which replaces the expanding cavity. The core thus comprises the indenter and the material encased within radius a_s (see Fig. 5.1). It is assumed to be hydrostatic and to induce radial flow on the surrounding material. Also, plastic deformations are taken to be incompressible, $\nu = 0.5$, which simplifies the mathematical treatment. A detailed analysis of this model is given in §7.

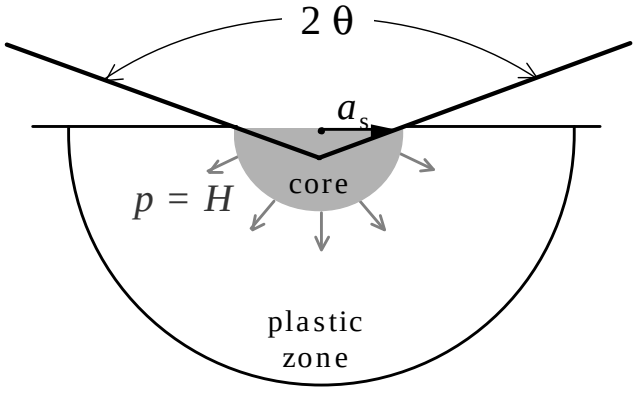

Figure 5.1: Johnson's indentation model and definition of the core of radius a_s exerting a hydrostatic pressure $p = H$ to the surrounding material.

It is important to point out that the elasto-plastic transition *as well as* the fully plastic regime are influenced by the elastic properties of the indented material. Tabor's hardness equation derived in the previous chapter reads

$$H = C\sigma_r = 2.7\sigma_\circ 0.1^n \ , \tag{5.2}$$

where $\sigma_\circ = {\sigma_{ys}}^{1-n} E^n$ for continuity of the stress-strain curve at ϵ_{ys} (see equation A.21 in Appendix A). Therefore, elastic modulus E affects hardness in the fully plastic regime as it implicitly enters into Tabor's equation. To illustrate this influence, take a variation of E from 70 GPa to 200 GPa for fixed values of σ_{ys} and n. Within the range of mechanical properties under study, such a variation leads to a maximum variation of 30% in σ_r, changing hardness H by the same amount. This finding cannot be attributed to

the contribution of elastic deformations to the total characteristic strain ϵ_r since, in most metallic materials, elastic deformations are insignificant as compared to $\epsilon_r = 0.10$. The effect of the Young's modulus on hardness is thus intrinsic to the constitutive equation used to parameterize the stress-strain curve (Eq.(A.21)).

In Fig. 5.2, we depict pressure distributions p of different solids deforming within the fully plastic regime. It is readily seen that as E increases, there is an associated increase in p. Since hardness is the mean value of the pressure distribution over the whole contact area (see Section 1.1.2), E acts as a scaling factor for p for a fixed set of σ_{ys} and n. This aspect becomes evident from the distributions in Fig. 5.2 because as E increases, the overall *shape* of the pressure distribution remains constant while its mean value (p_m) is gradually increased. The greatest influence of E on hardness is found to occur in solids with large values of hardening coefficient n and yield strength σ_{ys}. Note that the distributions in Fig. 5.2 are plotted in terms of the normalized contact radius r/a, where a is the contact radius and r the radial position from the center of the imprint (see Fig. 1.3).

5.2 Hardness equations for conical indentation

In the following, we use the concept of the representative stress σ_r to derive a hardness equation for the elasto-plastic transition in strain hardening solids. Thus, in the spirit of Tabor's findings, we seek to capture the role of strain hardening parameter n through the concept of the representative stress σ_r. In addition to the solids indicated in §3, finite element simulations were performed in solids whose contact response is anticipated to lie within the elastoplastic transition. The mechanical properties of these solids, compiled in Table 5.1, are relevant to titanium alloys (1), nickel-based superalloys and martensitic steels (2, 3). Other materials (4, 5, and 6) were also modelled for completeness.

Following Johnson's model, we use the mathematical form of Eq.(5.1), replacing yield strength by representative stress σ_r to account for strain-hardening. Hence, we fit hardness values from the simulations to an equation of the form

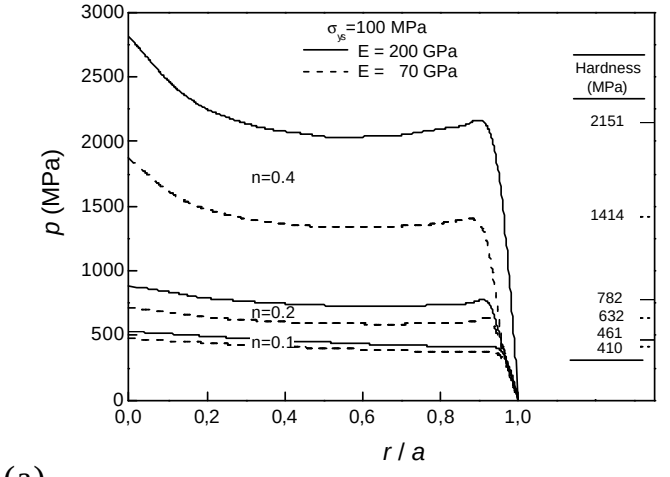

(a)

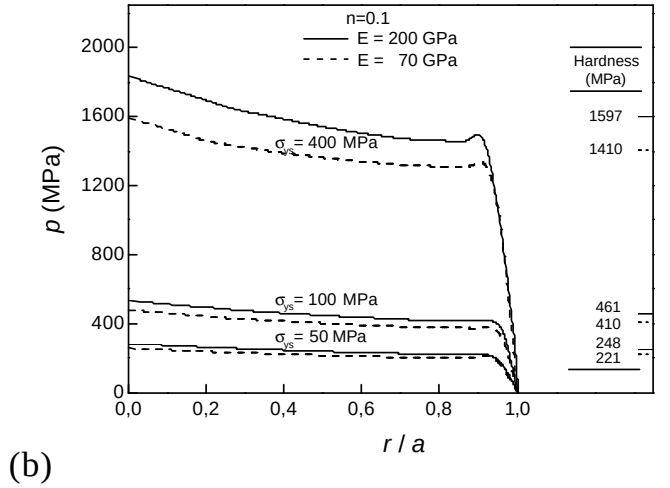

(b)

Figure 5.2: Finite element simulations showing the influence of Young's modulus E on contact pressure distributions p in solids where $\ln(E/\sigma_{\mathrm{r}}) > 4.5$. The results are for simulations with identical (a) yield stress σ_{ys}, and (b) hardening coefficient n. Note that hardness H quoted in the figure is given by the mean value of the pressure distribution (see Section 1.1.2.

	σ_{ys} (MPa)	n	E (GPa)	H (cone) * present simulations (GPa)
Ti alloys (1)	400	0.4	110	3.83
Ti alloys (1)	1000	0.2	110	4.14
Ti alloys (1)	1200	0.2	100	4.67
	2000	0.2	200	8.12
Nickel-based superalloys and martensitic steels (2, 3)	1000	0.4	200	8.25
	800	0.4	200	7.36
	2000	0.4	200	12.19
(4)	850	0.2	110	3.73
(5)	700	0.1	70	2.27
(6)	1200	0.4	100	6.71

* calculated considering surface deformation effects

Table 5.1: Mechanical properties of the additional solids modelled to find a hardness equation within the elasto-plastic transition.

$$\frac{H}{\sigma_{\mathrm{r}}} = A \; + \; B \, \ln\left(\frac{E}{\sigma_{\mathrm{r}}}\right) \; , \tag{5.3}$$

where the effect of cone angle is embedded into constant A (θ was fixed at 70.3° in the simulations). Constants A and B are thus found through curve-fitting, taking the values of 1.440 and 0.264, respectively. Directing attention to Fig. 5.3, one can easily identify the elasto-plastic transition where Eq.(5.3) rules the contact response, Tabor's fully plastic regime as the plateau corresponding to $H/\sigma_{\mathrm{r}} = 2.7$, and locate the limit between them at $E/\sigma_{\mathrm{r}} \simeq 110$ as indicated in Section 4.3. The three zones in the figure indicate the three stages of the evolution of the contact regimes: I is for the elasto-plastic transition, II corresponds to the fully plastic mode where sinking-in occurs, and III refers to fully plastic solids where piling-up prevails (§4).

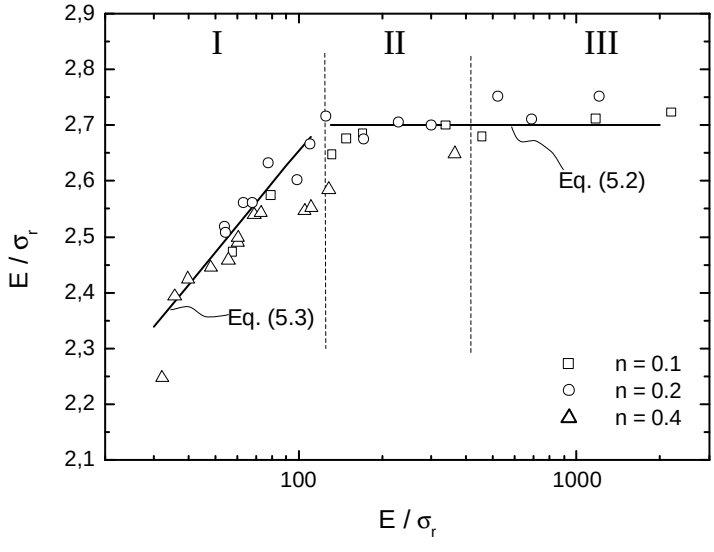

Figure 5.3: Correlation between hardness and the uniaxial mechanical response of elastic–strain hardening solids. I, elasto-plastic transition; II, fully plastic regime; III, fully plastic regime where piling-up predominates over sinking-in.

Although the concept of the representative stress σ_{r} is again key to correlate hardness with the mechanical properties of the solid, this approach is debatable when dealing with

solids deforming in the elasto-plastic transition. Obviously clarification is needed to use $\sigma_{\rm r}$, which is defined at a strain where $H = C\sigma_{\rm r}$, in the analysis of hardness within the elasto-plastic transition. Nevertheless, in light of present simulations, $\sigma_{\rm r}$ is still an applicable concept as it allows one to implicitly capture the effect of strain hardening on hardness through the functional form of Eq. (5.3). Since the constants in Eq.(5.3) are obtained through curve-fitting, this relation is anticipated to be valid only in the range of $30 < E/\sigma_{\rm r} < 110$, to which present fit is limited.

Since hardness H does not depend on penetration depth, for a fixed cone angle θ one may write $H = H(E, \sigma_{\rm ys}, n)$, so that application of the Π theorem in functional analysis (see Section 1.2) yields

$$\frac{H}{\sigma_{\rm ys}} = f_{\circ}\left(\frac{E}{\sigma_{\rm ys}}, n\right) \ . \tag{5.4}$$

Interestingly, it is found that the results of the finite element simulations can be fitted through a single equation, Fig. 5.4, which provides the ratio of hardness to representative stress ($H/\sigma_{\rm r}$) for *all* strain-hardening solids ($n > 0$). Hence,

$$\frac{H}{\sigma_{\rm r}} = f_1\left(\frac{E}{\sigma_{\rm r}}\right) \ . \tag{5.5}$$

The solid line in Fig. 5.4 corresponds to the following best-fit function

$$\begin{aligned}\frac{H}{\sigma_{\rm r}} = -0.0023\left[\ln\left(\frac{E}{\sigma_{\rm r}}\right)\right]^4 + 0.0647\left[\ln\left(\frac{E}{\sigma_{\rm r}}\right)\right]^3 - 0.6817\left[\ln\left(\frac{E}{\sigma_{\rm r}}\right)\right]^2 \\ +3.1968\left[\ln\left(\frac{E}{\sigma_{\rm r}}\right)\right] - 2.9261 \ ,\end{aligned} \tag{5.6}$$

which provides hardness estimates with an accuracy better than 3% irrespectively of the contact regime. This equation considers the combined influence of elasticity and plasticity in hardness, and is valid for any elastic–power-law plastic material whose properties range within the limits of Fig. 5.4 (i.e., $3.5 < \ln(E/\sigma_{\rm r}) < 8$).

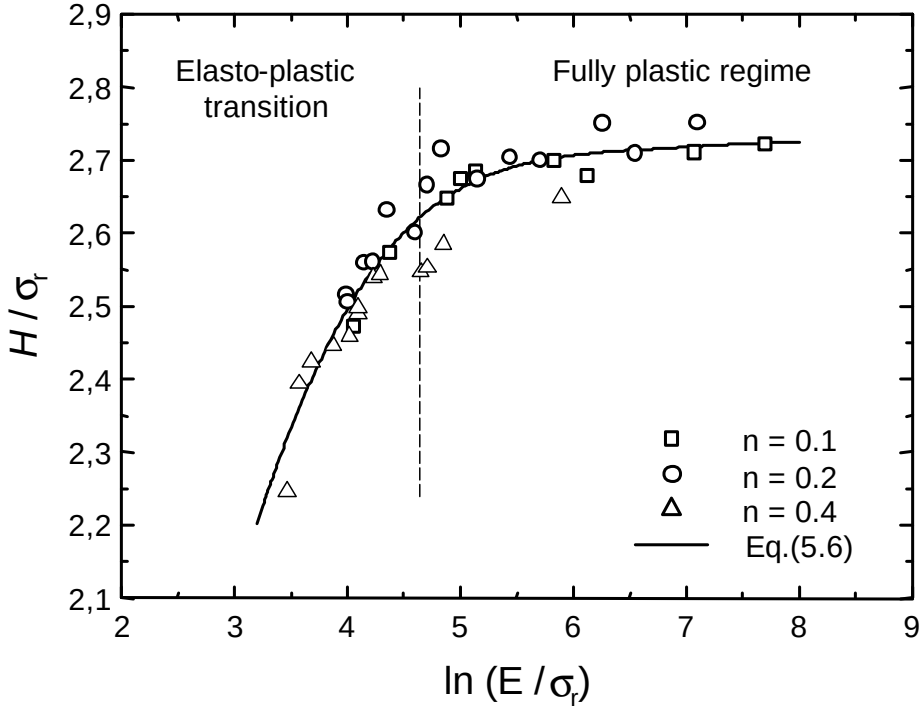

Figure 5.4: General correlation between H/σ_{r} and E/σ_{r} for all strain hardening solids ($n > 0$).

5.3 Influence of mechanical properties on the pileup and sinking-in responses

In addition to hardness, a fundamental parameter that characterizes the contact response is the amount vertical deformation occurring around the contact boundary. As indicated in Sections 1.1.1 and 1.1.2, the material may pile up or sink-in at the periphery of the imprint depending on the mechanical properties of the solid and the geometry of the indenter. The finite element simulations suggest that such deformation modes follow theoretical predictions in the sense that the more elastic the solid, the larger the tendency to sink-in [46]. The evolution to the fully plastic regime (marked by small values of n and $\sigma_{\rm ys}$) is thus followed by the development of pileup.

Parameter $\sqrt{\alpha}$ prescribes the ratio of material that piles up ($\sqrt{\alpha} > 1$) or sinks-in ($\sqrt{\alpha} < 1$), as defined in Section 1.1.1:

$$\sqrt{\alpha} = \frac{h}{h_{\rm s}} = \left(\frac{A}{A_{\rm s}}\right)^{1/2}, \tag{5.7}$$

where h is the penetration depth of the indenter as measured from the true contact periphery, and $h_{\rm s}$ is the penetration depth from the undeformed surface, Fig. 1.1. Note that one can also define α as the ratio of the true contact area (A) to the geometrical area ($A_{\rm s}$), Section 1.1.1.

The flow patterns described in Section 4.3 underly the evolution from sinking-in to pileup as the material becomes increasingly plastic. Solids deforming within the elasto-plastic transition are prone to sink-in because elasticity prevents the outwards flow from occurring. Deformation is thus more contained underneath the indenter (§4). When the influence of elastic strains decreases, either by increasing Young's modulus E or decreasing hardening coefficient n and yield strength $\sigma_{\rm ys}$, the solid is free to flow outwards from the indenter's tip leading to the development of pileup. Following previous results by Matthews [61] and by Alcalá *et al.* [3], we found that in the fully plastic regime deformation of the indented surface depends primarily on the value of n, while it is also affected by $\sigma_{\rm ys}$ and E. These results are shown in Fig. 5.5, where the influence

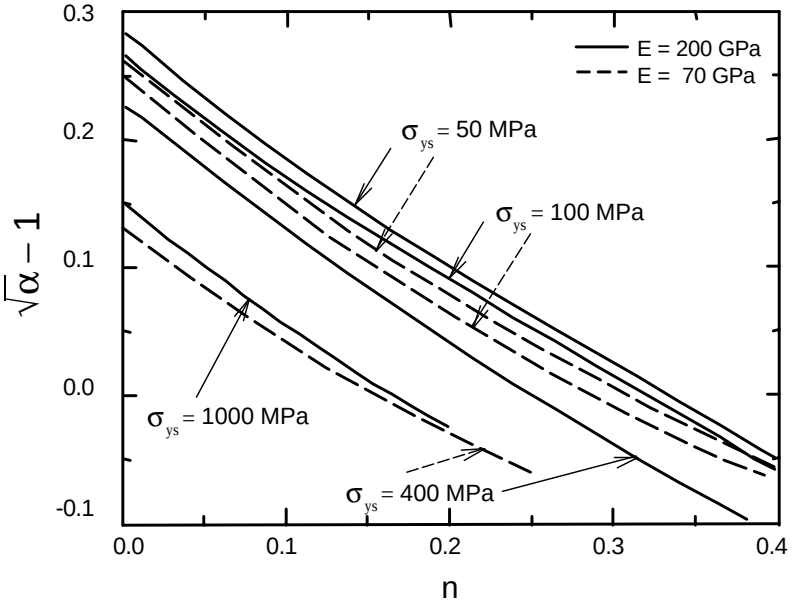

Figure 5.5: Correlation between the amount of piling-up and sinking-in ($\sqrt{\alpha} - 1$) and strain hardening coefficient n. The results relate to the fully plastic contact regime. Note the influence of σ_{ys} and E on surface deformation, and that even within the fully plastic regime it is possible to find solids undergoing sinking-in ($\sqrt{\alpha} - 1 < 0$).

of elasticity is clearly evidenced even though the simulations in the figure exclusively concern fully plastic solids. Therefore, as it was already established in Section 4.3, Fig. 5.5 illustrates that the development of sinking-in may not necessarily denote the attainment of the elasto-plastic transition. Interestingly, the trends described in the contact deformation map are also evident in Fig. 5.5, since a small E and a large σ_{ys} favor sinking-in.

Previous studies on the surface deformation modes around spherical indentations concluded that parameter α only depended on the strain-hardening coefficient n [3; 11; 43; 61; 64]. These results are applicable to *rigid*–power-law hardening materials, in which the elastic part of the deformations is neglected. The difference between the present work and the aforementioned investigations is thus justified on the grounds that the current simulations pertain to materials with non-vanishing σ_{ys} and finite value of E.

Using the same procedure as that employed to obtain a general hardness equation, Section 5.2, we seek to find a general relationship for the dependency of surface deformation parameter α on the mechanical properties of the solid. For a given sharp indenter, we thus write $\alpha = \alpha(E, \sigma_{\mathrm{ys}}, n)$. Applying the Π theorem in functional analysis, it follows that

$$\alpha = g_{\circ}\left(\frac{E}{\sigma_{\mathrm{ys}}}, n\right) \ , \tag{5.8}$$

which can be equivalently rewritten as

$$\alpha = g_1\left(E/\sigma_{\mathrm{r}}, n\right) \ . \tag{5.9}$$

A best-fit function to g_1 for a conical indenter of $\theta = 70.3^{\circ}$ is

$$\sqrt{\alpha} = R + Se^{-(\sigma_{\mathrm{r}}/E)/T} \ , \tag{5.10}$$

where coefficients R, S and T depend on strain-hardening parameter n. The dependency of these coefficients on n is captured through

$$R = 8.7760n^3 - 6.7180n^2 + 1.0478n + 0.8148 \ ,$$

$$S = -7.7892n^3 + 6.8690n^2 - 2.0273n + 0.4790 \ ,$$

$$T = -0.35359n^3 + 0.40038n^2 - 0.05926n + 0.01426 \ . \tag{5.11}$$

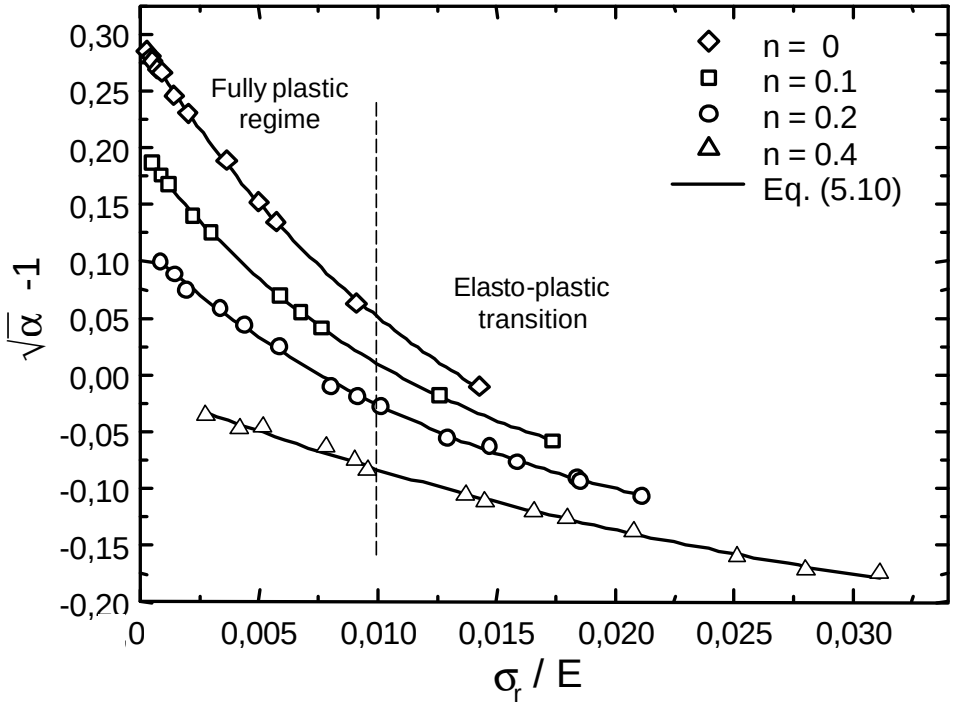

Figure 5.6: Correlation between surface deformation parameter $\sqrt{\alpha} - 1$ and uniaxial mechanical properties $E/\sigma_{\rm r}$ and n for all solids deforming within the fully plastic regime and the elasto-plastic transition.

The results in Fig. 5.6 show that Eq. (5.10) (solid lines) gives an extremely good representation to the data from the finite element simulations (symbols). In this regard, the maximum error in the estimation of $\sqrt{\alpha}$ from Eq.(5.10) is ± 0.01 for all solids whose properties are within those considered in the simulations. This error is negligible as

compared to the values of surface deformation parameter α for metallic materials, which range from 1.2 to 0.9.

5.4 Methodology to extract uniaxial mechanical properties

The development of general equations for hardness H (Eq.(5.6)) and for parameter α (Eq.(5.10)) allow one to develop a reverse procedure to extract the plastic properties of the indented solid from hardness tests. Since these equations are derived upon extensive finite element computations where the solids are taken to obey the J_2-flow plasticity model described in Appendix A, present methodology is limited to elastic–power-law plastic metallic materials. It is also restricted to indentations under frictionless conditions (extension to frictional contacts is given in §6).

The devised procedure is as follows:

(i) Evaluate parameter $\sqrt{\alpha}$ as indicated in Section 1.1.1. This can be performed through surface profilometry which maps the true area of the imprint. Notice that pileup and sinking-in have to be obtained at maximum load, since Eq.(5.10) correlates the mechanical properties to $\sqrt{\alpha}$ when the surface is deformed under maximum load. Linear elasticity indicates that although considerable elastic rebound occurs in the vertical direction, outwards deformation upon unloading from $P_{\max}$ is negligible (Section 3.3 and [3]). Thus, while there is little change in contact areas A and $A_{\rm s}$ during unloading, the same does not hold true for penetration depths h and $h_{\rm s}$. It is thus preferred to measure α from the ratio of contact areas (Eq. (5.7)) obtained, for instance, through conventional surface profilometry or atomic force microscopy (AFM), rather than from the ratio of residual penetration depths (Eq. (5.7)). Alternatively, access to the P–$h_{\rm s}$ curve of the material allows one to evaluate α through measurement of constant K from Kick's law ($P = K{h_{\rm s}}^2$, Eq. (1.7) in Section 1.1.1),

$$\alpha = \frac{K}{fH} \ , \tag{5.12}$$

where hardness H is evaluated as in (ii), and f is a geometrical constant depending on indenter's shape ($f = 24.50$ for the Vickers indenter and the 70.3° conical indenter, and 24.562 for the Berkovich tip).

(ii) Determine hardness H as

$$H = \frac{P}{A} \ , \tag{5.13}$$

where P is the applied load, and A is the true contact area accounting for pileup or sinking-in. The value of A can be obtained through conventional microscopy (dark areas in Fig. 3.5) or by mapping the indented surface in the same manner as described in the evaluation of parameter α.

(iii) Measure Young's modulus E. The elastic modulus can be obtained from unloading slope $\mathrm{d}P$ / $\mathrm{d}h_\mathrm{s}$ of the instrumented indentation curve, as indicated in Section 1.1.1. Alternative methods, such as ultrasound and impulse excitation techniques, can be used in the determination of E.

(iv) Use Eq.(5.6), H, and E to obtain representative stress σ_r.

(v) Solve Eq.(5.10) with the values of $\sqrt{\alpha}$, E, and σ_r to obtain n.

(vi) Calculate the value of the yield strength σ_ys through the uniaxial strain hardening model (Appendix A). That is,

$$\sigma_\mathrm{ys} = \frac{\sigma_\mathrm{r}}{E^n 0.1^n}^{\frac{1}{1-n}} \ . \tag{5.14}$$

According to the above methodology, the maximum error in inferred hardening coefficient n caused by an experimental scatter in $\sqrt{\alpha}$ of ± 0.025 lies within ± 0.07 for solids where $\sigma_\mathrm{r}/E < 0.01$. This error decreases for $n < 0.2$. In the same lines, the reverse methodology is more accurate in fully plastic solids than in materials with an increasing amount of elastoplasticity, as for $\sqrt{\alpha} < 0.95$ and $\sigma_\mathrm{r}/E < 0.015$ the curve in Fig. 5.6 flattens considerably. Slight statistical scatter in measured α is thus reflected as a considerable error in inferred properties.

5.5 Consistency with the existing indentation methodologies

An important issue in extracting mechanical properties from indentation experiments is the uniqueness of the solution. While the direct procedure of finding indentation parameters from the uniaxial properties has a straightforward solution, the reverse problem may be ill-posed, that is, there may be various solutions for a given set of indentation parameters [18; 26; 30]. Hence, a lack of uniqueness in inferred properties arises. Several authors proposed methodologies to characterize the mechanical response of solids from instrumented indentation measurements [26; 27; 30; 36; 39; 50; 74]; however, only few recent investigations have dealt with the possible multiplicity of solutions of inferred mechanical properties (see the discussion given by Cao and Lu [18], Cheng and Cheng [26], and Dao *et al.* [30]).

It is emphasized that the reverse procedure devised in this thesis leads to only one solution of inferred properties. That is, for a given set of E, H and α, there is only one combination of σ_{ys} and n that fulfills the equations. In this regard, functional analysis shows that Eq.(5.6) is a single-valued function of σ_{r} for the range of materials studied in the present work ($\ln(E/\sigma_{\mathrm{r}}) > 2$). Also, it is seen that Eq.(5.10) provides a single value of n for any given input of $\sqrt{\alpha}$ and σ_{r}/E.

We now compare the present methodology with that proposed by Dao and coworkers [30]. In that work, the authors conducted a thorough analysis of the P–h_{s} curves from finite element simulations upon the basis of the Π-theorem (see Section 1.2). They derived 6 dimensionless Π functions capturing the dependencies of the parameters from the P–h_{s} curve which shall be used to extract the mechanical properties of the material. The representative stress for Dao *et al.* is taken at a characteristic *plastic* strain ${\epsilon_{\mathrm{r}}}^{p}$ of 0.033, which differs from our *total* strain of $\epsilon_{\mathrm{r}} = 0.10$. Such a difference lies in the fact that Dao *et al.* define the representative stress so that ratio K/σ_{r} converges to a single curve for all n, whereas we find such master curve for ratio H/σ_{r}.

The following set of equations were derived by Dao *et al.* Note that only the parametrical dependencies are given since explicit best-fit functions from their simulations

are of no interest to the present discussion:

$$\begin{aligned}
\Pi_1 &= \frac{K}{\sigma_{0.033}} = \Pi_1\left(\frac{E^\star}{\sigma_{0.033}}\right) \\
\Pi_2 &= \frac{1}{E^\star h_{\max}}\frac{\mathrm{d}P}{\mathrm{d}h_\mathrm{s}}\bigg|_{h_{\max}} = \Pi_2\left(\frac{E^\star}{\sigma_{0.033}}, n\right) \\
\Pi_3 &= \frac{h_\mathrm{r}}{h_{\max}} = \Pi_3\left(\frac{\sigma_{0.033}}{E^\star}, n\right) \\
\Pi_4 &= \frac{H}{E^\star} \approx \Pi_4\left(\frac{h_\mathrm{r}}{h_{\max}}\right) \\
\Pi_5 &= \frac{W_\mathrm{pl}}{W_\mathrm{t}} = \Pi_5\left(\frac{h_\mathrm{r}}{h_{\max}}\right) \\
\Pi_6 &= \frac{1}{E^\star\sqrt{A_{\max}}}\frac{\mathrm{d}P}{\mathrm{d}h_\mathrm{s}}\bigg|_{h_{\max}} = c^\star \ .
\end{aligned} \tag{5.15}$$

The instrumented indentation variables in these equations are illustrated in Fig. 1.2; where W_t is the total work performed by the indenter during penetration (obtained through integration of Kick's law $P = K{h_\mathrm{s}}^2$ to maximum penetration depth ${h_{\max}}^2$), and W_pl is the plastic component of the total work [30]. Since H appears explicitly in the above Π functions, one can readily find connections between the method by Dao *et al.* and that proposed in this thesis. Starting with the loading slope, constant K from Kick's law is directly related to the product of hardness H and α as in Eq.(1.8). Concerning the unloading part of the curve, reduced Young's modulus $E^\star$ is obtained from the slope at peak load, $\mathrm{d}P/\mathrm{d}h_\mathrm{s}$, and the contact area at maximum load, $A_{\max}$, (see Eq. (1.5) which is the same as Π_6 in the work by Dao *et al.*). Note that this area is the same as that used in the calculation of hardness H. Obviously, as measured penetration depth h_s does not account for the development of pileup or sinking-in, parameter α enters implicitly into Π_6 and Π_4.

5.6 Experimental application of the methodology

The methodology devised herein is validated experimentally in the annealed copper and the two stainless steels in Table 3.1. With the procedure outlined in Section 5.4, we use

	Uniaxial properties		input			output	
	σ_{ys} † (MPa)	n	E (GPa)	H (GPa)	$\sqrt{\alpha}$ -1	σ_{ys} (MPa)	n
Annealed copper	20	0.52	110	0.52	-5 %	2.5	0.51
AISI 329 duplex stainless steel	525	0.17	190	2.21	8 %	448	0.14
SAF 2507 superduplex stainless steel	675	0.19	200	2.57	6 %	468	0.165

† measured directly in the uniaxial stress-strain curve. It is noted that some values may not lie within the power-law fit to this curve.

Table 5.2: Comparison between the uniaxial stress-strain curve and that obtained from the indentation methodology.

Young's modulus E, hardness H, and parameter $\sqrt{\alpha}$ as input variables to extract the uniaxial stress-strain curve of the solid.

The results of the methodology are presented in Table 5.2 and in the stress-strain curves in Fig. 5.7. It is found that the overall indentation stress-strain curve is in excellent agreement with the uniaxial curve. There is, however, a discrepancy between the exact values of the yield strength $\sigma_{\rm ys}$ obtained from uniaxial tests and those from the indentation methodology. This is because the value of $\sigma_{\rm ys}$ obtained through uniaxial tests does not strictly lie within the general relation $\sigma = \sigma_\circ \epsilon^n$, which is assumed in present methodology. On the other hand, variations in the value of n between the uniaxial tests and the indentation methodology are likely to be due to the presumption that the entire post-yield behavior is described with a unique value of n. This is an approximation which does not strictly hold in light of the present uniaxial tests. where the value of n reported in Table 5.2 represents an average over the complete stress-strain curve.

5.7 Summary

In this chapter we have derived relationships between uniaxial mechanical properties, hardness, and parameter α. In view of the finite element simulations, the final relationships are considerably accurate and do not require a notion on the active contact deformation regime ruling the indentation experiment. Using these equations, the Flow

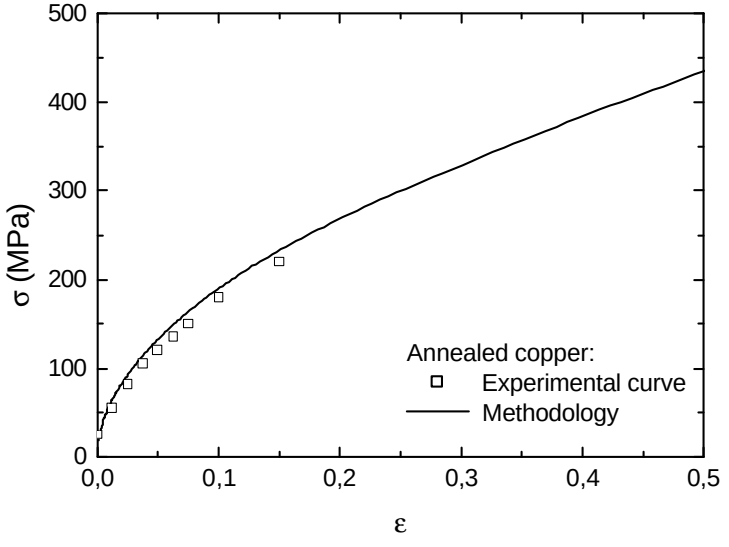
500
400
300
200
100
0
σ (MPa)
0,0
0,1
0,2
0,3
0,4
0,5
ε
Annealed copper:
Experimental curve
Methodology

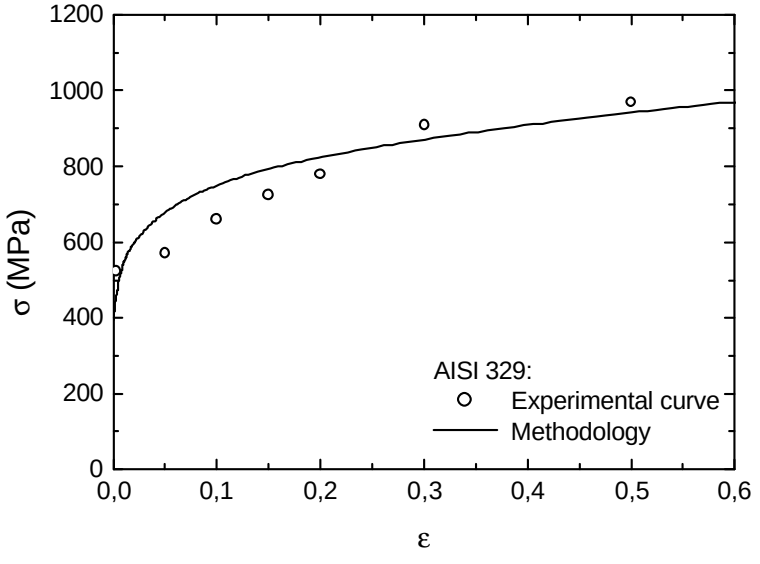
1200
1000
800
600
400
200
0
σ (MPa)
0,0
0,1
0,2
0,3
0,4
0,5
0,6
ε
AISI 329:
Experimental curve
Methodology

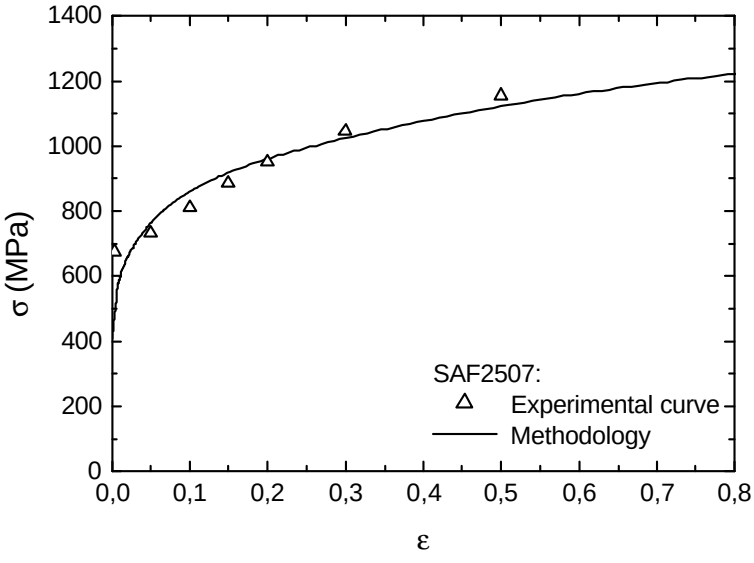

Figure 5.7: Stress-strain curves obtained from the uniaxial test (symbols) and from the indentation methodology (solid lines). The indentation curve fulfils Eq.(A.21), where the the values of σ_{ys} and n in Table 5.2 have been used.

Chart given in Fig. 5.8 summarizes the procedure devised herein to extract uniaxial plastic properties from parameters H, α and E. The procedure leads to a unique set of yield strength σ_{ys} and hardening parameter n from any given set of input parameters.

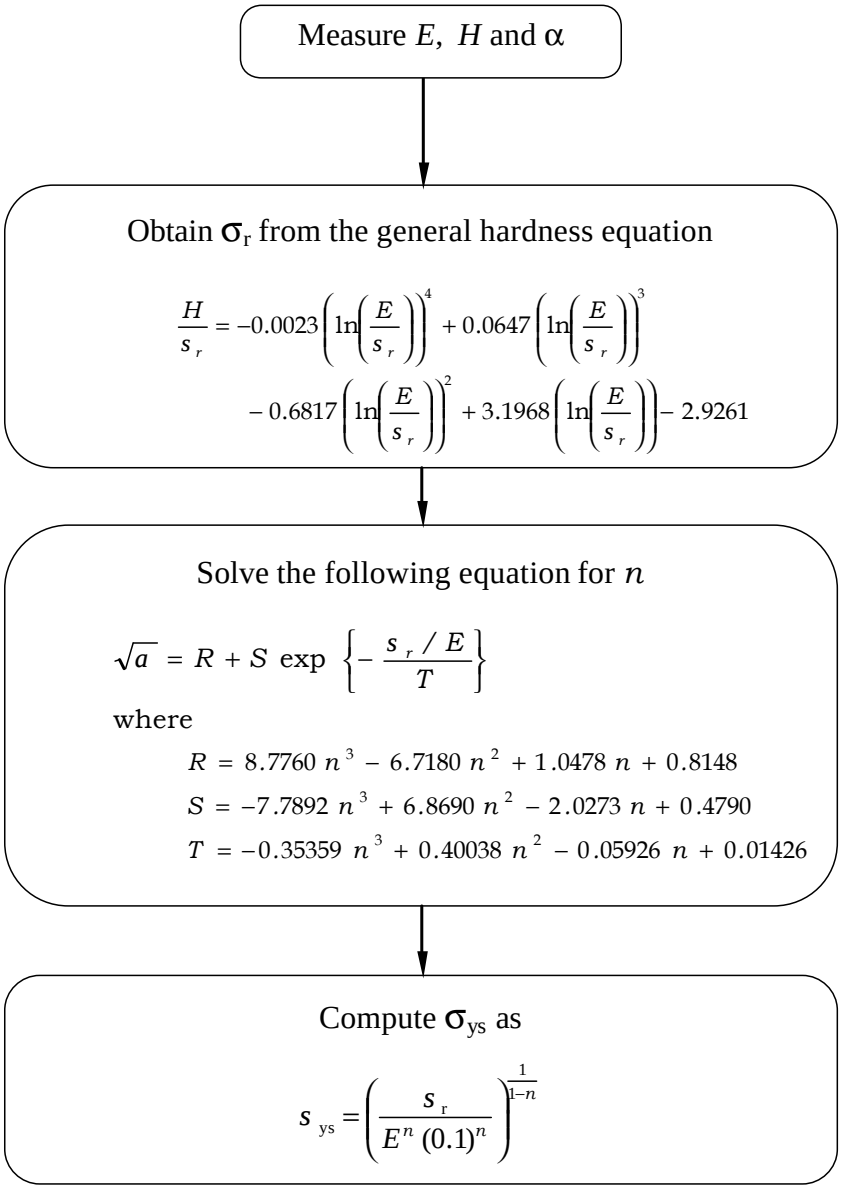

Figure 5.8: Flow chart to extract the plastic properties σ_{ys} and n from indentation experiments.

Chapter 6

The role of friction on sharp indentation

Frictional effects on sharp indentation of strain-hardening solids are examined in this chapter. The role of friction on sharp indentation was first studied by recourse to the theory of the slip-line field [46]. Since these early analyses concern rigid-perfectly plastic solids indented by rigid *wedges*, the specific results are of limited applicability to conventional pyramidal indentation of strain hardening materials. One shall bear in mind that for blunt wedges whose apical angle is $> 120°$, such early investigations already indicated that an increase of an utmost of $\sim 20\%$ in hardness occurs for adhesive contacts as compared to frictionless ones. More recently, the finite element method has been employed extensively to study the stress fields in frictionless contact problems, as well as to predict hardness and the development of surface deformation effects in indentation experiments (see, for instance, [8; 38; 39; 40; 43; 50; 51; 52]). By recourse to finite element simulations, some investigations have also shed light into the overall influence of friction in the contact response of *strain hardening solids* [19; 62]. These analyses suggest that friction may have a significant effect on the attainment of piling-up around the contact boundary and on the stress field underneath the indenter. They concern spherical indentation where either frictionless *or* adhesive contact conditions are at issue. Additional results for the indentation of solids exhibiting time-dependent

deformation under frictionless and adhesive conditions were obtained by Bower *et al.* [17].

Although the aforementioned studies underline the characteristic features of frictional contacts, a theoretical background to evaluate the influence of the friction coefficient on *sharp* indentation of strain hardening solids is still unavailable to our present knowledge. In this chapter we develop such a background, where the effect of the friction coefficient on (i) hardness, (ii) the development of surface deformation—i.e., the amount of pileup and sinking-in— and (iii) the shape of the P–h_s curves is specifically addressed. This is achieved through extensive finite element simulations where plastic flow features for different friction coefficients are considered in detail. This chapter ends with a methodology that extends the one given in §5 to deal with the role of friction in mechanical property extractions.

6.1 Experiments and computations

6.1.1 Friction experiments

The friction coefficient μ between diamond and the metallic materials was ~ 0.15. Measurement of μ was performed sliding a spherical tip of diamond, whose radius of curvature is 100 μm, over a distance of 1 mm across the polished surfaces of the metals. The applied normal load was 1 N and the sliding velocity was ~ 1 μm/s. Such relatively slow sliding velocity was selected to measure a friction coefficient that is as close as possible to the static (largest) one, which is anticipated to rule present indentation experiments (Section 6.1.2). Upon removal of the diamond tip, it was not possible to detect scratches at the polished surfaces of the metals. The measured friction coefficient confirms the belief that the value of μ between well-polished metallic surfaces and diamond lies within 0.10 to 0.15 [73].

6.1.2 Finite element simulations

Frictional effects were accounted for in the finite element simulations through an isotropic Coulomb model. Thus, the maximum local shear stress acting at the interface, τ_c, is

given by

$$\tau_{\mathrm{c}} = \mu p_{\mathrm{c}} \ , \tag{6.1}$$

where p_{c} denotes the local normal pressure, μ is the friction coefficient between the surfaces in contact, and τ_{c} is the critical value of q_{c} for which Coulomb's law is fulfilled (Fig. 6.1). For the sake of simplicity, the strain rate at the indented surface is taken to be sufficiently small as to ensure that a static friction coefficient rules the interaction between the solids. The finite element implementation of the contact model was performed within a finite-sliding formulation, where any arbitrary sliding and rotation between the surfaces can occur. In addition, the introduction of unsymmetric terms in the system of equations was accounted for in the simulations [1].

The finite element computations were performed for solids exhibiting all possible combinations of $E = 70$ and 200 GPa, with the values of σ_{ys} and n described in Section 3.1. The simulations were performed under $\mu = 0.1$ and 0.2 for each of the above solids. As indicated in Section 6.1.1, values of μ ranging from 0.1 to 0.2 are pertinent to indentation experiments carried out in well-polished metallic materials. Poisson's ratio, ν, was set constant at 0.3. In total, 64 simulations were conducted to account for the above combinations of mechanical properties and values of the friction coefficient.

6.2 Framework to the analysis of frictional effects

Theoretical aspects along with the results from the finite element simulations are considered in this section with the aim of developing a general framework to elucidate the influence of friction on sharp indentation.

6.2.1 Theoretical background

The influence of friction on contact stresses can be analyzed invoking load equilibrium at the indenter's face ($\sum \mathrm{d}F_z = 0$). First, we start by writing

$$P = \int_0^a p \ 2\pi r \ \mathrm{d}r \ , \tag{6.2}$$

which relates the overall pressure distribution $p(r)$ to the applied load P. Directing attention to Fig. 6.1, distributions of contact pressure $p_{\mathrm{c}}(r)$ and shear stress $q_{\mathrm{c}}(r)$ at the cone's face shall follow

$$\mathrm{d}P = p_{\mathrm{c}}\ \mathrm{d}A\ \sin\theta + q_{\mathrm{c}}\ \mathrm{d}A\ \cos\theta\ , \tag{6.3}$$

where

$$\mathrm{d}A = 2\pi r\ \mathrm{d}r/\sin\theta\ . \tag{6.4}$$

Eqs. (6.3) and (6.4) give

$$\mathrm{d}P = p_{\mathrm{c}}\ 2\pi r\ \mathrm{d}r + q_{\mathrm{c}}\ \cot\theta\ 2\pi r\ \mathrm{d}r\ . \tag{6.5}$$

Integrating Eq. (6.5) over the contact area and noting that the mean contact pressure at the cone, $\bar{p}_{\mathrm{c}}$, is given by

$$\bar{p}_{\mathrm{c}} = \frac{1}{\pi a^2}\int_0^a p_{\mathrm{c}} 2\pi r\ \mathrm{d}r\ , \tag{6.6}$$

it is found that

$$P = \pi a^2 \bar{p}_{\mathrm{c}} + \int_0^a q_{\mathrm{c}}\cot\theta\ 2\pi r\ \mathrm{d}r\ . \tag{6.7}$$

In addition, Eqs. (6.2) and (6.5) yield

$$p = p_{\mathrm{c}} + q_{\mathrm{c}}\cot\theta\ . \tag{6.8}$$

Note that the mean value of p is used to define hardness so that

$$H \equiv \frac{1}{\pi a^2}\int_0^a p\ 2\pi r\ \mathrm{d}r\ . \tag{6.9}$$

We now seek to find a relationship between hardness under frictional constraints, H, and hardness for frictionless conditions, $H_\circ$. For this purpose, Eq. (6.7) can be rearranged as

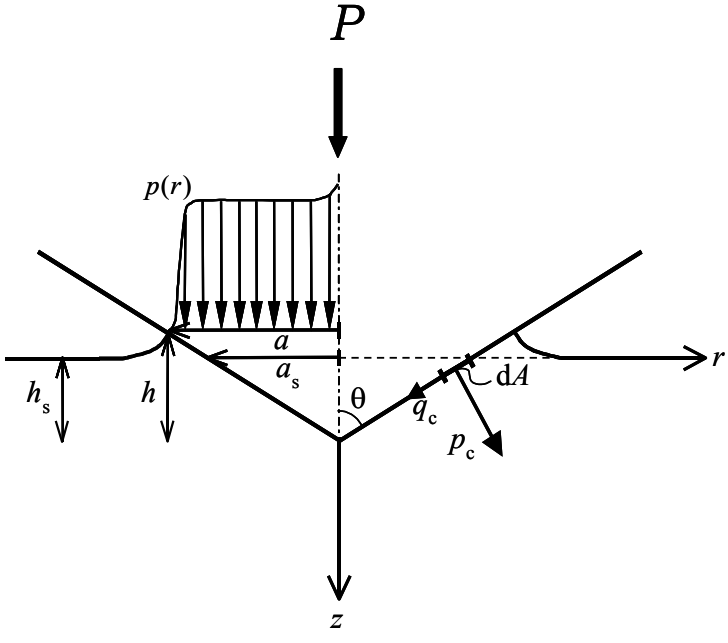

Figure 6.1: Contact variables used in the analysis of frictional effects.

$$P = \bar{p}_{\mathrm{c}} \pi a^2 \left(1 + \cot\theta \frac{1}{a^2} \int_0^a \frac{q_{\mathrm{c}}}{\bar{p}_{\mathrm{c}}} 2r\mathrm{d}r \right) \ . \tag{6.10}$$

Writing the integral on the right hand side of Eq. (6.10) as two integrals over regions where Coulomb's shear stress bound (CL) is reached and non-critical ones (NC) where the local $q_{\mathrm{c}} < \ \mu p_{\mathrm{c}}$, it follows that

$$H = \frac{P}{\pi a^2} = \bar{p}_{\mathrm{c}} \left(1 + \cot\theta \frac{1}{a^2} \left[\int_{\mathrm{NC}} \frac{q_{\mathrm{c}}}{\bar{p}_{\mathrm{c}}} 2r\mathrm{d}r + \int_{\mathrm{CL}} \frac{\mu p_{\mathrm{c}}}{\bar{p}_{\mathrm{c}}} 2r\mathrm{d}r \right] \right) \ . \tag{6.11}$$

Equation (6.11) is then rewritten as

$$H = \frac{P}{\pi a^2} = \bar{p}_{\mathrm{c}} \left(1 + \hat{\mu} \cot\theta \ \right) \ , \tag{6.12}$$

where

$$\hat{\mu} = \frac{1}{a^2} \left[\int_{\mathrm{NC}} \frac{q_{\mathrm{c}}}{\bar{p}_{\mathrm{c}}} 2r\mathrm{d}r + \int_{\mathrm{CL}} \frac{\mu p_{\mathrm{c}}}{\bar{p}_{\mathrm{c}}} 2r\mathrm{d}r \right] \ . \tag{6.13}$$

It is noted that the integration interval NC vanishes in the case where Coulomb's law applies throughout the whole contact area, thus $\int_{\mathrm{NC}} = 0$ and $\hat{\mu} = \mu$.

To relate H to $H_\circ$, we aim to find variable β so that the mean contact pressure at the cone's face, $\bar{p}_{\mathrm{c}}$, can be obtained through the mean contact pressure at the cone's face for $\mu = 0$, $\bar{p}_\circ$. Thus, we define

$$\bar{p}_{\mathrm{c}} = \beta \bar{p}_\circ \ . \tag{6.14}$$

Obviously, β has to be evaluated for the specific contact conditions at hand. Note that Eq. (6.8) implies $p_\circ = p_{\mathrm{c}_\circ}$, so that $H_\circ = \bar{p}_\circ$ (Eq. (6.9)) and

$$\bar{p}_{\mathrm{c}} = \beta H_\circ \ . \tag{6.15}$$

Hence, Eq. (6.12) becomes

$$H = \beta H_\circ \left(1 + \hat{\mu} \cot\theta \ \right) \ . \tag{6.16}$$

It is emphasized that frictional contacts induce shear stresses q_c so that $\hat{\mu} \neq 0$ and $\bar{p}_c \neq H$ (Eq.(6.12)). Then, from Eqs. (6.7) and (6.14), and by taking $H_\circ = P_\circ/A_\circ = P_\circ/\pi a_\circ^2$, it follows that

$$\beta = \frac{\pi a_\circ^2}{\pi a^2}\left(P - \int_0^a q_c 2\pi \cot\theta \; r dr\right)\frac{1}{P_\circ} \; . \tag{6.17}$$

Thus,

$$\beta = \frac{\pi a_\circ^2}{\pi a^2}\kappa \;\; ; \;\; \kappa = \left(P - \int_0^a q_c 2\pi \cot\theta \; r dr\right)\frac{1}{P_\circ} \; . \tag{6.18}$$

For indentations made under friction and frictionless conditions where identical penetration depth h_s is imposed, Eq. (1.4) yields

$$\beta = \frac{\alpha_\circ}{\alpha}\kappa \tag{6.19}$$

where for consistency with the current nomenclature, subscript $\circ$ denotes the absence of friction. Substituting Eq. (6.19) into Eq. (6.16), one finally obtains

$$H = \frac{\alpha_\circ}{\alpha}\kappa \; H_\circ \left(1 + \hat{\mu}\cot\theta \; \right) \; . \tag{6.20}$$

6.2.2 Simulations of frictional effects on hardness

A fundamental understanding of the role of friction in the contact response of strain hardening solids can be gained by comparing the distributions of contact pressure $p(r)$ for frictional contacts with those for frictionless conditions. First, the influence of elasto-plastic properties on pressure distributions is summarized as follows. As expected, the finite element simulations indicate that as σ_{ys}, n and E increase, $p(r)$ shifts gradually to larger stresses. It is also found that $p(r)$ is more sensitive to changes in σ_{ys} and n than to changes in E. Contact pressure distributions scale with E so that their overall *shape* remain constant. Solids with small values of σ_{ys} and n are found to exhibit the largest decay of p from the maximum value at $r = 0$ to that close to the contact boundary

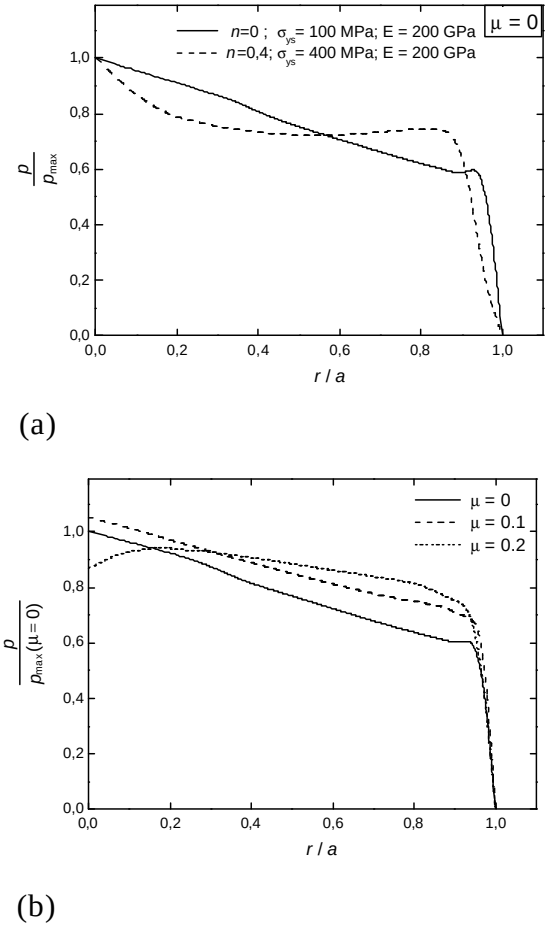

Figure 6.2: (a) Normalized pressure distributions $p/p_{\max}$ in terms of r/a for frictionless contacts. Note that $p/p_{\max}$ flattens as $\sigma_{\rm ys}$ and n increase. (b) Influence of friction coefficient μ on contact pressure distributions $p/p_{\max}$ for a solid with $\sigma_{\rm ys} = 100$ MPa, $n = 0$ and $E = 70$ GPa. The value of $p_{\max}$ used in the figure corresponds to that for $\mu = 0$. Note that by raising μ, the mean value of $p/p_{\max}$ increases while the whole distribution of $p/p_{\max}$ flattens.

($r \rightarrow a$), see Fig 6.2(a). Also, pressure distributions flatten with increasing $\sigma_{\rm ys}$ and n, Fig. 6.2(a), as well as by raising the friction coefficient μ, Fig. 6.2(b).

For frictionless contacts, the combined influence of elasto-plastic properties on $p(r)$ may be assessed through Tabor's hardness equation (note that hardness is given by the mean value of $p(r)$ as in Eq. (1.9)). Following Tabor's equation for the fully plastic regime, hardness is proportional to the uniaxial stress $\sigma_{\rm r}$ at a total (elastic plus plastic) uniaxial strain of 0.1 (see §4). Therefore,

$$H_\circ = C_\circ \sigma_{\rm r} \tag{6.21}$$

where $C_\circ = 2.7$ (subscript $\circ$ is used herein to denote frictionless conditions as in the previous section), and $\sigma_{\rm r} = {\sigma_{\rm ys}}^{1-n}(0.1E)^n$ according to the power-law relation in Eq. (A.21).

In the following, the finite element simulations are evaluated in the context of the theory presented in Section 6.2. Thus, it is our aim to find simple closed-form solutions for the relationship between H and $H_\circ$. First, it is important to note that solids undergoing piling-up effects also exhibit a large tendency to slip against the indenter's face which is opposed by friction. In such simulations, the critical shear stress according to Coulomb's relation is reached in the majority of the elements that are brought into contact. Good correspondence is thus found between the actual distribution of shear stresses $q_{\rm c}$ and the critical value of $\mu p_{\rm c}$, Fig. 6.3(a). This figure also shows that it is precisely the stresses at the innermost and outermost regions of the contact surface that may defy Coulomb's bound. However, notice that considerable slipping occurs in such regions which is required to accommodate the plastic deformations underneath the indenter. In solids where $\sqrt{\alpha} > 1.12$ and $\mu = 0.1$, more than 75% of the imprint lies within the Coulomb's dominated (CL) region. It is also found that $\hat{\mu}$ varies from 0.097 to 0.094 as κ ranges from 0.98 to 1.03. Equation (6.20) thus yields

$$H \approx \frac{\alpha_\circ}{\alpha}\, H_\circ(1 + \mu \cot\theta)\ . \tag{6.22}$$

In the above simulations for $\sqrt{\alpha} > 1.12$, the difference between H and $H_\circ$ is maximum as it lies in the range of $\sim 10\%$–15%. The accuracy of Eq. (6.22) when $\mu = 0.1$ is better than 1.5%.

When $\sqrt{\alpha} < 1.12$, that is, in solids exhibiting either moderate pileup or sinking-in effects, the local contact shear stresses become much smaller than the critical stress prescribed by Coulomb's relation (i.e., $q_c < \mu p_c$), see Fig. 6.3(b). In addition, the difference between q_c and μp_c increases as μ is raised from 0.1 to 0.2, indicating a larger tendency for the suppression of slip for large values of μ. Interestingly, it is found that $\kappa\ (1 + \hat{\mu}\ \cot\theta)$ varies from 0.99 to 1.01 for all values of μ. Thus, Eq. (6.20) reduces to

$$H \approx \frac{\alpha_\circ}{\alpha} H_\circ\ . \tag{6.23}$$

The validity of Eq. (6.23) when $\sqrt{\alpha} < 1.12$ is also sustained on the pressure distributions $p(r)$ which are found to be almost identical to those for frictionless simulations. Therefore, Eq. (6.23) suggests that to estimate H, it suffices to correct $H_\circ$ to account for the influence of friction on the size of the contact area (i.e., multiplying $H_\circ$ by $(\pi a_\circ^2/\pi a^2)$, see Eqs. (6.18) and (6.19)). Although the difference between H and $H_\circ$ when $\sqrt{\alpha} < 1.12$ is quite small as it lies in the range of 2%–6%, Eq. (6.23) is rather accurate as it allows to predict hardness H within a 1% error. It remains to be mentioned that in cases where $\sqrt{\alpha} > 1.12$ and $\mu = 0.2$, Eq. (6.23) is preferred over Eq. (6.22) because the material within the Coulomb's dominated region is less than 30% of that brought into contact. The error associated with the use of Eq. (6.23) is then smaller than 2.5% in contrast to the maximum value of $\sim 4.5\%$ obtained by using Eq. (6.22).

In view of the above findings, one may consider using Eqs. (6.22) and (6.23) to establish the influence of friction in Tabor's relation (Eq. (6.21)). Hence, for solids deforming within Tabor's fully plastic regime, we write

$$H = C(\mu)\ \sigma_r \tag{6.24}$$

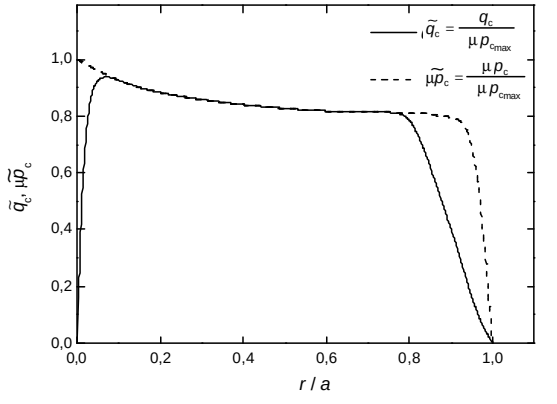

(a)

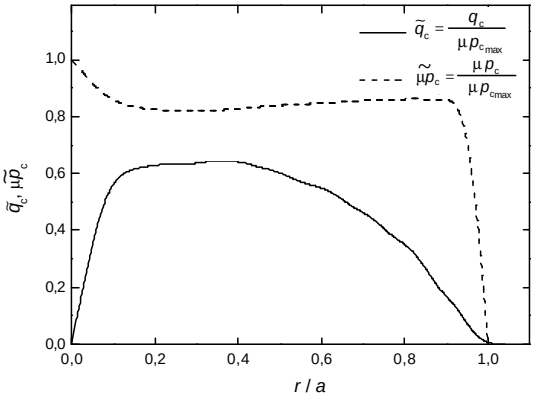

(b)

Figure 6.3: Distributions of normalized shear stress, $\tilde{q}_c$, and normalized critical shear stress according to Coulombs relation, $\tilde{\mu p}$. Coulombs law dominates within CL regions ($\tilde{q}_c = \tilde{\mu p}_c$) whereas the critical shear stress is not reached within the NC regions. The results are for solids exhibiting (a) extensive piling-up effects (σ_{ys} = 100 MPa, n = 0.1 and E = 70 GPa, where μ = 0.1 and $\sqrt{\alpha}$ = 1.14); and (b) sinking-in (σ_{ys} = 400 MPa, n = 0.2 and E = 70 GPa, where μ = 0.2 and $\sqrt{\alpha}$ = 0.97). The solid in Fig. 6.3(a) fulfills Eq.(6.22) while that in Fig. 6.3(b) fulfills Eq.(6.23).

where

$$C(\mu) = \begin{cases} 2.7\ (\alpha_\circ/\alpha)\ (1 + \mu\cot\theta), & \text{if } \sqrt{\alpha} > 1.12 \text{ and } \mu \leq 0.1; \\ 2.7\ (\alpha_\circ/\alpha), & \text{otherwise.} \end{cases}$$

It is emphasized that these equations are regarded to apply to pyramidal indentation to some useful extent because current simulations for $\theta = 70.3°$ yield hardness values that are in agreement with experimental measurements with Vickers indenters (see Section 3.3). Note that the influence of the half-apical angle θ is not captured thoroughly in these equations. Thus, care has to be exercised when applying Eq. (6.24) to conical indenters other than those with $\theta = 70.3°$ because the value of 2.7 for constant $C_\circ$ and the limiting value of 1.12 for $\sqrt{\alpha}$ are anticipated to depend on θ.

6.2.3 Plastic flow features and surface deformation effects

Figure 6.4 shows the results from the finite element simulations on the value of $\alpha_\circ/\alpha$ for all combinations of μ, E, n and σ_{ys} under consideration. Hence, the absolute value of α for a given μ and elasto-plastic properties can be readily obtained using Fig. 6.4 in conjunction with the correlation given in Section 5.3 between $\alpha_\circ$ and the elasto-plastic properties (Eq. (5.10)). Since the attainment of an elastic-plastic transition leads to an abrupt decrease in $\alpha_\circ/\alpha$, the relationship between $\alpha_\circ/\alpha$ and n is displayed in separate figures (Figs. 6.4(a), (b) and (c)). In doing so, we prevent the curves of $\alpha_\circ/\alpha$ – n for the different σ_{ys} and E from crossing each other.

The results in Fig. 6.4 show that $\alpha_\circ/\alpha$ is always > 1 in good agreement with physical intuition. In this regard, one can visualize the indenter as a rigid body displacing the material sideways. Frictional effects shall reduce contact radius a as shear stresses q_{c} build-in at the contact surface. This reduces the outward flow of material so that $a_\circ > a$. Therefore, the constraint imposed by q_{c} brings about a tendency to sink-in which necessary leads to $\alpha_\circ/\alpha > 1$. The plastic flow patterns from the simulations show evidence of such suppression of radial flow as the shear distortion of the elements at the interface is smaller as the value of μ increases, see Fig. 6.5. Consequently, for any given set of mechanical properties, $\alpha_\circ/\alpha$ increases as μ is raised from 0.1 to 0.2 (Fig. 6.4).

(a)

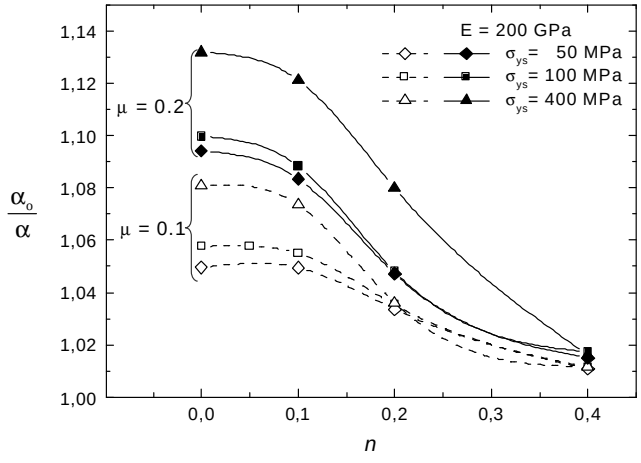
E = 200 GPa
σys= 50 MPa
σys= 100 MPa
σys= 400 MPa
μ = 0.2
μ = 0.1
αo/α
n
1,14
1,12
1,10
1,08
1,06
1,04
1,02
1,00
0,0
0,1
0,2
0,3
0,4

(b)

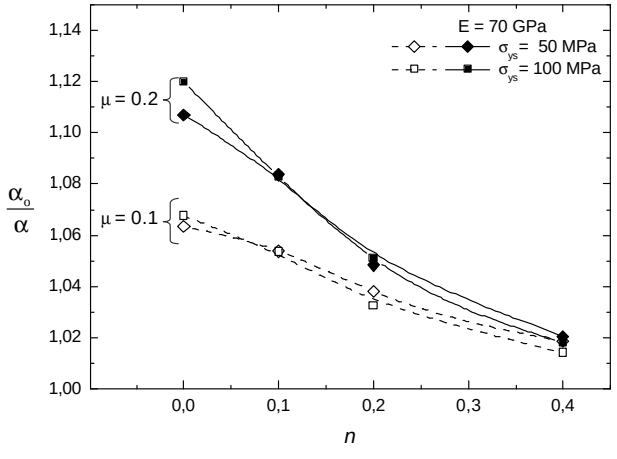
E = 70 GPa
σys= 50 MPa
σys= 100 MPa
μ = 0.2
μ = 0.1
αo/α
n
1,14
1,12
1,10
1,08
1,06
1,04
1,02
1,00
0,0
0,1
0,2
0,3
0,4

(c)

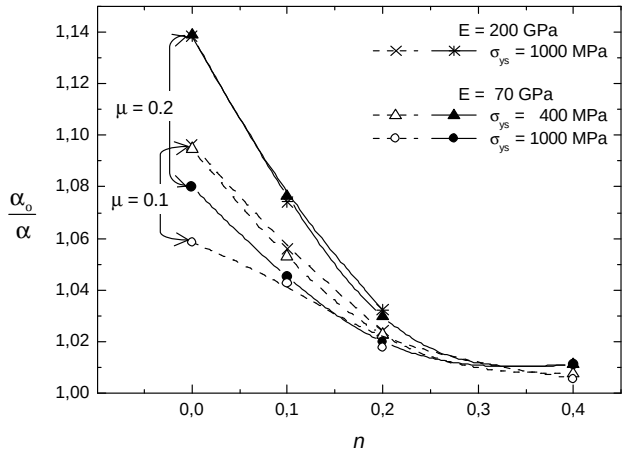

Figure 6.4: Relationship between $\alpha_\circ/\alpha$ and strain hardening coefficient n. The simulations are for $\mu = 0.1$ and 0.2 with (a) $E = 200$ GPa, (b) $E = 70$ GPa, and (c) either $E = 70$ GPa or 200 GPa with large values of $\sigma_{\rm ys}$.

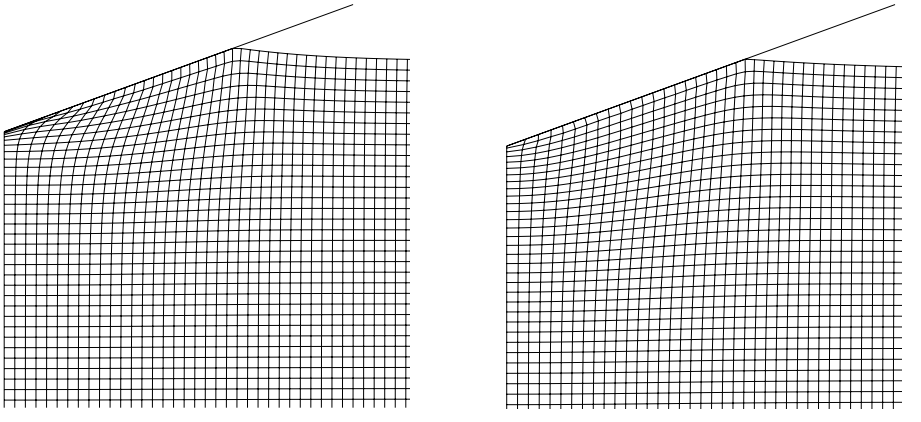

Figure 6.5: Frictional effects on plastic flow (a) $\mu = 0$, and (b) $\mu = 0.2$. Note that friction opposes slip of the elements at the indenter's face, which leads to a decrease in the amount of pileup. The results are for a solid with $\sigma_{\rm ys} = 100$ MPa, $n = 0.1$, and $E = 200$ GPa.

Overall, the simulations show that the influence of friction on surface deformation is larger in solids exhibiting pileup and, specially, when $\sqrt{\alpha} > 1.12$. This is due to the fact that pileup develops as a result of large outward flow at the interface, which is significantly restrained when sinking-in prevails. Therefore, frictional constraints have little influence in the simulations where sinking-in already occurs in the absence of friction. Indeed, for large sinking-in effects, joint motion between indenter and material occur along the z-axis irrespective of the value of μ. Such joint motion is favored by the tendency of the material to adhere to the indenter. It is also noticed that because of the radial component of the plastic flow when piling-up occurs, the existence of relative motion between indenter and material in the CL and NC regions is promoted.

Figure 6.4 shows that $\alpha_\circ/\alpha$ departs from unity as n decreases. This finding is consistent with the fact that piling-up is favored in solids with low values of n. As indicated above, the contact response under such conditions shall be largely affected by the development of shear stresses which tend to preclude radial flow. On the other hand, the simulations for $\mu = 0$ indicate that the amount of radial flow is already restricted when sinking-in prevails (this being the case for large values of n). Thus, it follows that an increase of μ shall not affect much in the development of plastic flow for large values of n. This is demonstrated in Fig. 6.4, whereby $\alpha_\circ/\alpha \rightarrow 1$ as $n \rightarrow 0.4$ irrespective of μ. Fig. 6.4 also shows that, for a fixed μ, the development of pileup is more sensitive to n than to σ_{ys}. In this sense, note that while $\alpha_\circ/\alpha$ may change in 0.12 as n increases from 0 to 0.4, a variation in σ_{ys} from 50 to 1000 MPa only changes $\alpha_\circ/\alpha$ by 0.04.

Finally, the simulations show that for small values of the strain hardening coefficient and yield strength, the plastic zone increases its size in the r-axis and z-axis as μ is raised gradually from 0 to 0.2, see Fig. 6.6. The maximum increase in the size of the plastic zone is about 20% in both axis. However, for large values of n and σ_{ys}, an increase in μ does not result in further growth of the plastic zone. The above-mentioned results are coincidental with the early analyses of a distortion of a square grid underneath a wedge indenter for adhesive and frictionless contacts in perfectly plastic solids ($n = 0$) [42; 46]. These analyses suggest that as friction is increased and the amount of piling-up becomes

smaller, the volume of material that originally displaced sideways shall be accommodated over a larger region underneath the indenter. This phenomenon increases the size of the plastic zone in solids exhibiting pileup. For the case of solids with large values of n and σ_{ys} where sinking-in is favored, radial flow is already limited under frictionless conditions to a point where an increase in μ does not bring significant changes to the plastic zone size.

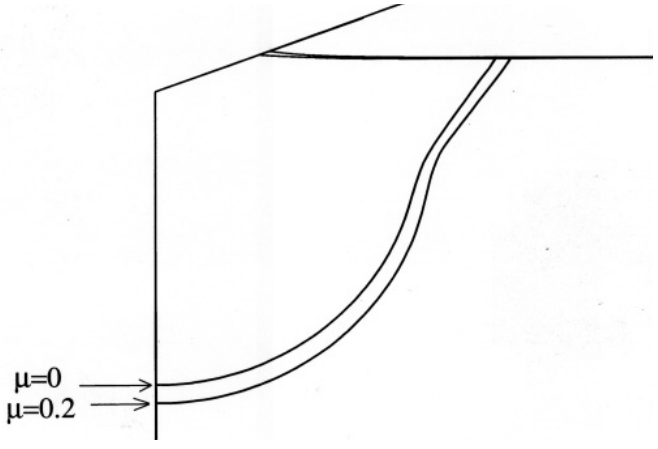

Figure 6.6: Increase in the plastic zone size as μ is raised from 0 to 0.2. The results are for $\sigma_{\mathrm{ys}} = 100$ MPa, $n = 0.1$, and $E = 200$ GPa.

6.3 Implications to indentation experiments

The present results are relevant to mechanical property extractions from instrumented indentation experiments when the friction coefficient μ is known *a priori*. In this regard, it is found that friction affects mostly surface deformation and hardness values while smaller changes occur in constant K from Kick's law, see Section 6.1.1. Kick's law ($P = K{h_{\mathrm{s}}}^2$; $K = f\alpha H$, Eq. (1.7)) thus indicates that the increase in hardness H induced by frictional effects is compensated by a decrease in the value of α so that the maximum increase in K due to friction is 3 %. As K describes the P–h_{s} curves, analysis

of instrumented indentation experiments requires consideration of surface deformation to improve accuracy in inferred mechanical properties. The purpose of this section is, therefore, to devise a methodology that considers surface deformation to evaluate the influence of the friction coefficient on the plastic properties $\sigma_{\rm ys}$ and n extracted from the P–$h_{\rm s}$ curves. The key issue in the present methodology is to obtain the equivalent *frictionless* contact parameters $H_\circ$ and $\alpha_\circ$ from the actual experimental data, where friction between the indenter and material occurs. Then, with such $H_\circ$ and $\alpha_\circ$ the procedure outlined in §5 is applied to obtain the yield strength and hardening coefficient which truly correspond to the indented material. The methodology is as follows (Fig. 6.7):

(i) Evaluate Young's modulus E with conventional nano-indentation procedures where the unloading segment of the P–$h_{\rm s}$ curves is fitted to Sneddon's relation (Eq. (1.5)). Measure hardness H considering bulging and pincushion effects at the sides of the imprint in the calculation of contact area A. Obtain the mean value of α around the indent as described in Section 5.4.

(ii) In the first iteration, assume $H_\circ = H$ and $\alpha_\circ = \alpha$.

(iii) Use the the general hardness equation derived in Section 5.2 (Eq. (5.6)) to estimate $\sigma_{\rm r_\circ}$.

(iv) Apply the procedure outlined in Section 5.4 to find $n_\circ$ and $\sigma_{\rm ys_\circ}$ using the values of $\alpha_\circ$, $\sigma_{\rm r_\circ}$ and E obtained in (i) and (iii).

(v) With Fig. 6.4, estimate $\alpha_\circ/\alpha$ for the friction coefficient μ of the experiment using the above values of $n_\circ$, $\sigma_{\rm ys_\circ}$ and E. Multiply such $\alpha_\circ/\alpha$ by the value of α obtained in (i) to calculate a new $\alpha_\circ$.

(vi) Compute $H_\circ{}'$ with the measured μ and the value of $\alpha_\circ/\alpha$ in (v). Use Eq. (6.22) if $\sqrt{\alpha} > 1.12$ and $\mu \le 0.1$; or Eq. (6.23) either if $\sqrt{\alpha} < 1.12$ for any arbitrary μ, or if $\sqrt{\alpha} > 1.12$ and $\mu = 0.2$. For intermediate values of μ, interpolate with the above results of $H_\circ{}'$ for $\mu = 0.1$ and 0.2.

(vii) End the procedure if $H_\circ = H_\circ{}'$. Otherwise, take $H_\circ = H_\circ{}'$ and apply steps (iii)–(vii). (Note that the current $\alpha_\circ$ obtained in (v) has to be used in (iv) in each subsequent iteration). The final $\sigma_{\mathrm{ys}_\circ}$ and $n_\circ$ correspond to the actual yield strength and strain hardening coefficient of the indented material. Less than 4 iterations are usually needed to obtain these properties within good accuracy.

The above methodology is relevant to the analysis of indentation experiments because if frictional effects were disregarded, the overall contact response in terms of hardness and surface deformation would coincide with that of a solid whose n or, alternatively, σ_{ys} are larger to the utmost of $\sim 50\%$. The magnitude of such overestimation depends upon $\sqrt{\alpha}$, n, σ_{ys} and μ.

6.4 Summary

Present chapter provided a rationale to assess the role of friction on sharp indentation experiments performed in strain hardening solids. Finite element simulations were conducted to analyze the effect of friction coefficient μ on the main physical quantities and features of indentation testing (such as hardness and the attainment of surface deformation effects around the contact boundary), as well as instrumented indentation P–h_{s} curves.

The finite element simulations of pressure distributions along with the theoretical treatment of frictional contacts provided in Section 6.2, enable derivation of two equations relating the actual hardness H with the equivalent hardness in the absence of friction $H_\circ$. It is found that α is a useful parameter in establishing the range of applicability of these equations. In this sense, it is shown that when considerable piling-up occurs ($\sqrt{\alpha} > 1.12$), Eq. (6.22) provides a good relation between H and $H_\circ$, whereas for moderate pileup or sinking-in effects H and $H_\circ$ are better correlated through Eq. (6.23).

Emphasis is placed in providing a detailed evaluation of the influence of the friction coefficient μ on α in solids exhibiting a vast combination of mechanical properties. Since solids undergoing extensive pileup require slipping of material to take place against the

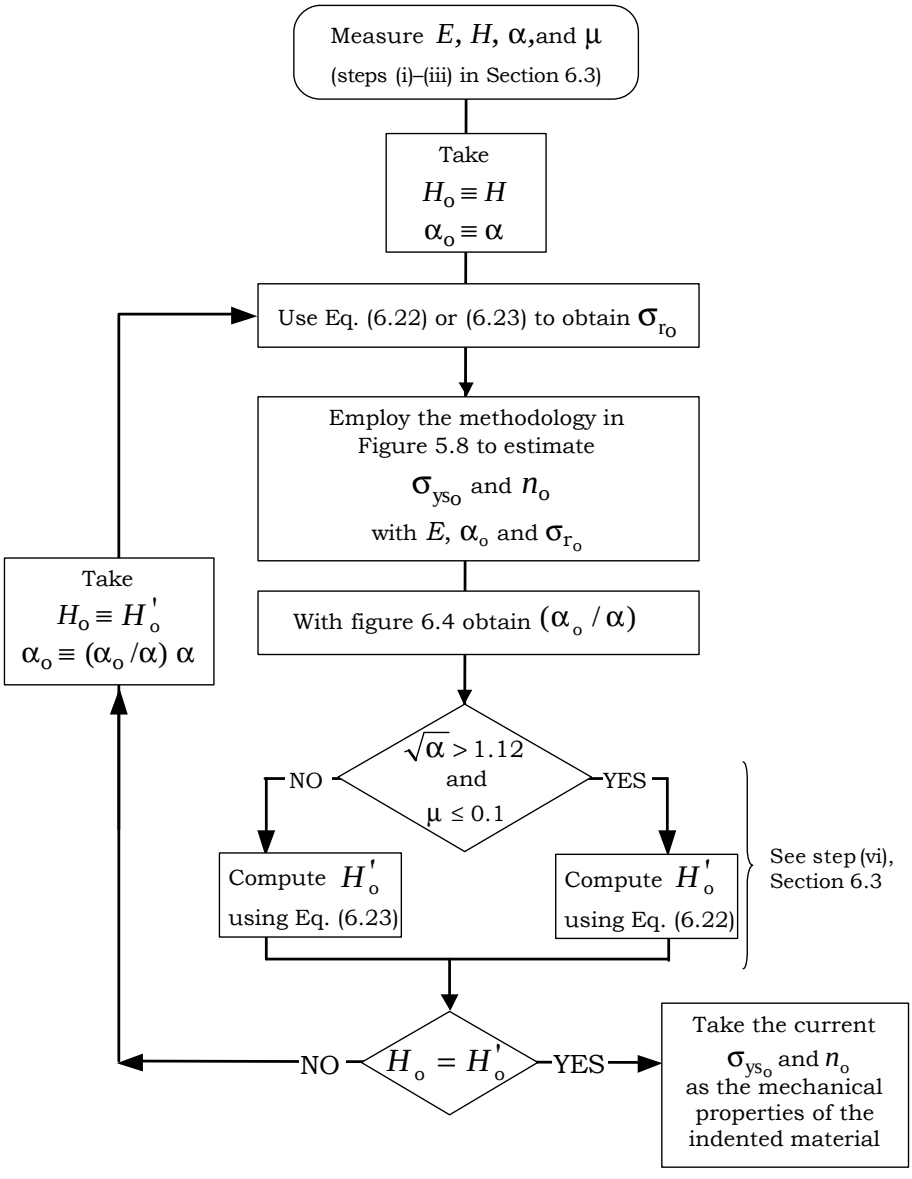

Figure 6.7: Algorithm to evaluate frictional effects on mechanical properties extracted through indentation experiments.

indenter, friction has the largest influence on their contact response as it opposes such slip. In these solids, it is found that Coulomb's relation gives the distribution of shear stresses acting at the interface, simplifying the theoretical treatment of frictional effects on hardness. On the other hand, moderate pileup or sinking-in effects ($\sqrt{\alpha} < 1.12$) are indicative of contact responses wherein the radial flow of material at the indenter's face is restrained even in the absence of friction. Consequently, in such solids, the introduction of friction into the analysis does not bring much of a change in plastic flow patterns and pressure distributions. It goes without saying that as the critical shear stress is not reached in the latter cases, Coulomb's law does not provide an accurate description of contact interactions.

Finally, a methodology is proposed to account for the influence of the friction coefficient in mechanical properties evaluated through instrumented indentation experiments. The methodology utilizes present findings of the role of friction on the development of surface deformation, as well as the procedure devised in the §5 to infer yield strength $\sigma_{\rm ys}$ and hardening coefficient n from indentation experiments. The actual friction coefficient has to be taken into account in the assessment of mechanical properties specially in such solids exhibiting piling-up effects, where the largest influence of friction upon the contact response is encountered. In such cases, the values of $\sigma_{\rm ys}$ and n extracted from the P–$h_{\rm s}$ curves neglecting friction may be up to 50% larger than the actual ones.

From an experimental standpoint, it may be recommended that rather than using a lubricating fluid to decrease friction in indentation experiments, one shall consider measuring the actual friction coefficient and correct the results according to the analysis presented herein. While the use of a lubricating fluid between the indenter and specimen may certainly decrease μ, its effective value in the presence of such fluid may be difficult to evaluate experimentally. In addition, large contact pressures in indentation testing may induce evacuation of the fluid from the contact area, thus preventing formation of a lubricating layer. It is finally noticed that indentation size effects, typically encountered in nano- and micro-indentation, may not be related to frictional effects [7; 37; 53; 54]. In this sense, note that within present analytical framework, hardness and surface defor-

mation remain constant irrespective of applied load range for a given friction coefficient. Surface roughness effects in nano-indentation may defy the continuum treatment presented herein when the contact area is comparable to the characteristic length-scale of the roughness profile at the indented surface. In addition to the current framework, where the indented surface is characterized through a continuous (macroscopic) value of μ, the effect of roughness on nano-indentation may be taken into account considering the change in the angle of incidence of the indenter as it is brought into contact with the asperities of the surface [12; 16].

Chapter 7

The plastic zone size in indentation experiments: the analogy with the expansion of a spherical cavity

A characteristic feature of indentation experiments is the development of a plastic zone, whose size increases during load application. Among other aspects, knowledge of the plastic zone size allows (i) extraction of the yield strength of a material; (ii) examination, within a continuum mechanics framework, of discrete deformation processes occurring at small loads; and (iii) assessment of possible influence of substrate effects on the contact response of thin films and small-volume structures; see [29; 35; 36; 45; 49; 53; 66; 68; 77; 79]. In addition, the shape of the plastic zone is indicative of the plastic flow features underneath the indenter. In this thesis we have shown that elasticity plays a fundamental role in indentation experiments when the plastic zone is confined underneath the indenter's tip. On the other hand, elastic strains play a secondary effect within the fully plastic contact regime, where the plastic zone spreads outwards from the indenter (see §4).

Mechanistic interpretations to indentation experiments have long been based on the analogy between indentation and the expansion of a spherical cavity [10; 28; 47]. This

analogy provides useful relationships between contact parameters, such as hardness and plastic zone size, and the elasto-plastic mechanical properties of the material. In particular, Johnson's model allows one to predict the plastic zone size c from

$$\left(\frac{c}{a_{\mathrm{s}}}\right)^{3} = \frac{E}{3\,\sigma_{\mathrm{ys}}\,\tan\theta} \tag{7.1}$$

where a_{s} is the radius of the imprint (which is equivalent to the radius of the spherical cavity), E is the Young's modulus, and σ_{ys} is the yield strength. Although this equation has been employed in the analysis of indentation experiments [29; 35; 36; 45; 47; 49; 53; 66; 77; 79], the underlying analogy between indentation parameters and those ruling the expansion of the cavity has not been thoroughly established. Furthermore, the above indentation model requires definition of a hydrostatic core to act as the spherical cavity [28; 47]. The rationale behind the conception of the core remains rather obscure, as it comprises both the rigid indenter and the surrounding material within a single concept. Also, the hydrostatic nature of the core is controversial in light of the large shear stresses and extensive plastic flow attained underneath the indenter.

An important limitation in Eq. (7.1) is that it ignores strain hardening effects, as it is derived for elastic–perfectly plastic solids. Formulations to incorporate strain hardening into the analysis of the expanding cavity were given by [9; 21; 28; 33; 56]. These investigations focused on the internal pressure existing at the cavity which, according to Johnson's model, is taken to be proportional to hardness. Although such analyses on strain-hardening solids succeeded in finding integral-form relations for the internal pressure as a function of the plastic zone size, attempts were not made to derive closed-form relations between the plastic zone and the mechanical properties of the solid. The main purpose of this chapter is to obtain closed-form solutions for these relations and to ensure their applicability to the analysis of indentation experiments.

This chapter is arranged in the following sections. First, the internal pressure for the expansion of the cavity in elastic–power-law plastic solids is solved in Section 7.1. Through extensive finite element simulations of spherical and conical indentation, the analogy between indentation experiments and the expansion of the cavity is examined

in Section 7.3. The finite element simulations allow us to elaborate on the concept of an equivalent spherical indenter, which replaces the cavity. Based upon these findings, parameters from indentation experiments are related to governing variables from expanding cavity formulations. These formulations are then reviewed in the context of indentation experiments in Section 7.4. Three-dimensional finite element simulations of pyramidal indentation are used in Section 7.5 to address the issue of how to extend the present framework to the analysis of Vickers and Berkovich indentation experiments, as well as to evaluate the influence of load removal upon the extension of the plastic zone.

7.1 Formulation of the expansion of a spherical cavity in an infinite medium

7.1.1 General framework

In this section, an overview is given on the existing framework for the analysis of the expansion of a spherical cavity in strain hardening solids [42; 56]. Figure 7.1 illustrates a cavity of instantaneous radius R_{i} which expands radially into an infinite space. Inflation of the cavity exerts hydrostatic pressure which modifies the stress-strain state of the surrounding medium.

After an initial elastic behavior of the solid, further inflation of the cavity leads to the onset of plastic deformation at a critical value of internal pressure p_{cav}. An elastic-plastic boundary of radius c is thus induced, where for $\rho > c$ the solid remains elastic. Owing to spherical symmetry, stresses and strains are expressed in terms of radial position ρ, Fig. 7.1. By virtue of spherical symmetry, the stress state is taken as the sum of a fully hydrostatic state (σ_θ, σ_θ, σ_θ) and compressive state ($\sigma_\rho - \sigma_\theta$, 0, 0) [42]. Hence, the von Mises yield condition implies [56],

$$\sigma_\theta - \sigma_\rho = Y(\epsilon) \ , \tag{7.2}$$

where $Y(\epsilon)$ is the uniaxial strain-hardening law of the solid, which is taken to obey a Ramberg-Osgood relation. Therefore, see Appendix A,

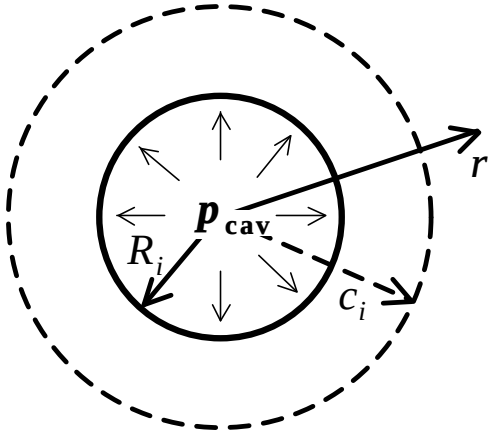

Figure 7.1: Expansion of a spherical cavity of instantaneous radius R_i and plastic zone c_i induced by hydrostatic pressure p_cav. ρ is the radial coordinate.

$$\sigma = \begin{cases} E\epsilon & \text{if } \epsilon \leq \epsilon_\mathrm{ys}, \\ \mathrm{Y}(\epsilon) = \sigma_\circ \epsilon^n & \text{otherwise}, \end{cases} \tag{7.3}$$

where ϵ is the *total* uniaxial strain ($\epsilon = \epsilon_\mathrm{el} + \epsilon_\mathrm{pl}$), E is the Young's modulus, and n is the power-law strain-hardening coefficient. As in the previous chapters, for continuity of the stress–strain relation at $\epsilon = \epsilon_\mathrm{ys}$ it follows that $\sigma_\circ = {\sigma_\mathrm{ys}}^{1-n} E^n$.

As the stresses are continuous across the elastic-plastic boundary, the internal pressure p_cav leading to plastic flow is [42; 56]

$$p_\mathrm{cav} = \frac{2}{3}\sigma_\mathrm{ys} + 2\int_R^c Y(\epsilon)\frac{\mathrm{d}\rho}{\rho} \ . \tag{7.4}$$

The following concerns description of cavity growth in terms of the plastic zone size and the mechanical properties of the solid. Treating the elastic-plastic boundary as elastic and compressible, the relative plastic zone size (c/R) is given by [42; 56]

$$\frac{dR}{dc} = \frac{3(1-\nu)Y(\epsilon)c^2}{ER^2} - \frac{2(1-2\nu)Y(\epsilon)R}{Ec} \ . \tag{7.5}$$

For simplicity in solving Eq. (7.5), plastic incompressibility is assumed for $\rho < c$ (i.e., Poisson's ratio, ν, $= 0.5$). This is a sensible approximation as ν has little influence in the value of c [21]. The second term in the right-hand side of Eq. (7.5) thus vanishes, leading to a separate-variable differential equation. Integration yields

$$R^3 - {R_\circ}^3 = \frac{3}{2E}\int_{c_\circ}^{c} 3\rho^2 Y(\epsilon)\mathrm{d}\rho \ , \tag{7.6}$$

where $R_\circ$ is the cavity radius corresponding to a plastic zone $c_\circ$. In contrast to Eq. (7.4), which describes an instantaneous state in the inflation of the cavity, Eq. (7.6) concerns the *evolution* of the cavity from initial conditions $R_\circ$ and $c_\circ$. Therefore, finding closed-form solutions for Eq. (7.6) requires prior knowledge of variables $R_\circ$ and $c_\circ$.

A particular case in the above analyses pertains to elastic–*perfectly* plastic solids ($n = 0$ and $Y(\epsilon) = \sigma_{\mathrm{ys}}$) [42]. Integration of Eq. (7.4) in such solids yields

$$p_{\mathrm{cav}} = \frac{2}{3}\sigma_{\mathrm{ys}}\left[1 + 3\ln\left(\frac{c}{R}\right)\right] \ . \tag{7.7}$$

Under these conditions, the well-known relation for the relative plastic zone size is obtained from Eq. (7.6):

$$\frac{c}{R} = \left(\frac{2E}{3\sigma_{\mathrm{ys}}}\right)^{\frac{1}{3}} \ , \tag{7.8}$$

where it is assumed that $R_\circ = c_\circ = 0$ [42]. Alternatively, considering that linear elasticity still applies at the elastic-plastic boundary, $\rho = c$, substitution of elastic solutions for σ_θ and σ_ρ into Eq. (7.2) yield the same relation as Eq. (7.8) [42; 56].

7.1.2 Fully plastic response

Integration of Eq. (7.4) is performed in this section neglecting the influence of elastic strains on the plastic zone size (i.e., $\epsilon = \epsilon_{\mathrm{pl}}$). The closed-form solution derived herein thus applies to the inflation of a cavity in solids whose local strains are plastically dominated. The applicability of this approximation to indentation experiments of solids exhibiting various degrees of elasto-plastic deformation is examined in Section 7.4.2.

Since the displacements are radial, plastic incompressibility allows one to find the following equation for radial deformation ϵ within the plastic zone (see [42; 56])

$$\epsilon = 2\ln\left(\frac{\rho}{\rho_\circ}\right) = \frac{2}{3}\ln\left(\frac{\rho^3}{\rho^3 - R^3}\right) \ . \tag{7.9}$$

Equation (7.9) prescribes the instantaneous deformation of a generic material-point at distance ρ with respect to its initial position $\rho_\circ$ (ρ and $\rho_\circ$ are within plastic zones c and $c_\circ$, respectively). In deriving Eq. (7.9), it is further assumed that $R_\circ = 0$.

Substitution of Eq. (7.9) into Eq. (7.3) leads to a relationship for yield strength Y in terms radial coordinate ρ. Then, from Eq. (7.4), it follows that

$$p_{\text{cav}} = \frac{2}{3}\sigma_{\text{ys}} + 2\int_R^c \sigma_\circ\left(\frac{2}{3}\ln\left(\frac{\rho^3}{\rho^3 - R^3}\right)\right)^n \frac{\mathrm{d}\rho}{\rho} \ . \tag{7.10}$$

Taking $t = \rho/R$, Eq. (7.10) transforms to

$$p_{\text{cav}} = \frac{2}{3}\sigma_{\text{ys}} + 2\int_1^{c/R} \sigma_\circ\left(\frac{2}{3}\ln\left(\frac{t^3}{t^3 - 1}\right)\right)^n \frac{\mathrm{d}t}{t} \ . \tag{7.11}$$

This equation provides a fundamental relationship between cavity pressure p_{cav}; mechanical properties σ_{ys}, $\sigma_\circ$ and n; and relative plastic zone size c/R. However, to our knowledge, the integral in Eq. (7.11) lacks of analytical solution. The approach adopted herein to solve Eq. (7.11) is thus to replace the integrand with a simple best-fit integrable function. It is remarked that although the integrand diverges for $t = 1$, the integral in Eq. (7.11) is necessarily finite as σ_{ys} and p_{cav} are bounded quantities.

Hence, we seek to find $f(t, n)$ so that

$$\left(\frac{2}{3}\ln\left(\frac{t^3}{t^3 - 1}\right)\right)^n \frac{1}{t} \ = \ f(t \geq x(n), n) \ \simeq \ A(n)\, t^{B(n)} \ , \tag{7.12}$$

where $x(n)$ is the value of t below which $f(t,\, n)$ starts to depart from the integrand. Functional analysis is then used to obtain constants A and B best-fitting Eq. (7.12) for discrete values of the strain hardening coefficient n. Representation of $f(t,\, n) = At^B$ readily confirms that for optimum values of A and B, this simple functional form adjusts

extremely well to the integrand (provided $t \geq x(n)$), Fig. 7.2. To solve the integral, we then impose

$$\int_1^{c/R} 2\sigma_\circ \left(\frac{2}{3} \ln\left(\frac{t^3}{t^3-1} \right) \right)^n \frac{\mathrm{d}t}{t} \;=\; 2\sigma_\circ N_\circ(n) \;+\; 2\sigma_\circ \int_{x(n)}^{c/R} f(t,n)\; \mathrm{d}t \;, \tag{7.13}$$

where $2\sigma_\circ N_\circ(n)$ estimates the diverging part of the integral from $t = 1$ to $t = x(n)$. The actual value of $N_\circ(n)$ is herein obtained through a numerical integration scheme.

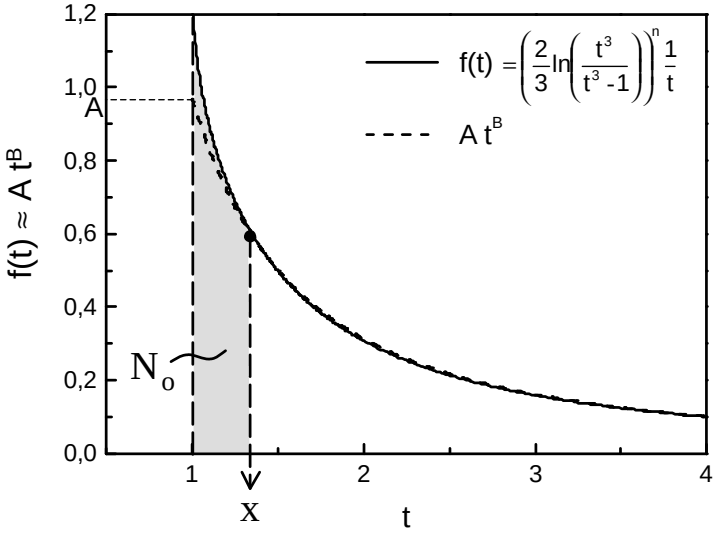

Figure 7.2: Functional analysis of the integrand in Eq.(7.12) for a value of $n = 0.2$. The solid line corresponds to the integrand, and the dashed line to the fitting function At^B.

Finally, substituting Eq. (7.13) into Eq. (7.11) yields

$$\frac{p_{\mathrm{cav}}}{\sigma_\circ} = \frac{2}{3}\frac{\sigma_{\mathrm{ys}}}{\sigma_\circ} + 2N_\circ(n) + 2M_\circ(n)\left[\left(\frac{c}{R} \right)^{P(n)} - x(n)^{P(n)} \right] \;; \tag{7.14}$$

$$M_\circ(n) = \frac{A(n)}{B(n)+1} \quad , \quad P(n) = B(n)+1 \;.$$

We now direct attention to the early work by Tabor, where hardness is normalized with respect to the representative uniaxial stress σ_{r} [73]. This is an important issue as the use of expanding cavity formulations in the analysis of indentation experiments relies on the equivalency between hardness H and pressure p_{cav}, see Section 7.3. In the spirit of Tabor's work, stress level σ_{r} is defined at a uniaxial material-independent representative deformation ϵ_{r} of 0.1, so that H/σ_{r} happens to be of about 2.7 in solids whose contact response is plastically dominated (see §4). Then, from the uniaxial stress-strain relation (Eq. (7.3)) it follows that

$$\sigma_{\mathrm{r}} = {\sigma_{\mathrm{ys}}}^{1-n}(0.1\ E)^n\ . \tag{7.15}$$

Thus, replacing variable $\sigma_\circ$ for σ_{r} in Eq. (7.14), yields

$$\frac{p_{\mathrm{cav}}}{\sigma_{\mathrm{r}}} = \frac{2}{3}\left(\frac{\epsilon_{\mathrm{ys}}}{\epsilon_{\mathrm{r}}}\right)^n + \Theta(n) + M(n)\left(\frac{c}{R}\right)^{P(n)}\ ; \tag{7.16}$$

$$\Theta(n) = N(n) - M(n)\ x(n)^{P(n)}\ ,\quad N(n) = \frac{2N_\circ(n)}{{\epsilon_{\mathrm{r}}}^n}\ ,\quad M(n) = \frac{2M_\circ(n)}{{\epsilon_{\mathrm{r}}}^n}\ .$$

Where, in accordance with Eqs. (7.12)–(7.14), it is found that

$$\Theta(n) = \ \ 2.5968 + \frac{0.5097}{n}\ , \tag{7.17}$$

$$M(n) = -2.2778 - \frac{0.5479}{n}\ , \tag{7.18}$$

$$P(n) = -3.0615\ n - 0.005\ . \tag{7.19}$$

7.1.3 Elasto-plastic response

In this section, we aim at extending the above analysis for fully-plastic solids to account for the influence of elastic strains within the plastic zone. An integral equation for $p_{\mathrm{cav}}/\sigma_\circ$ that explicitly incorporates the role of elastic strains is thus derived. As

described in Section 7.4.1, this analysis is relevant to indentation experiments in solids whose contact response is significantly affected by elasticity (that is to say, those deforming within the elasto-plastic contact regime, see §4).

Following Eq. (7.3), the uniaxial strain-hardening law of the solid is assumed to obey

$$Y(\epsilon) = \sigma_\circ(\epsilon_{\rm pl} + \epsilon_{\rm el})^n = \sigma_\circ\Big(\epsilon_{\rm pl} + \frac{\sigma}{E}\Big)^n \ . \tag{7.20}$$

Considering that elastic strains are smaller than plastic strains, we write

$$\Big(\epsilon_{\rm pl} + \frac{\sigma}{E}\Big)^n \simeq {\epsilon_{\rm pl}}^n \left(1 + n\frac{\sigma/E}{\epsilon_{\rm pl}}\right) \ . \tag{7.21}$$

So that, taking $\epsilon_{\rm pl} \simeq \epsilon$, it follows that

$$Y(\epsilon) \simeq \sigma_\circ \left(\epsilon^n + n\epsilon^{n-1}\frac{\sigma}{E}\right) = \sigma_\circ\epsilon^n + \frac{{\sigma_\circ}^2}{E} n\epsilon^{2n-1} \ . \tag{7.22}$$

The same analysis as in Section 7.1.1 is then performed using the approximative stress-strain relation in Eq. (7.22). After some rearrangements, we find

$$\frac{p_{\rm cav}}{\sigma_\circ} = \frac{2}{3}\frac{\sigma_{\rm ys}}{\sigma_\circ} + 2\int_1^{c/R} \left(\frac{2}{3}\ln\left(\frac{t^3}{t^3-1}\right)\right)^n \frac{{\rm d}t}{t} \ + \\ 2n\frac{\sigma_\circ}{E}\int_1^{c/R} \left(\frac{2}{3}\ln\left(\frac{t^3}{t^3-1}\right)\right)^{2n-1} \frac{{\rm d}t}{t} \ . \tag{7.23}$$

By virtue of the approximation made in Eq. (7.22), note that the right hand side of Eq. (7.23) is composed by three terms. A relevant feature in this formulation is that, comparing Eq. (7.23) with Eq. (7.11), one can readily see that the first two terms in Eq. (7.23) correspond to the fully plastic solution, so that the influence of elastic strains is necessarily captured through the third term. The second term dominates over the third term in metallic materials because $\sigma_\circ \ll E$ and $n < 0.6$. The validity of Eq. (7.23) is questionable in stiff solids where $n \ \to 1$, as one may not longer assume that $\epsilon_{\rm pl} \simeq \epsilon$.

7.2 Finite element simulations

Finite element simulations were performed for conical and spherical indentation experiments. Details of the finite element meshes and their density-region hierarchy are given in Section 3.1. Indenter's diameter was scaled to fulfill $a_s/R = 0.75$ at maximum depth. Complementary three-dimensional simulations were performed for the Vickers and the Berkovich pyramidal indenters as described in [20; 39], see Fig. 7.3. Frictionless contact conditions were assumed.

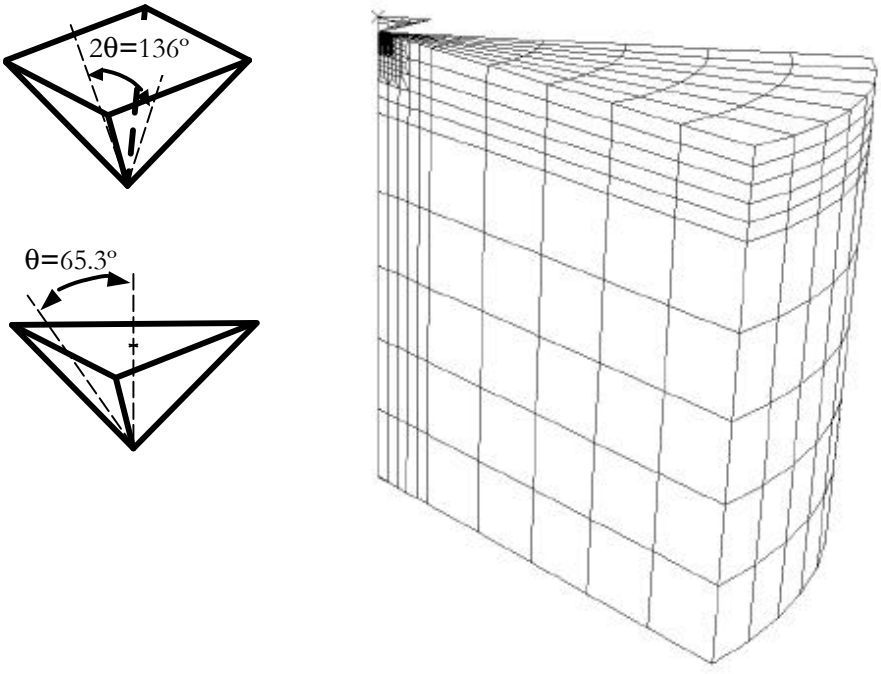

Figure 7.3: Finite element mesh used in the three-dimensional simulations of Vickers and Berkovich indentations. [From [20]].

The simulations of spherical indentation, Vickers indentation, and Berkovich indentation were performed for the solids listed in Table 7.1. These solids are representative of the wide range of mechanical properties used in the previous simulations of conical

indentation (§3).

indenter			E / σ_r	E (GPa)	σ_{ys} (MPa)	n
	V		4000	200	50	0
S			1400	70	50	0
		B	700	70	100	0
S		B	500	200	400	0
	V		275	110	400	0
S	V	B	70	70	1000	0
S	V	B	2197	200	50	0.1
	V	B	1177	200	100	0.1
S		B	854	70	50	0.1
		B	458	70	100	0.1
S	V	B	338	200	400	0.1
S		B	148	200	1000	0.1
S	V	B	58	70	1000	0.1
S			1207	200	50	0.2
	V	B	693	200	100	0.2
	V	B	521	70	50	0.2
S	V	B	229	200	400	0.2
S	V	B	47	70	1000	0.2
S	V	B	364	200	50	0.4
	V	B	240	200	100	0.4
S		B	194	70	50	0.4
S	V	B	105	200	400	0.4
S	V	B	36	70	1000	0.4

S = sphere, V = Vickers, B = Berkovich

Table 7.1: Mechanical properties of the solids used in the simulations of spherical and pyramidal indentation.

7.3 The analogy between indentation and the expansion of a cavity

The purpose of this section is to propose a sensible substitution of the parameters describing the plastic zone in sharp indentation experiments for those in expanding cavity formulations.

We first seek to establish an equivalent penetration depth in which the plastic zone induced by a spherical indenter (replacing the cavity) is similar to that existing around a conical tip. Note that the sought-after similarity exclusively concerns the plastic zone and not the stress fields or hardness values. Perhaps the main obstacle in finding such an equivalent penetration depth is that while the plastic zone in sharp indentation has a self-similar nature, the severity of the deformation field in spherical indentation increases as the ratio between contact radius a_s to indenter's radius R is increased. Thus, as indentation strain a_s/R increases, the contact response evolves from a Hertzian perfectly-elastic regime, to an elasto-plastic transition, to the fully plastic response examined by Tabor. In the absence of length scales, however, the active deformation regime in conical indentation remains constant throughout the entire penetration process by virtue of its self-similar character. Following the work by Johnson, a contact deformation map was devised in §4 to predict the active deformation regime in sharp indentation experiments of strain hardening solids. The results, which are pertinent to the present discussion, showed that the degree of elasto-plasticity increased in solids with a small E or with large values of σ_{ys} and n.

It is noteworthy that the angle of 136° existing between opposite faces of the Vickers pyramidal indenter was selected based upon a geometrical analogy with the spherical (Brinell) indentation test. In the spirit of this analogy, the equivalent sphere is taken to be tangent to the cone at imprint radius a_s (Fig. 7.4(a)). It thus follows that

$$\sin(90^\circ - \theta) = a_s/R \ , \tag{7.24}$$

so that when $\theta = 70.3^\circ$, $a_s/R = 0.342$. Nevertheless, inspection of the finite element

simulations reveals that the plastic zone size induced by the conical indenter is larger than that which is present around the spherical tip at $a_s/R = 0.342$ (Fig. 7.5). Overall, the evolution in plastic zone size exhibited in spherical indentation of solids with a large degree of elasto-plasticity is more pronounced than that found in those whose contact response is more plastically dominated (compare Figs. 7.5 (a) and (c)). The difference in plastic zone sizes between both tips thus increases as the contact response becomes more elasto-plastic. This indicates that, while solids indented within the fully plastic contact regime have similar plastic zones for conical and spherical indentation provided $a_s/R > 0.30$, this is not true in elasto-plastic materials where agreement in the plastic zone size is only encountered for larger values of a_s/R. Along these lines, circumspective analysis of the finite element simulations suggests that *irrespectively of the contact response*, relative plastic zone sizes measured at $a_s/R = 0.643$ are the same as those exhibited for conical indentation with $\theta = 70.3°$. As illustrated in Fig. 7.4(b), this interesting finding enables us to reformulate the aforementioned analogy of the equivalent penetration depth to ensure that the two indenters cross each other at the free surface (a_s) as well as at penetration depth h_s. Simple geometrical arguments thus yield

$$\frac{a_s}{R} = \frac{2\tan\theta}{1+\tan^2\theta} \ , \tag{7.25}$$

so that when $\theta = 70.3°$, $a_s/R = 0.643$. Cavity radius R in expanding cavity formulations is thus substituted by

$$R = \frac{a_s}{0.643} \ . \tag{7.26}$$

Attention is now given to cavity pressure p_{cav}. In the spirit of the analogy between the hydrostatic pressure inflating the cavity and hardness measurements in a sharp indentation experiments, we take

$$p_{cav} = H_L = \frac{H}{l} \ , \tag{7.27}$$

where H is the projected hardness, H_L is the Ludwick hardness computed with the curved surface or cavity area of the indentation, and l is a projection factor. For conical

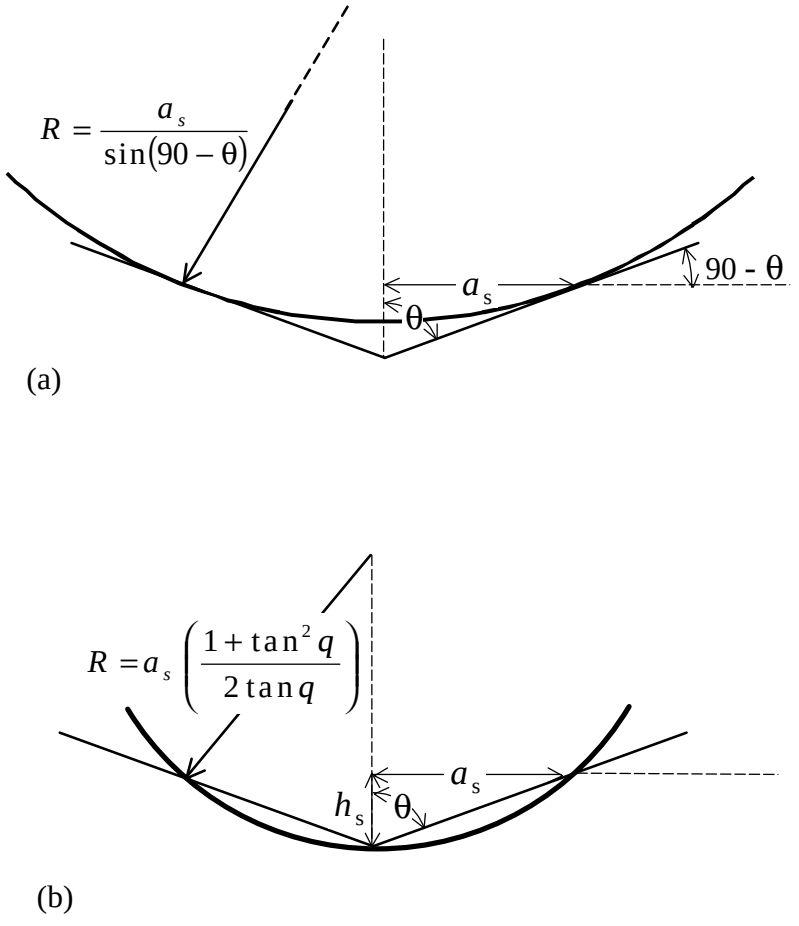

Figure 7.4: Definition of the equivalent spherical indenter. (a) The sphere is taken to be tangent to contact radius a_s. (b) Configuration where the equivalent sphere intersects contact radius a_s and penetration depth h_s.

(a)

	σ_e
1	1000
2	1231
3	1463
4	1694
5	1926
6	2157
7	2389
8	3314

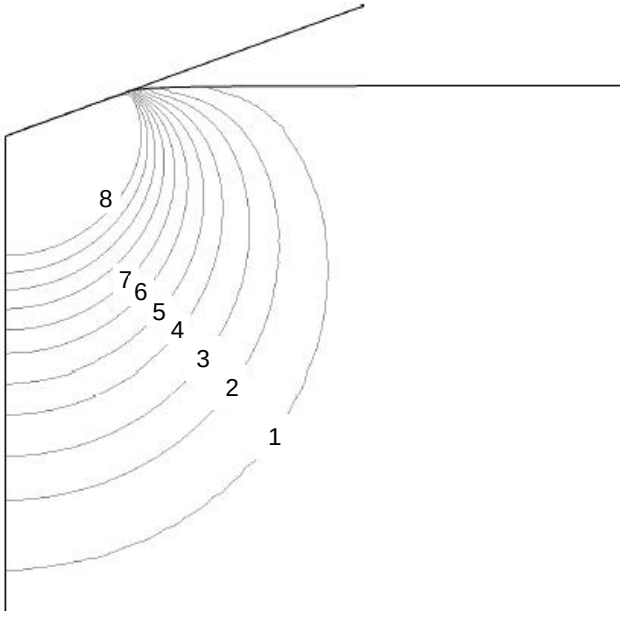

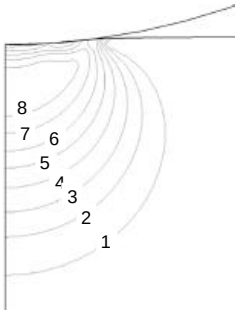

$\frac{a_s}{R} = 0{,}10$

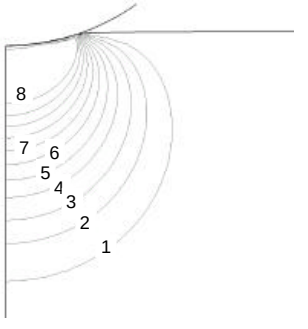

$\frac{a_s}{R} = 0{,}342$

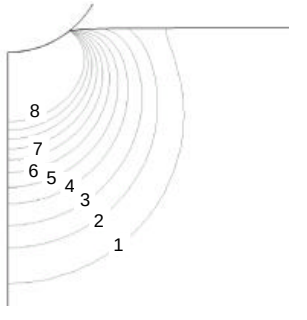

$\frac{a_s}{R} = 0{,}643$

(b)

	σ_e
1	400
2	448
3	495
4	542
5	590
6	637
7	685
8	875

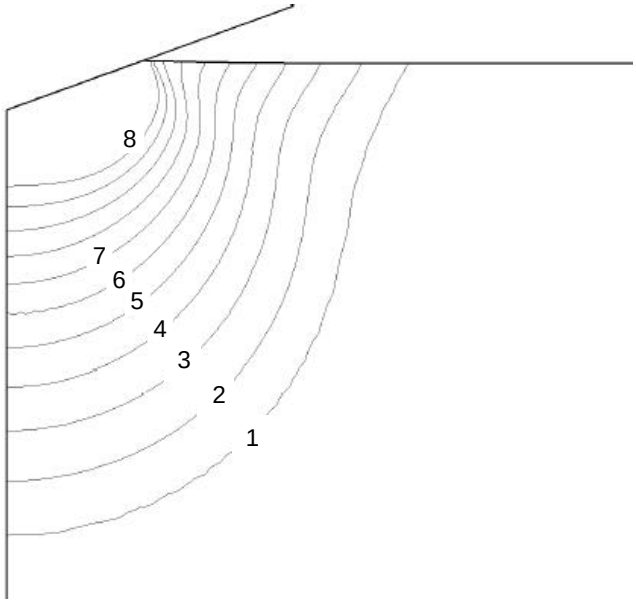

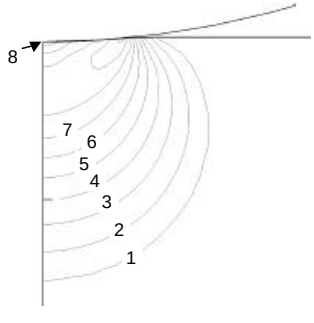

$\frac{a_s}{R} = 0{,}10$

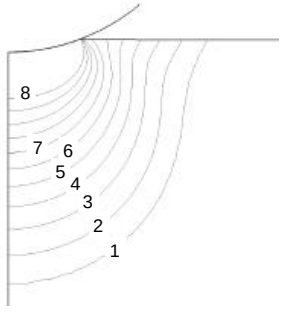

$\frac{a_s}{R} = 0{,}342$

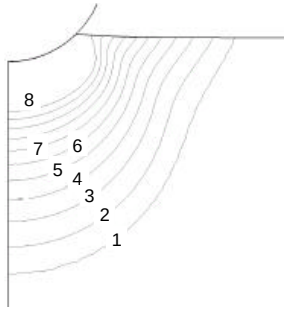

$\frac{a_s}{R} = 0{,}643$

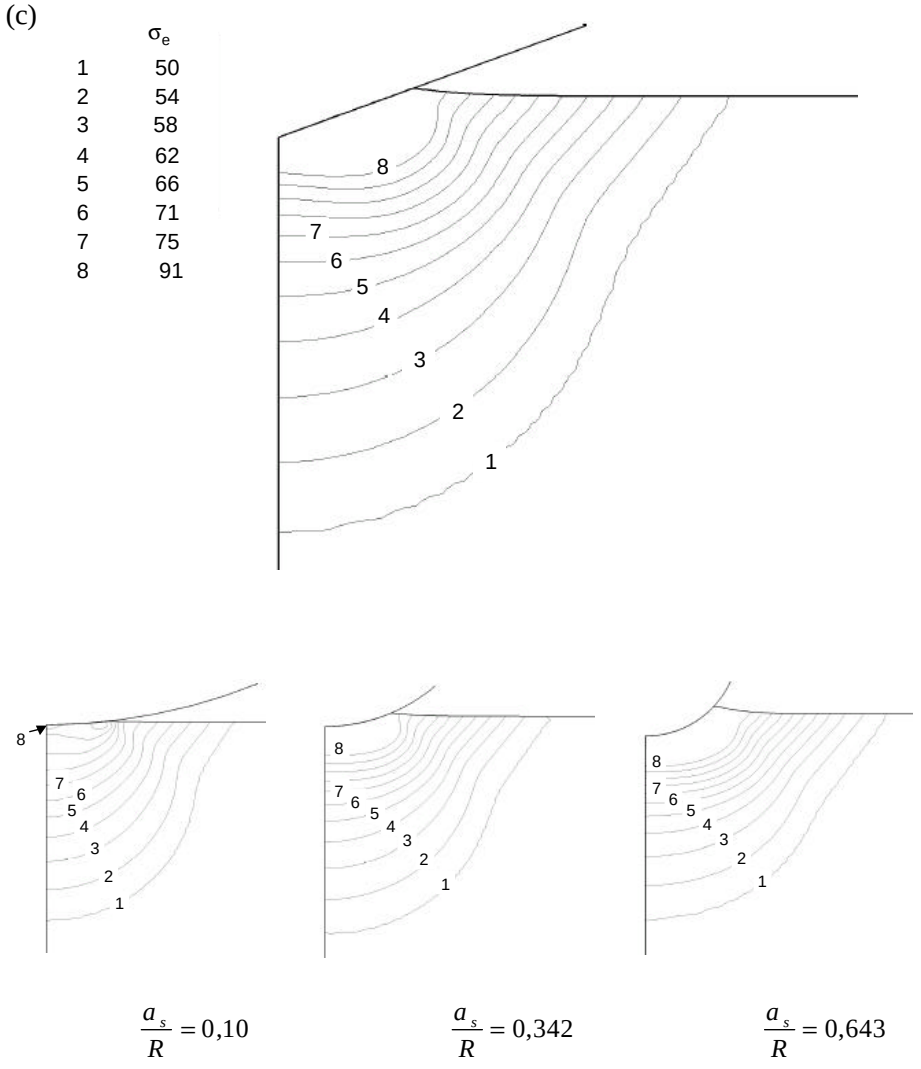

Figure 7.5: Comparison of the plastic zone size between conical and spherical indentations at different a_s/R for: (a) a highly elasto-plastic solid (E = 200 GPa, σ_{ys} = 1000 MPa, and n = 0.4), (b) an elasto-plastic solid (E = 200 GPa, σ_{ys} = 400 MPa, and n = 0.2), and (c) a fully- plastic material (E = 200 GPa, σ_{ys} = 50 MPa, and n = 0.1). Notice that for all materials, the plastic zone size in spherical indentation equals that obtained in conical indentation at $a_s/R = 0.643$ along the z-axis.

indenters $l = 1/\sin\theta$. For the Vickers and the Berkovich indenters, $l = 1.079$ and 1.101, respectively. In addition to assimilating a sharp indenter as the spherical tip replacing the cavity, Eq. (7.27) underlies a presumed constancy of the pressure distribution because, by definition, hydrostatic pressure p_{cav} takes a constant value throughout the cavity. Thus, H_{L} may only be equated to hydrostatic pressure p_{cav} in solids where the contact pressure distribution is rather constant.

Finally, one has to consider that expanding cavity formulations describe inflation of an infinite space. In this regard, comparison between such formulations and indentation experiments is attempted here along the symmetry z-axis, where the influence of the free surface is diminished. Thus, following Fig. 7.6,

$$c = z_{\mathrm{ys}} + R - h_{\mathrm{s}} = z_{\mathrm{ys}} + 1.913 a_{\mathrm{s}} \ , \tag{7.28}$$

where the equality in the right hand side holds for the particular case of a conical tip whose $\theta = 70.3°$.

7.4 Validation of the analogy

7.4.1 Elastic–perfectly plastic solids

In the following discussion, the proposed parametrical analogy between indentation experiments and the inflation of the cavity is examined. Essentially, we seek to establish the applicability of Eqs. (7.7) and (7.8) to the analysis of indentation experiments in perfectly plastic solids ($n = 0$). This is performed by recourse to the finite element simulations of conical indentation, which provide contact radius a_{s}, plastic zone size z_{ys}, and hardness H for a given solid indented to a fixed penetration depth h_{s}.

Substitution of Eqs. (7.26)–(7.28) into Eqs. (7.7) and (7.8) yields

$$\frac{H}{\sigma_{\mathrm{ys}}} = l\frac{2}{3} + l\ 2\ \ln\left(\frac{z_{\mathrm{ys}} + 1.913 a_{\mathrm{s}}}{a_{\mathrm{s}}/0.643}\right) \ , \tag{7.29}$$

$$\frac{c}{R} = \frac{z_{\mathrm{ys}} + 1.913 a_{\mathrm{s}}}{a_{\mathrm{s}}/0.643} = \left(\frac{2E}{3\sigma_{\mathrm{ys}}}\right)^{1/3} \ . \tag{7.30}$$

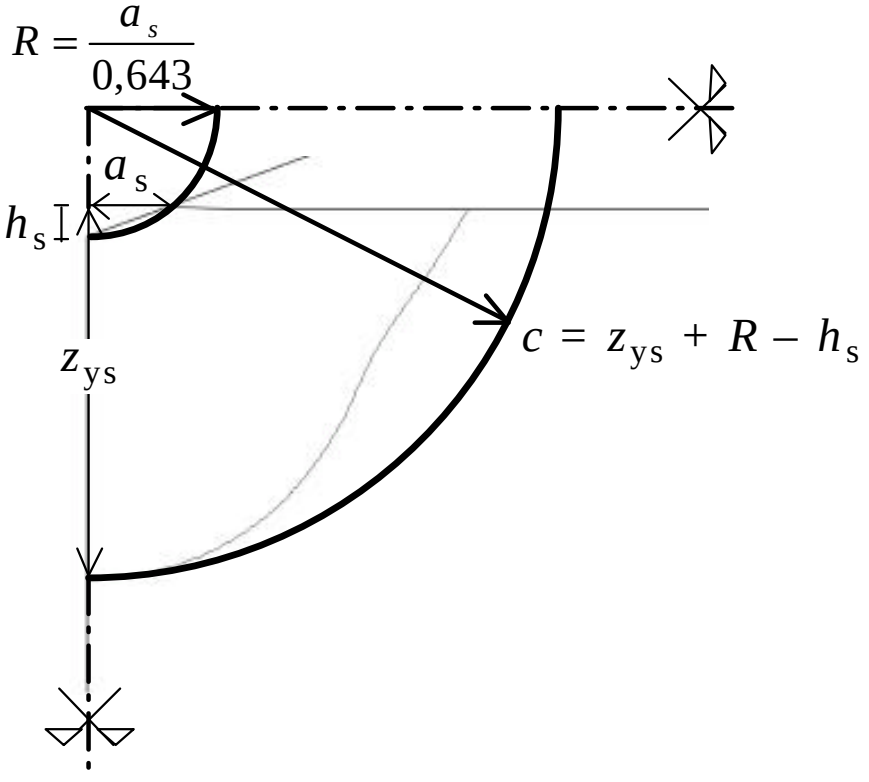

Figure 7.6: Illustration of the parametrical analogy between indentation and the expansion of a spherical cavity.

Since the finite element simulations for $n = 0$ show that $H/\sigma_{ys} = 2.57$ irrespectively of the mechanical properties of the solid (see §4), substitution of this equality into Eq. (7.29) suggests saturation of the logarithm in the right hand side and, thus, of relative plastic zone size c/R (see Figs. 7.7 and 7.8). The trends predicted through Eq. (7.29) are in very good accord with the finite element simulations. Interestingly, however, Eq. (7.30) strongly overestimates c/R and does not capture the feature of its saturation. (Note that Eq. (7.30) predicts a monotonic increase of c/R with E/σ_{ys}).

The above-mentioned discrepancy between Eqs. (7.29) and (7.30) seems to lie in the fact that integration limits $c_\circ = R_\circ = 0$ (Section 7.1.1) are not truly acceptable solutions from a physical standpoint. This is because the elastic-plastic boundary only appears following some early state, where cavity inflation is perfectly elastic. As c appears after an elastic cavity growth from $R = 0$, the solution $c_\circ = R_\circ = 0$ is exclusively valid in solids whose $\sigma_{ys} = 0$. (As it is only in such solids where plastic flow commences immediately upon inflation of the cavity.) It thus follows that it is only for $\sigma_{ys} = 0$ that the expansion of the cavity has a self-similar nature in the sense that the instantaneous plastic zone size can be obtained from any previous state, *including* $R_\circ = 0$. It is noted that the presumption of similarity was not made in deriving Eq. (7.7), from where Eq. (7.29) originated.

It is remarked that in the analogy between indentation and the expansion of the cavity proposed by Johnson [47], the cavity was taken to encompass the indenter and some of the material located directly underneath the tip. In the present work, however, the cavity has the perhaps more simple interpretation of being the indenter itself, which applies pressure to the solid. One may argue that the present analogy is somewhat arbitrary as it would have also been possible to take any alternative definition of R and c in Eq. (7.7) while changing constants 2/3 and 2 to capture the trends from the finite element simulations. In addition to strictly preserving the functional forms of expanding cavity formulations, current parametrical analogy has the advantage of holding true when the analysis of indentation experiments in *strain hardening solids* comes into its own, see Section 7.4.2.

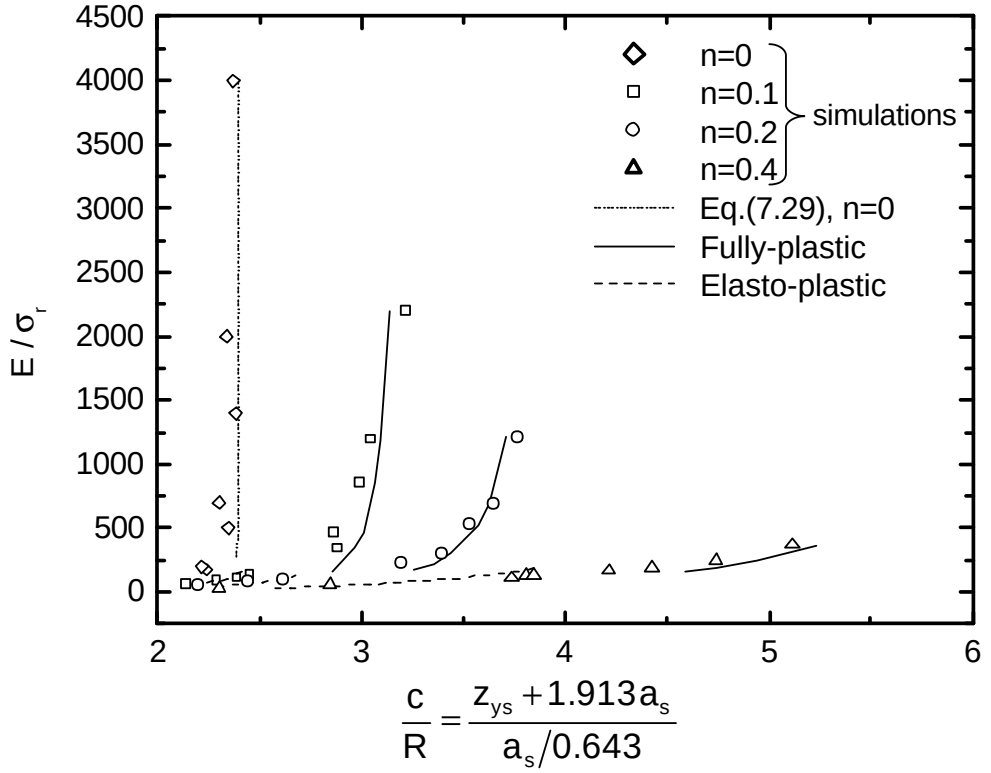

Figure 7.7: Correlation between the plastic zone size c/R in conical indentation and $E/\sigma_{\rm r}$ for the different values of n. Dotted line corresponds to the expanding cavity solution for elastic–perfectly plastic solids in Eq. (7.29) equated to $H/\sigma_{\rm ys} = 2.57$. Solid lines correspond to the fully-plastic solution for strain-hardening solids (equating Eq.(7.31) to Eq.(7.33)). Dashed lines concern the elasto-plastic solution where $\Theta_{\rm ep}$ has been used.

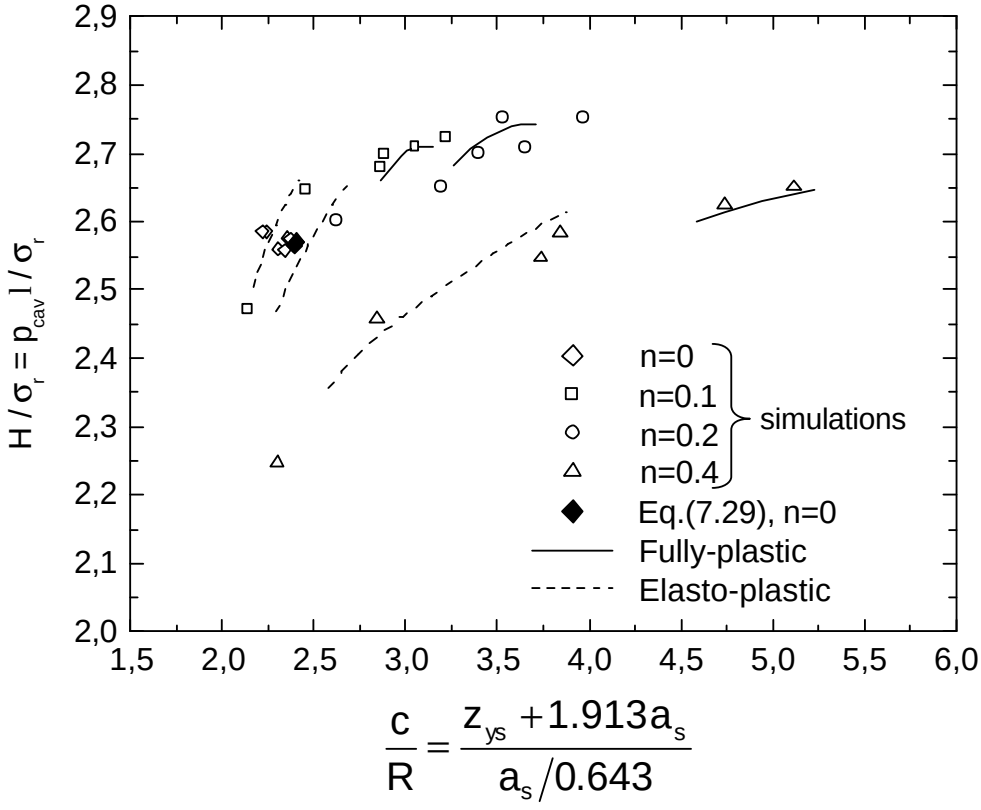

Figure 7.8: Comparison between the expanding cavity equations and the simulations of conical indentation. Solid line represents the fully plastic solution in Eq. (7.31). Dashed line corresponds to the elasto-plastic equation (Eq.(7.31) where $\Theta_{\rm ep}$) is employed.

7.4.2 Elastic–strain hardening solids

We now direct attention to the applicability of expanding cavity formulations to indentation experiments in strain-hardening solids ($n > 0$). Following present parametrical analogy (Eqs. (7.26)–(7.28)), Eq. (7.16) is rewritten as

$$\frac{H}{\sigma_{\mathrm{r}}} = l\left[\frac{2}{3}\left(\frac{\epsilon_{\mathrm{ys}}}{0.1}\right)^{n} + \Theta(n) + M(n)\left(\frac{z_{\mathrm{ys}} + 1.913a_{\mathrm{s}}}{a_{\mathrm{s}}/0.643}\right)^{P(n)}\right] . \tag{7.31}$$

Since the influence of elastic strains was neglected in deriving Eq. (7.16), Eq. (7.31) is in principle limited to solids whose contact response is plastically dominated. As elasticity is incorporated through the third term in the right hand side of Eq. (7.23) which is missing in Eqs. (7.16) and (7.31), the finite element simulations allows us to find function $\Theta_{\mathrm{ep}}(n)$ incorporating such missing terms into function $\Theta(n)$. $\Theta_{\mathrm{ep}}(n)$ is thus to be used replacing $\Theta(n)$ when elasto-plastic contact responses are at issue ($E/\sigma_{\mathrm{r}} \leq 110$ (§4)):

$$\Theta_{\mathrm{ep}} = 3.3556 + \frac{0.5122}{n} . \tag{7.32}$$

Note that $\Theta_{\mathrm{ep}}(n)$ is an approximative function in the sense that it neglects dependency on $\sigma_{\circ}$ and E of the replaced term in Eq. (7.23).

Figure 7.8 illustrates that Eq. (7.31) is an accurate formulation in solids deforming within the fully plastic regime (where original function $\Theta(n)$ is used), as well as in elasto-plastic ones (where function $\Theta_{\mathrm{ep}}(n)$ is employed). A general correlation between the uniaxial stress-strain curve and the size of the plastic zone is then found equating Eq. (7.31) to the hardness relation obtained in §5:

$$\begin{aligned}\frac{H}{\sigma_{\mathrm{r}}} = -0.0023\left[\ln\left(\frac{E}{\sigma_{\mathrm{r}}}\right)\right]^{4} + 0.0647\left[\ln\left(\frac{E}{\sigma_{\mathrm{r}}}\right)\right]^{3} - 0.6817\left[\ln\left(\frac{E}{\sigma_{\mathrm{r}}}\right)\right]^{2} \\ +3.1968\left[\ln\left(\frac{E}{\sigma_{\mathrm{r}}}\right)\right] - 2.9261\end{aligned} \tag{7.33}$$

Figure 7.7 reveals that the resulting relationship is in accordance to the finite element simulations for all fully plastic and elasto-plastic solids.

7.5 Pyramidal indentation and surface estimates of plastic zone size

The objective of this section is to illustrate how to use present framework in the assessment of the plastic zone size *at the indented surface*, as well as to extend the current analysis to Vickers and Berkovich indentation.

First, it is relevant to consider issues of indenter's tip three-dimensionality in present formulations. Following Section 7.3, the finite element simulations showed that normalized plastic zone size c/R is the same for conical and spherical indentation provided indentation strain a_s/D is set at 0.643. Along these lines, the present simulations indicate that this similarity holds for pyramidal indenters when a_s is measured at an angle of 25° from the corners of Vickers and Berkovich imprints (see Figs. 7.9(a) and (b) and Fig. 7.10).

Another important aspect in the experimental application of present framework concerns the fact that further plastic flow is promoted upon unloading from peak indentation load, see Fig. 7.11 (a) and (b). In this regard, the simulations for Vickers, Berkovich, and conical indentation show that the stress field outside the plastic zone decreases upon unloading except for the solid lying at vicinity of the free surface, where the equivalent von Mises stress increases facilitating plastic flow (see Fig. 11 (a)). Interestingly, the growth of the plastic zone at the surface depends on the contact response of the solid. Overall, it is enhanced in solids exhibiting an elasto-plastic transition rather than in those where the fully plastic regime rules the contact response. The finite element simulations indicate that when contact is elasto-plastic, further attainment of plasticity upon load removal leads to plastic zones whose shape resemble those in fully plastic contacts. Compare Fig. 7.11(a) with 7.11(b) where, upon load removal, the plastic zone size at the surface in elasto-plastic contacts bends outwards from the imprint as in fully plastic indentations. It is noted that this phenomenon is not one of reverse plasticity as plastic flow upon unloading is not induced by residual compressive stresses but, instead, by an increase in the magnitude of the tensile stresses close to the surface. Thus, consideration

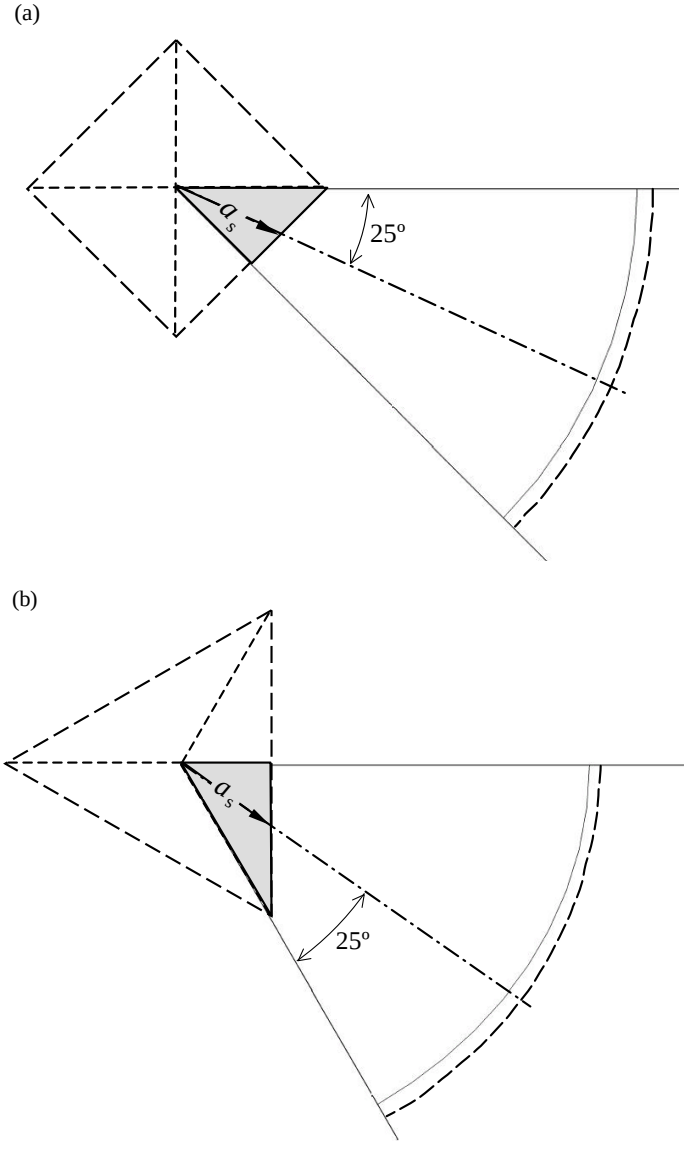

Figure 7.9: Illustration of equivalent contact radius a_s for (a) Vickers and (b) Berkovich pyramidal indentations. Solid line represents the plastic zone at peak load and dashed line gives the plastic zone upon complete unloading. The simulations are for $E = 70$ GPa, $\sigma_{ys} = 50$ MPa, and $n = 0.2$.

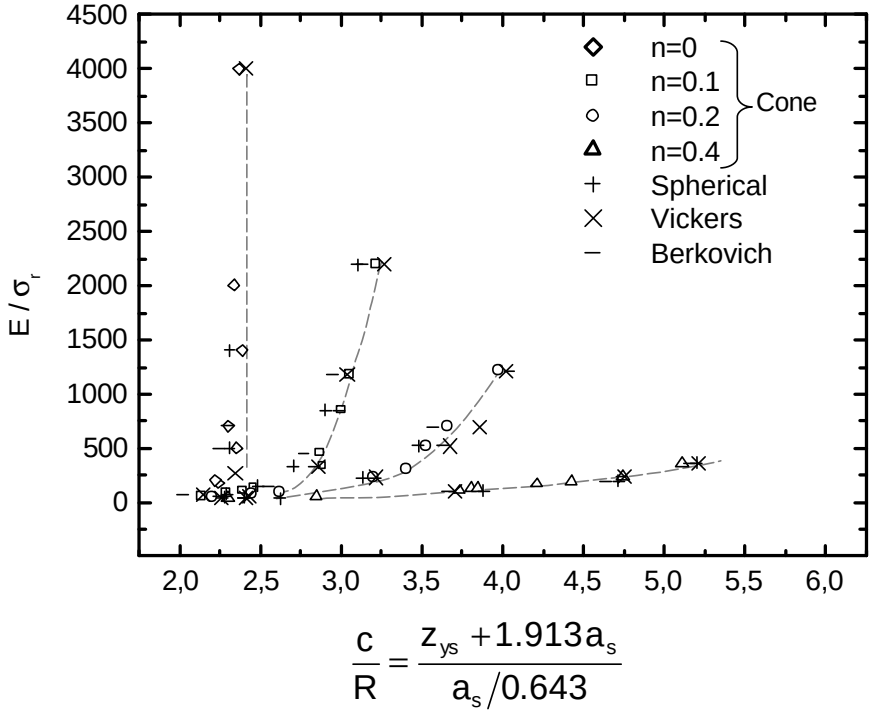

Figure 7.10: Comparison of the plastic zone size c/R between conical, spherical, and pyramidal indentations.

of kinematic hardening effects in the plasticity model shall not bring any change to the present results.

An interesting feature from the simulations of Vickers, Berkovich and conical indentation is that the plastic zone is not continuous in solids with a strong elasto-plastic character. As shown in Fig. 7.12, an unplastified surface region thus remains embedded within the plastic zone. Upon unloading, plastic flow gradually occurs at the periphery of such region, decreasing its size.

The relative increase in plastic zone size δ/c_{s} in terms of E/σ_{r} (Fig. 7.13) is found to be well fitted through

$$\frac{\delta}{c_{\mathrm{s}}} = \left(-19.754 + 1,00974\left(\frac{E}{\sigma_{\mathrm{r}}}\right)\right)^{-1/4,3} \tag{7.34}$$

for Vickers, Berkovich and conical indentations where, from the geometrical construction in Fig. 7.11,

$$\frac{c_{\mathrm{s}}}{R} = \sqrt{\left(\frac{c}{R}\right)^2 - 0.5868} \tag{7.35}$$

for the conical tip with $\theta = 70.3^{\circ}$ as well as the Vickers and the Berkovich indenters, where a_{s} is defined as in Fig. 7.9. Therefore, to estimate the plastic zone size r_{ys} at the surface, one has to calculate first c/R from Eq. (7.29) in solids where $n = 0$, or from Eq. (7.31) when $n > 0$. Then, find R through Eq. (7.26) and compute c_{s} from Eq. (7.35). Finally, δ is obtained through Eq. (7.34), so that the plastic zone size is calculated as

$$r_{\mathrm{ys}} = c_{\mathrm{s}}\,(1 - \delta) \ . \tag{7.36}$$

7.6 Summary

In this investigation, we have shown the validity of indentation models based on the expansion of a spherical cavity. This analogy sheds light into the analysis of indentation experiments either in perfectly plastic and in strain hardening media.

The following are the central findings of this chapter.

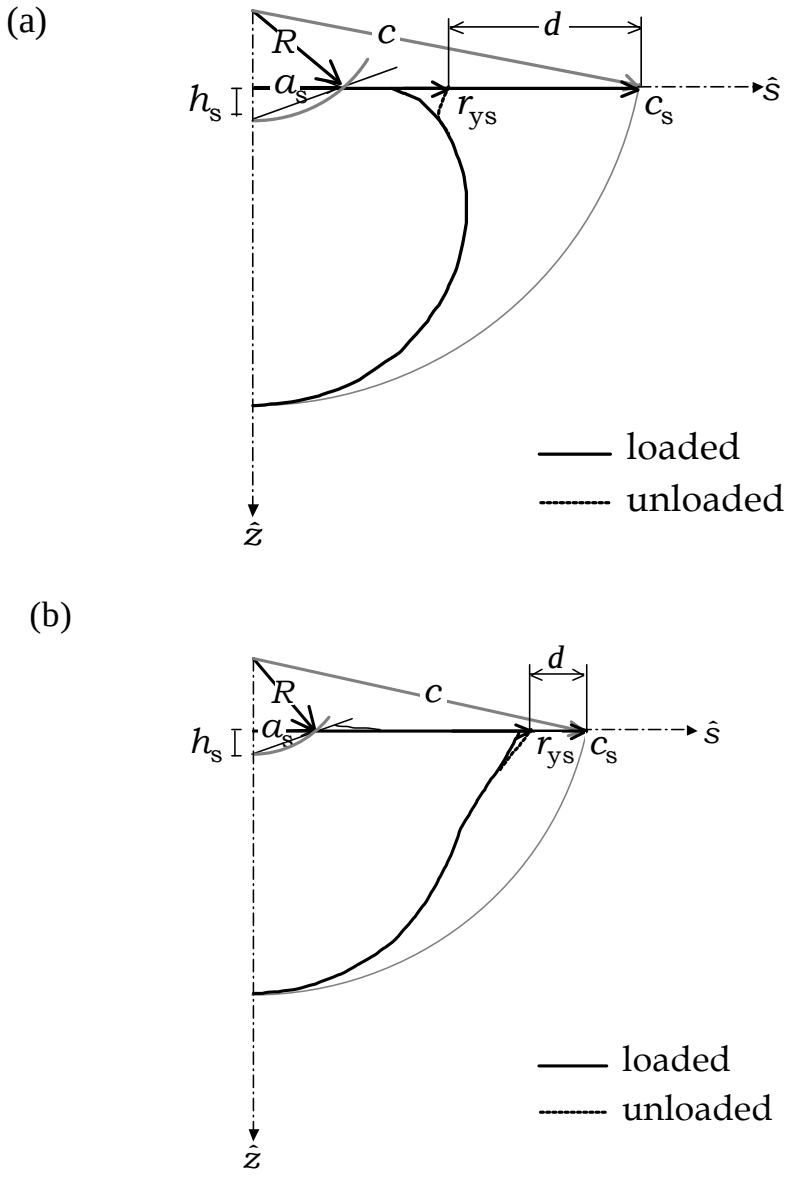

Figure 7.11: Plastic zone size for (a) an elasto-plastic solid with $E = 200$ GPa, $\sigma_{ys} = 1000$ MPa, and $n = 0.4$, and (b) a fully plastic material with $E = 200$ GPa, $\sigma_{ys} = 50$ MPa, and $n = 0.1$. Notice the growth in the plastic zone (dashed line) in the s-axis whereas the plastic zone remains constant in the z-axis.

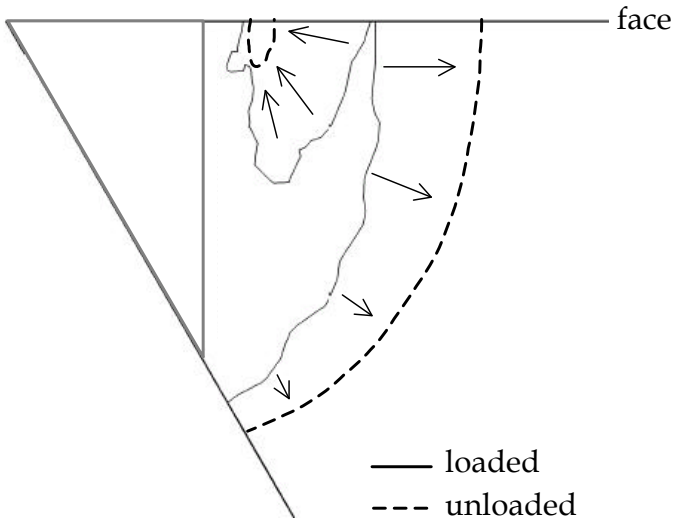

Figure 7.12: Comparison between the plastic zone for Berkovich indentation at maximum load (solid line) and upon load removal (dashed line) for a highly elasto-plastic solid (E = 70 GPa, σ_{ys} = 850 MPa, and n = 0.2). Notice the existence of an elastic region embedded within the plastic zone. Arrows indicate the direction of plastic flow upon unloading.

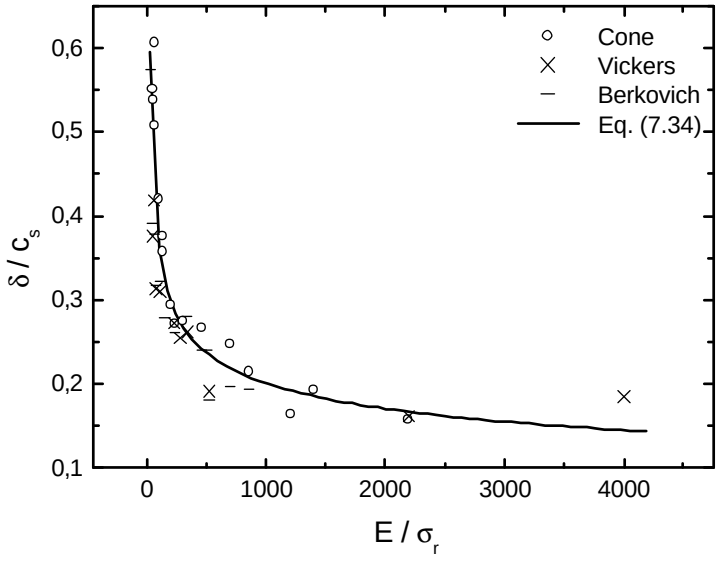

Figure 7.13: Correlation between δ/c_s and E/σ_r for the conical and the pyramidal indenters.

- Derivation of closed-form solutions for the plastic zone size cannot be strictly based on the assumption of a vanishingly small plastic zone at the commencement of cavity inflation. That is, one cannot take $R_\circ = c_\circ = 0$ because the early elastic response during cavity expansion breaks out similarity arguments. Presently derived solutions circumvent such an assumption, extending prior analysis for perfectly plastic solids to strain hardening media ($n \neq 0$). Overall, it is found that strain hardening has a profound effect on the inflation of the cavity and on the plastic zone size. Such strain hardening effects cannot be captured through a simple substitution of yield strength $\sigma_{\rm ys}$ with representative stress $\sigma_{\rm r}$ in perfectly plastic formulations (Eq. (7.1)).

- The present analysis in conjunction with finite element simulations allowed us to develop an accurate analogy between variables in expanding cavity formulations and those ruling indentation experiments. This parametrical analogy is based on the concept of an equivalent spherical indenter which, regardless of the mechanical properties of the indented material, induces the same plastic zone size as a conical tip. A distinctive feature of present parametrical analogy is that the plastic zone size in indentation experiments strictly fulfills predictions from expanding cavity formulations both in perfectly plastic solids as well as in those undergoing strain hardening effects.

- Three-dimensional finite element simulations enabled extension of the present framework to Vickers and Berkovich pyramidal indentation. It is found that the full features of the plastic zones induced by a conical indenter of tip angle $\theta = 70.3^\circ$ are maintained at an angle of 25° from the corners of Vickers and Berkovich imprints. Interestingly, considerable plastic flow may occur at the surface upon unloading from peak indentation load, increasing the plastic zone size. The overall results from the simulations allowed us to develop a simple procedure for the assessment of the true plastic zone remnant at the indented surface upon complete load removal in pyramidal and conical indentation.

Chapter 8

Summary

Comprehensive finite element simulations and analysis of conical indentation were performed in this thesis to develop a detailed physical understanding on the plastic flow features governing indentation experiments. Limited attention was also given to pyramidal (Vickers and Berkovich) and spherical indentation. This work provided (i) a sound understanding of the deformation regimes developing in sharp indentation experiments; (ii) direct correlations between hardness and the development of pileup or sinking-in around the contact boundary with uniaxial mechanical properties; (iii) a general framework for the analysis of frictional effects in the contact response; and (iv) an improved physically-based model for indentation predicated upon the analogy of the inflation of a spherical cavity.

The following are the central findings of this work.

- As the yield strength ($\sigma_{\rm ys}$) and strain hardening coefficient (n) decrease or, alternatively, as Young's modulus (E) increases, the contact regime evolves from (i) an elastic-plastic transition, to (ii) a fully plastic contact response, to (iii) a fully plastic regime where piling-up of material prevails at the contact area. In accordance with preliminary analyses by Johnson, it was found that Tabor's equation, where hardness $H = 2.7\ \sigma_{\rm r}$, strictly applies within the fully plastic regime of elastic – power-law plastic materials. The results thus confirm the concept of the

uniqueness of the characteristic strain, ϵ_{r}, $= 0.1$ that is associated with uniaxial stress, σ_{r}. A contact deformation map was then constructed to provide bounds for the elasto-plastic transition and the fully plastic contact regimes for a wide range of values of σ_{ys}, n and E.

- Mathematical formulations were derived to correlate hardness and the amount of pileup and sinking-in phenomena around sharp indenters with uniaxial mechanical properties. The formulations are applicable regardless of the deformation regime ruling the contact response of the strain hardening solid. A methodology was devised where the use of these formulations in mechanical property assessments from indentation experiments was demonstrated. The current results make contact with existing methodologies using the Π theorem in functional analysis to extract uniaxial properties from instrumented indentation load–penetration depth curves. It is argued that since surface deformation is an essential feature of the contact response, it enters directly or indirectly in such existing methodologies. The thesis illustrates how independent knowledge of surface deformation can be used to guide mechanical property assessments from load–penetration depth curves. A discussion on the uniqueness of mechanical characterizations through indentation experiments is also provided.

- The results of finite element simulations in a wide range of solids allowed us to derive two simplified equations accurately accounting for the influence of the friction coefficient on hardness. Comparisons between the simulations and instrumented micro-indentation experiments were undertaken to ensure the validity of the former to metallic materials. Quantitative estimates of the role of friction on the development of pileup and sinking-in around the contact boundary are also given in the thesis. These results provide a physical insight into the plastic flow features of distinctly different solids brought into contact against sharp indenters. Overall, the investigation shows that the amount of pileup can be used to set the range of validity of the two hardness equations indicated above. Friction has the largest

influence on the contact response of solids exhibiting considerable piling-up effects (whose parameter $\sqrt{\alpha} > 1.12$), whereas materials developing moderate pileup or sinking-in are less sensitive to friction. Finally, a methodology was devised to assess the influence of the friction coefficient on mechanical properties extracted through instrumented experiments.

- The thesis ends with an in-depth examination of the well-known analogy between indentation experiments and the expansion of a spherical cavity. Closed-form solutions were derived for the extension of the plastic zone in perfectly plastic and strain hardening solids. The theoretical analysis takes into account the role of elastic and plastic deformations in the overall contact response, leading to accurate solutions for cavity inflation. Presently proposed analogy is based on comprehensive finite element simulations of conical, spherical, and pyramidal indentation which allows us to find a correspondence between contact parameters and those from expanding cavity formulations. Such parametrical identification has the advantage to hold true in expanding cavity formulations for perfectly plastic solids as well as in those derived herein for strain hardening solids. Attention is given to the assessment of the plastic zone along the indented surface as well as to quantify the influence of further plastic flow, induced upon load removal, on the plastic zone size.

Appendix A

Appendix A

A.1 Continuum solid mechanics

A brief background on the mechanics of continuum media is given in this section. This knowledge is relevant in understanding the constitutive response and the plasticity theory used in the finite element simulations performed in this thesis. Definition of the theories and parameters governing the response of a given solid under load application thus constitutes the central topic of this section. The continuum theories given next are capable of describing the macroscopic response of the solid. Any microstructural effects shall thus be homogenized over the continuum and incorporated in the global parameters defining the macroscopic behavior of the material. The theories are limited to those involving temperature-independent deformation processes. We first examine the principles and constitutive relations for elastic deformations. Then, we analyze plastic deformations and the underlying constitutive theories. Comprehensive text books are available providing detailed descriptions of such plasticity theories [42; 56; 57].

A.1.1 Elasticity theory

The constitutive theory of elasticity is based on the existence of a simple relation between the stress tensor and the strain tensor of the form $\sigma = \sigma(\epsilon)$. The linearization of the stress-strain relation leads to the *generalized Hooke's law*

$$\sigma_{ij} = C_{ijkl}\epsilon_{kl} \tag{A.1}$$

where σ_{ij} is the ij-stress component, ϵ_{kl} is the kl-strain component, and C_{ijkl} is the tensor containing the elastic constants or *stiffness matrix*. By virtue of the symmetries of the stress tensor, where the solid may be taken as homogeneous and isotropic, the 81 components in tensor C_{ijkl} can be reduced to 2.

The simplest case of elasticity is that found in *isotropic linear elastic solids*, leading to the following stiffness tensor:

$$\lambda\delta_{ij}\delta_{kl} + \mu\delta_{ik}\delta_{jl} + \gamma\delta_{il}\delta_{jk} \ , \tag{A.2}$$

where δ_{ij} is the Kronecker delta. To satisfy the symmetry of the stress tensor $C_{ijkl} = C_{jikl}$, $\mu = \gamma$. Introducing this result into Eq.(A.2) leads to

$$\sigma_{ij} = \lambda\delta_{ij}\epsilon_{kk} + 2\mu\epsilon_{ij} \ . \tag{A.3}$$

Constants λ and μ are the *Lamé coefficients*. Constant μ is referred to as shear modulus G, and both λ and μ are related to Young's modulus E and Poisson's ratio ν [56]. Equivalently, Eq. (A.3) is rewritten as

$$\epsilon_{ij} = \frac{1}{E}\left((1+\nu)\sigma_{kk} - \nu\sigma_{kk}\delta_{ij}\right) \ . \tag{A.4}$$

A particular case is obtained under uniaxial conditions, where non-vanishing stress is $\sigma = \sigma_{11}$, and $\epsilon_{11} = \epsilon$, so that

$$\sigma = E\epsilon \ . \tag{A.5}$$

An important element in elasticity theory is due to Green, who introduced conjugate energy functions where

$$\epsilon_{ij} = \frac{\partial \Phi}{\partial \sigma_{ij}} \quad \text{and} \quad \sigma_{ij} = \frac{\partial \Psi}{\partial \epsilon_{ij}} \, . \tag{A.6}$$

These functions can be taken so that a linear relation between stresses and strains emerges (linear hyperelasticity). However, is also possible to define such functions so that the dependency of stresses and strains becomes non-linear. The latter is employed in the analysis of plastic flow phenomena (where it is no longer possible to assume linearity between stresses and strains).

A.1.2 Plasticity theories

Several theories are available to describe the plastic response of solids subjected to a complex stress state. The more complete incremental theories of plasticity are usually referred to as *flow theories*. Essentially, they combine a *yield condition*, which prescribes the stress combinations inducing plastic deformations; with a description of the *postyield behavior*, which sets the relation between plastic strain increments and the stress components as well as the variation in the yield condition caused by strain-hardening phenomena. On the other hand, simple *deformation theories* prescribe the total strain as a function of the current stress disregarding the strain history of the solid.

Flow theory

The yield condition for continuum solids whose response is rate-independent postulates that *there exists a function* $f(\boldsymbol{\Sigma})$ *of the stress* $\boldsymbol{\Sigma}$ *so that the material remains elastic for*

$$f(\boldsymbol{\Sigma}) < 0 \;\; \text{or} \; f(\boldsymbol{\Sigma}) = 0 \;\; \text{and} \;\; \frac{\partial f}{\partial \Sigma_{ij}} \dot{\Sigma}_{ij} < 0 \tag{A.7}$$

and becomes plastic for

$$f(\mathbf{\Sigma}) = 0 \quad \text{and} \quad \frac{\partial f}{\partial \Sigma_{ij}} \dot{\Sigma}_{ij} \geq 0 \tag{A.8}$$

being $f(\mathbf{\Sigma}) \leq 0$ *always.*

One can visualize function $f(\mathbf{\Sigma}) = 0$ as a surface in stress space, and interpret the conditions in Eq.(A.8) so that all possible stress states inside the region enclosed by the yield surface are elastic, while all the stress states at the surface are plastic. The plastic loading condition $(\partial f/\partial \Sigma_{ij})\ \dot{\Sigma}_{ij} \geq 0$ thus ensures that plastic deformation proceeds over time as the stress state cannot evolve towards the elastic region. Notice that yield surface $f(\mathbf{\Sigma})$ contains material parameters which may vary over time, so that $f(\mathbf{\Sigma})$ remains equal to zero as plastic deformation proceeds.

In the present thesis, we assume that the material follows the Levy-Mises yield condition,

$$f(\mathbf{\Sigma}) \equiv J_2 \ - \ k^2 = 0 \ , \tag{A.9}$$

where J_2 is the second invariant of the stress deviator $\mathbf{\Sigma}'$ [42; 56; 57]. While k is constant in perfectly plastic solids, it increases during deformation of strain-hardening materials. Figure A.1 illustrates the yield surface for the simple case of biaxial stress (Σ_{11} and Σ_{22}). As plastic deformation proceeds, the isotropic-hardening Levy-Mises theory indicates that the yield surface shall maintain its shape and enlarge in such a way that any instantaneous stress state cannot be located outside the current yield surface.

Metal plasticity theories particularize the general yield condition in Eq.(A.8) to fulfill the following conditions:

Yield is independent of hydrostatic pressure. This implies that the yield surface is an exclusive function of stress deviator $\mathbf{\Sigma}'$ (${\Sigma_{ij}}' = \Sigma_{ij} - \frac{1}{3}\Sigma_{mm}\delta_{ij}$). This assumption gives a good description of plastic deformation processes in metallic materials, as dislocation slip is independent of the spherical part of the stress tensor [42; 57]. Therefore, the yield surface in Eq.(A.8) reads

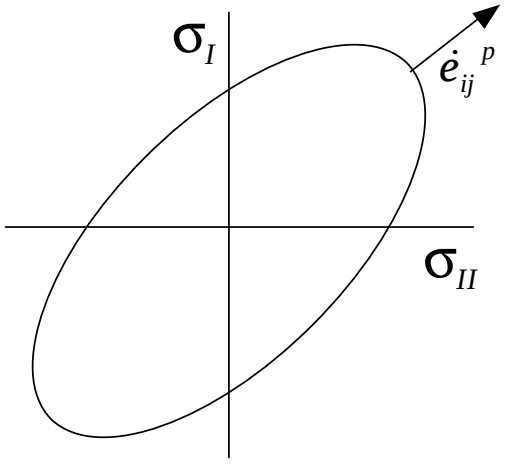

Figure A.1: Schematic of the yield surface in the principal stresses σ_{I}–σ_{II} plane (biaxial stress state).

$$f(\boldsymbol{\Sigma}) = f(\boldsymbol{\Sigma}') = 0 \ . \tag{A.10}$$

The material is isotropic. This assumption indicates that since there are no preferred directions in the solid, function $\boldsymbol{\Sigma}$ has the same form in any orientation within the material. Without considering Eq. (A.10), the yield condition in terms of stress components Σ_{ij} reads

$$f(\boldsymbol{\Sigma}) = f(\Sigma_{11}, \Sigma_{22}, \Sigma_{33}, \Sigma_{23}, \Sigma_{31}, \Sigma_{13}) \tag{A.11}$$

or, using principal stresses σ_1, σ_2, σ_3, and principal directions $\hat{\mathbf{n}}_\mathbf{1}$, $\hat{\mathbf{n}}_\mathbf{2}$, $\hat{\mathbf{n}}_\mathbf{3}$,

$$f(\boldsymbol{\Sigma}) = f(\sigma_1, \sigma_2, \sigma_3, \hat{\mathbf{n}}_\mathbf{1}, \hat{\mathbf{n}}_\mathbf{2}, \hat{\mathbf{n}}_\mathbf{3}) \ . \tag{A.12}$$

Isotropy indicates that (i) f cannot depend on the orientation $\hat{\mathbf{n}}_\mathbf{i}$ of the principal stresses, and (ii) the dependency of f upon the principal stress components σ_i is indistinguishable so that f is a symmetric function of σ_1, σ_2, σ_3. Hence, the yield surface can be expressed through any linear combination of the three principal stresses σ_1, σ_2, σ_3. Since any stress combination is described through stress invariants I_1, I_2, I_3, the yield condition can be rewritten as

$$f(\boldsymbol{\Sigma}) = f(I_1, I_2, I_3) \ . \tag{A.13}$$

Together with the assumption of the independency of yield on hydrostatic pressure, f can then be expressed as a function of deviatoric stress invariants J_2 and J_3 (since $J_1 \equiv 0$)

$$f(\boldsymbol{\Sigma}) = f(J_2, J_3) \ . \tag{A.14}$$

The yield surface is symmetric. $f(-\boldsymbol{\Sigma}) = f(\boldsymbol{\Sigma})$. In accordance with the assumption of material isotropy, yield locus has to be symmetric with respect to the axis of the stress space. This postulate implies an additional symmetry of the yield surface with respect to the origin. From a physical standpoint, this condition excludes materials exhibiting

Bauschinger effects, where load reversal causes plastic flow at stresses whose magnitude lies below those applied in the original loading path.

The von Mises yield criterion is known to fulfill the above assumptions, as well as to consider that plastic flow is independent of the third invariant J_3:

$$f = f(J_2) = \frac{1}{6}\left[(\sigma_1 - \sigma_2)^2 + (\sigma_2 - \sigma_3)^2 + (\sigma_3 - \sigma_1)^2\right] \; - \; k^2 = 0 \; , \tag{A.15}$$

or using the principal deviatoric stress components s_1, s_2, s_3,

$$f = f(J_2) = \frac{1}{2}\left[{s_1}^2 + {s_2}^2 + {s_3}^2\right] \; - \; k^2 = 0 \; . \tag{A.16}$$

Figure A.2 gives a schematic representation of such yield surface on the principal stress space, where the von Mises condition is depicted as a cylinder oriented parallel to the hydrostatic line ($\sigma_1 = \sigma_2 = \sigma_3$), whose section is the deviatoric plane ($\sigma_1 + \sigma_2 + \sigma_3 = 0$).

In addition to the above postulates on the yield surface, a flow theory of plasticity incorporates a plastic flow potential function. Such potential is described in terms of generalized variables which prescribe the mechanical behavior of the material for any type of external solicitations. Thus, at each material point i, the generalized stresses $\mathbf{Q}_i$ and their conjugate rates of deformation $\dot{\mathbf{q}}_i$ are defined. In the three-dimensional formulation, the nine components of the generalized stress $\mathbf{Q}_i$ are the nine stress components Σ_{ij}, and the deformation rate is identified as $\mathrm{d}\epsilon_{ij}/\mathrm{d}t$. These variables allow one to define the *plastic potential function* as the function f of $\mathbf{Q}_i$ that prescribes the rate of plastic deformation $\dot{\mathbf{q}}_i^{pl}$,

$$\dot{\mathbf{q}}_i^{pl} = \dot{\lambda}\frac{\partial f}{\partial \mathbf{Q}_i} \; , \tag{A.17}$$

where $\dot{\lambda}$ is a scalar function. We shall note that for stable plastic solids [57] the plastic potential function exists and it is identical to the yield function, which must represent a convex surface in the stress space. [Quoting Drucker's definition, a stable plastic material is one where "(i) the plastic work done by the external agency during the application

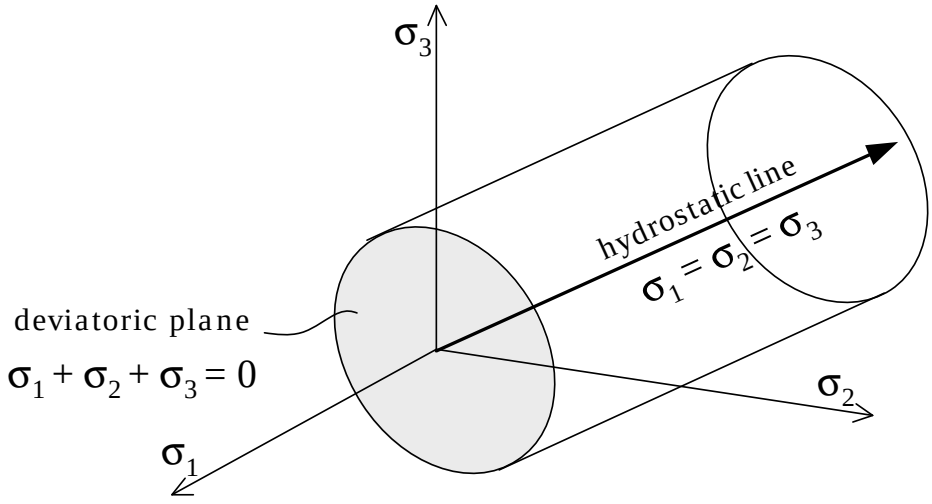

Figure A.2: Von Mises yield surface in the principal stresses space (σ_1, σ_2, σ_3) for a generic three-dimensional stress state.

of additional stresses is positive, and (ii) the net total work performed by the external agency during the cycle of adding and removing stresses is non-negative".]

Geometrical interpretation of the plastic potential in Eq.(A.17) leads to the conception that the plastic rate of deformation $\dot{\mathbf{q}}^{pl}$ is parallel to the outer normal at a point $\mathbf{Q}$ of yield surface f. Since the outer normal to the yield surface is parallel to the deviatoric plane in the von Mises plasticity model described above, plastic deformations are also deviatoric and there are no plastic volume changes.

Finally, the evolution of the yield function during plastic deformation is obtained through the work-hardening behavior. Several simplifications can be made upon the strain-hardening response: perfect plasticity (where yield surface is constant during plastic flow), isotropic hardening, and kinematic hardening. Isotropic hardening is assumed in this thesis so that the yield surface maintains its shape while its size increases. This behavior is controlled by a single parameter depending on plastic deformation. On the other hand, capturing anisotropic deformation phenomena such as Bauschinger effects necessarily requires consideration of a non-isotropic (kinematic) hardening theory. Under the isotropic hardening hypothesis, it is possible to find the explicit form of scalar $\dot{\lambda}$ in Eq.(A.17) using two scalar quantities prescribing a generalized stress-strain relation. The scalar stress is defined as the *effective stress* $\bar{\sigma}$, which measures the size of the von Mises yield surface as

$$\bar{\sigma} = \sqrt{3J_2} = \sqrt{\frac{3}{2} s_{ij} s_{ij}} \ . \tag{A.18}$$

The scalar strain is the *effective plastic-strain increment* $\mathrm{d}\bar{\epsilon}^{pl}$, defined as

$$\mathrm{d}\bar{\epsilon}^{pl} = \sqrt{\frac{2}{3} \mathrm{d}\epsilon^{pl}{}_{ij} \mathrm{d}\epsilon^{pl}{}_{ij}} \ . \tag{A.19}$$

The numerical factors in Eq.(A.18) and Eq.(A.19) are chosen so that under uniaxial stress (Σ_{11}) one has $\bar{\sigma} = \Sigma_{11}$ and $\mathrm{d}\bar{\epsilon}^{pl} = \mathrm{d}\epsilon^{pl}{}_{11}$. Combination of the von Mises yield condition (Eq.(A.9)), the plastic potential function (Eq.(A.17)), and the above definitions leads to

$$\mathrm{d}\epsilon^{pl}{}_{ij} = \frac{3}{2}\frac{\mathrm{d}\bar{\epsilon^{pl}}_{ij}}{\bar{\sigma}} s_{ij} \ , \tag{A.20}$$

which determines the evolution of the plastic strains in terms of known variables.

The concepts of effective stress and effective strain are used to generalize the uniaxial stress-strain relations to triaxial states. Stress-strain relations obtained from uniaxial tests in metallic materials are usually well fitted through the piece-wise equation

$$\sigma = \begin{cases} E\epsilon & \epsilon \leq \epsilon_{\mathrm{ys}}, \\ \sigma_{\circ}\epsilon^{n} & \text{otherwise} \end{cases} \ , \tag{A.21}$$

where the first part accounts for the elastic response and the second part describes plastic deformations. Parameter n is the hardening coefficient, and $\sigma_{\circ} = \sigma_{\mathrm{ys}}^{(1-n)} E^{n}$ for continuity at ϵ_{ys}. An alternative model regards solids exhibiting linear strain hardening, so that the stress-strain relation reads

$$\sigma = \begin{cases} E\epsilon & \epsilon \leq \epsilon_{\mathrm{ys}}, \\ m\ \epsilon & \text{otherwise} \end{cases} \ , \tag{A.22}$$

where m is the linear plastic hardening slope, which has dimensions of stress. Figure A.3 is an schematic illustration of Eq.(A.21) and Eq.(A.22).

Limiting values of E, n, and σ_{ys} provide idealized cases that are of special interest in contact mechanics. These model responses are shown in Fig. A.4.

Box in Fig. A.5 summarizes the main features of the J_2 flow theory where the plastic flow potential function is taken to be associated to the von Mises yield condition. This model is adopted in the finite element simulations performed in this thesis (§3).

Deformation theories

The principal assumption in a deformation theory of plasticity is that the correlation between the plastic strains and the stresses is fully prescribed through a state equation. These theories neglect strain history, as any instantaneous strain only depends on the actual stress state. The main advantage of deformation theories of plasticity is that their mathematical treatment is more simple than that of flow theories. Deformation theories

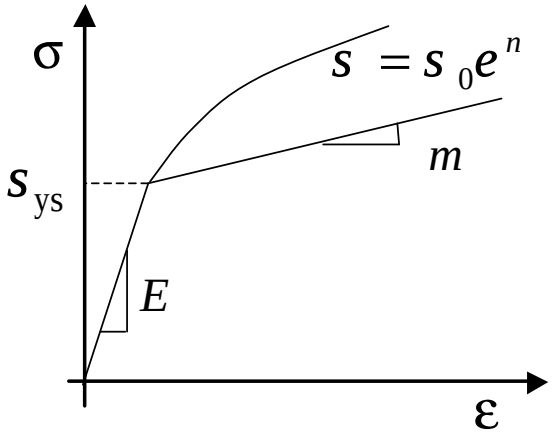

Figure A.3: Stress-strain curve for an elastic–power-law plastic solid, and elastic–linear plastic solid.

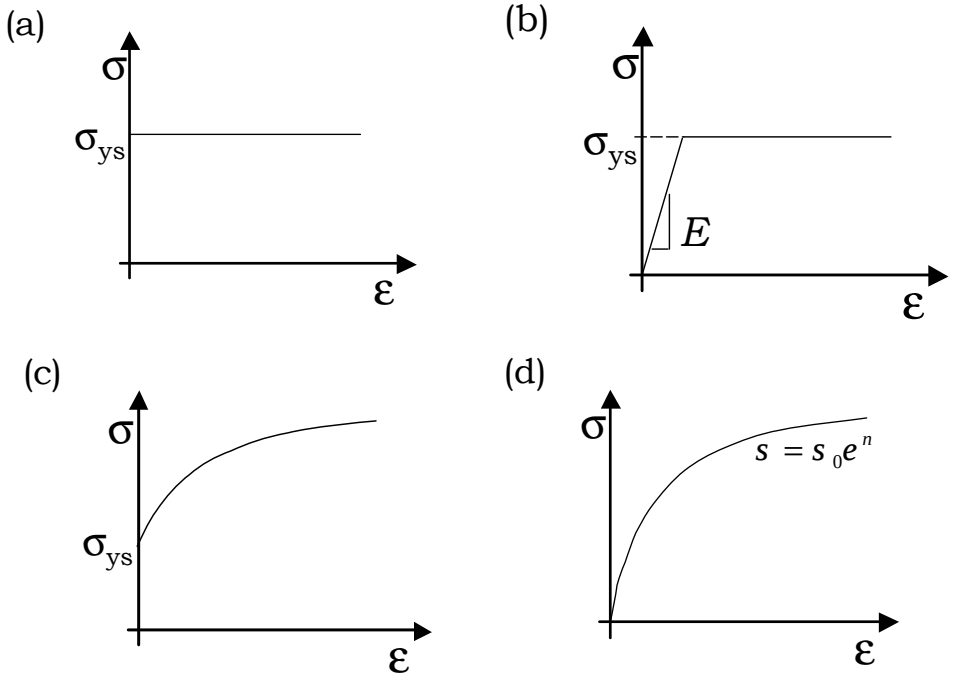

Figure A.4: Idealized stress-strain relations. (a) Rigid–perfectly plastic, (b) elastic–perfectly plastic, (c) rigid–power-law plastic, and (d) power-law plastic ($\sigma_{\mathrm{ys}} = 0$).

J_2 associated flow plasticity model

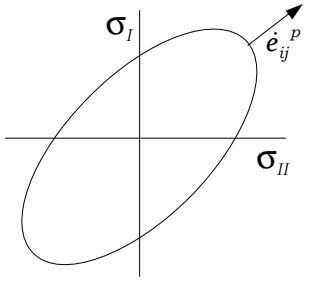

Flow surface

- Von Mises yield surface:

$$f(s_{ij}) \equiv J_2 - k^2 = \frac{1}{2} s_{ij} s_{ij} - k^2 = 0$$

- Associated flow rule:

$$\dot{e}_{ij}^{\,p} = \frac{2}{3} \dot{e}_e^{\,pl} \frac{s_{ij}}{s_e} \quad ; \quad \begin{cases} \dot{e}_e^{\,pl} = \sqrt{\frac{2}{3} \dot{e}_{ij}^{\,pl} \dot{e}_{ij}^{\,pl}} \\ s_e = \sqrt{\frac{3}{2} s_{ij} s_{ij}} \end{cases}$$

- Constitutive equation:

$$e = \begin{cases} s / E & s \le s_{ys} \\ s_{ys} / E \quad (s / s_{ys})^{1/n} & s > s_{ys} \end{cases}$$

Figure A.5: Main features of the J_2 flow plasticity model.

are accurate for simple loading cases in which the stresses evolve in a radial path in the stress space.

In a deformation theory, the material can be taken to fulfill the von Mises yield condition, and the finite strain E_{ij} to be the sum of the elastic ${E^{el}}_{ij}$ and the plastic ${E^{pl}}_{ij}$ parts of the deformation. These components are obtained separately from their corresponding stress-strain relation, where

$$E_{ij} = {E^{el}}_{ij} + {E^{pl}}_{ij} \ . \tag{A.23}$$

The elastic finite deformation components ${E^{el}}_{ij}$ are linked to the total stress components Σ_{ij} and deviatoric stresses ${\Sigma'}_{ij}$ as

$${E^{el}}_{kk} = \frac{1-2\nu}{E}\Sigma_{kk} \qquad {E'^{el}}_{ij} = \frac{1}{2G}{\Sigma'}_{ij} \ . \tag{A.24}$$

Plastic finite strains ${E^{pl}}_{ij}$ are taken to be proportional to the deviatoric stress components ${\Sigma'}_{ij}$,

$${E^{pl}}_{ij} = \phi {\Sigma'}_{ij} \ , \tag{A.25}$$

where ϕ is a proportionality scalar function. This scalar is a function of the equivalent stress $\bar{\sigma}$ and the equivalent strain $\bar{\epsilon}^{pl}$, defined in Eq.(A.18) and Eq.(A.19),

$$\phi = \frac{2}{3}\frac{\bar{\epsilon}^{pl}}{\bar{\sigma}} \ . \tag{A.26}$$

Thus, the stress-strain relation in a simple uniaxial test provides the value for ϕ. Note that there is no "plastic" unloading criterion, as this model is based on non-linear elasticity formulations.

Published articles

Mata, M., Anglada M., Alcalá, J., 2002. *Contact deformation regimes around sharp indentations and the concept of the characteristic strain.* J. Mater. Res. 17, 964–976.

Mata, M., Anglada M., Alcalá, J., 2002. *A hardness equation for sharp indentation of elastic–power-law strain-hardening materials.* Phil Mag. A. 82, 1831–1839.

Mata, M., Alcalá, J., 2003. *Mechanical property evaluation through indentation experiments in elasto-plastic and fully plastic contact regimes.* J. Mater. Res. 18, 1705–1709.

Mata, M., Alcalá, J., 2004. *The role of friction in sharp indentation.* J. Mech. Phys. Solids, 52, 145–165.

Casals, O., Mata, M., Alcalá, J., 2004. *The duality in mechanical property extractions from Vickers and Berkovich instrumented indentation experiments.* Acta Mater., in revision.

Mata, M., Casals, O., Alcalá, J., 2004. *The plastic zone in indentation experiments.* Submitted to J. Mech. Phys. Solids.

Bibliography

[1] ABAQUS User's manual, V5.8, 1998. Hibbit, Karlsson and Sorensen, Inc., Providence R.I. 3.1.1, 6.1.2

[2] Alcalá, J., Giannakopoulos, A.E., Suresh, S., 1998. Continuous measurements of load–penetration curves with spherical microindenters and the estimation of mechanical properties. J. Mater. Res. 13, 1390–1400. 1.1.1, 5

[3] Alcalá, J., Barone, A.C., Anglada, M., 2000. The influence of plastic hardening on surface deformation modes around Vickers and spherical indents. Acta mater. 48, 3451–3464. (document), 1.1.1, 1.1.1, 1.1.1, 3.6, 3.2.3, 3.3, 5.3, 5.4

[4] Alcalá, J., 2000. Instrumented indentation of Zirconia Ceramics. J. Am. Ceram. Soc. 83, 1977–1984. 1.1.1, 3.2.3, 5

[5] Alcalá, J., Gaudette, F., Suresh, S., Sampath, S., 2001. Instrumented spherical micro-indentation of plasma-sprayed coatings. Mater. Sci. Eng. A 316, 1. 5

[6] Barenblatt, G. I., 1996. Scaling, self-similarity, and intermediate asymptotics. Cambridge University Press, United Kingdom. 1.1, 1.2, 1.2

[7] Beeuwkes, R., Chait, R., Lin, H.H., 1973. The practical determination of flow curves by indentation hardness methods, in The Science of Hardness Testing and its Research Applications (Eds. J.H. Westbrook and H. Conrad). American Society for Metals, Ohio. 6.4

[8] Bhattacharya, A.K., Nix, W.D., 1988. Finite element simulation of indentation experiments. Int. J. Solids Struct. 24, 881–891. 6

[9] Bignoni, D., Ludiero, F. , 1989. The quasi-static finite cavity expansion in a non-standard elasto-plastic medium. Int. J. Mech. Sci. 31, 825–837. 7

[10] Bishop, R.F., Hill, R., Mott, F.R.S., 1945. The theory of indentation and hardness tests. Proc. Phys. Soc. 57, 147–159. 1.1, 1.1.2, 5.1, 5.1, 7

[11] Biwa, S., Storåkers, B., 1995. An analysis of fully plastic Brinell indentation. J. Mech. Phys. Solids. 43, 1303–1333. 1.1, 1.2.1, 5.3

[12] Bobji, M.S., Biswas, S.K., 1999. Deconvolution of hardness from data obtained from nano- indentation of rough surfaces. J. Mater. Res. 14, 2259–2268. 6.4

[13] Bolshakov, A., Pharr, G.M., 1998. Influence of pileup on the measurement of mechanical properties by load and depth sensing indentation techniques. J. Mater. Res. 13, 1049–1058.

[14] Borodich, F.M., 1998. Similarity methods in Hertz contact problems and their relations with the Meyer hardness test. Technical report. 1.1, 1.2, 1.2.1, 1.2.1, 1.2.1

[15] Borodich, F. M., Keer, L. M., 2004. Contact problems and depth-sensing nanoindentation for frictionless and frictional boundary conditions. Int. J. Solids Structures 41, 2479-2499.

[16] Bouzakis, K.-D., Michailidis, N., Hadjiyannis, S., Skordaris, G., Erkens, G., 2003. The effect of specimen roughness and indenter tip geometry on the determination accuracy of thin hard coatings stress-strain laws by nanoindentation. Mater. Charact. 49, 149–156. 6.4

[17] Bower, A.F., Fleck, N.A., Needleman A., Ogbonna N., 1993. Indentation of power law creeping solid. Proc. R. Soc. Lond. A. 441, 97–124. 1.1.2, 6

[18] Cao, Y. P., Lu, J., 2004. A new method to extract the plastic properties of materials from an instrumented spherical indentation loading curve. Acta Mater., 52, 13, 4023-4032. 1.2, 5.5

[19] Carlsson, S., Biwa, S., Larsson, P.L., 1999. On frictional effects at inelastic contact between spherical bodies. Int. J. Mech. Sci. 42, 107–128. 1.1.2, 6

[20] Casals, O., Mata, M., Alcalá, J., 2004. The duality in mechanical property extractions from Vickers and Berkovich instrumented indentation experiments. Submitted to Acta Mater. (document), 7.2, 7.3

[21] Chadwick, P., 1959. The quasi- static expansion of a spherical cavity in metals and ideal soils. Quart. J. Mech. and Applied Math. 12, 52–71. 1.1, 5.1, 7, 7.1.1

[22] Chaudhri, M.M., 1998. Subsurface strain distribution around Vickers hardness indentations in annealed polycrystalline copper. Acta Mater. 46, 3047–3056. 1.1.2, 3.3, 3.3, 4, 4.1, 4.1

[23] Cheng, Y.T., Cheng, C.M., 1998. J. Appl. Phys. 84, 1284. 5

[24] Cheng, Y.T., Cheng, C.M., 1998. Appl. Phys. Lett. 73, 614. 5

[25] Cheng, Y.T., Cheng, C.M., 1999. Scaling relationships in conical indentation of elastic perfectly plastic solids. Int. J. Solids Struct. 36, 1231–1243. 1.1.1, 5

[26] Cheng, Y.T., Cheng, C.M., 1999. Can stress-strain relationships be obtained from indentation curves using conical and pyramidal indenters?. J. Mater. Res. 14, 3493–3496. 1.1.1, 4, 5, 5.5

[27] Cheng, Y.T., Li, Z., 2000. Hardness obtained from conical indentations with various cone angles. J. Mater. Res. 45, 2830–2835. 1.1.2, 4, 4.1, 5.5

[28] Chiang, S.S., Marshall, D.B., Evans, A.G., 1982. The response of solids to elastic/plastic indentation. I. Stresses and residual stresses. J. Appl. Phys. 53, 298–311. 1.1, 5.1, 7, 7

[29] Chiu, Y.L., Ngan, A.H.W., 2002. A TEM investigation on plastic zones in Ni3Al(Cr,B) single crystals. Acta Mater. 50, 2677–2691. 7, 7

[30] Dao, M., Chollacoop, N., Van Vliet, K. J., Venkatesh, T. A., Suresh, S., 2001. Computational modelling of the forward and reverse problems in instrumented indentation. Acta mater. 49, 3899–3918. 1.1.1, 4, 5, 5.5, 5.5

[31] Datsko, J., 1966. Material Properties and Manufacturing Processes. John Wiley & Sons, New York. 3.2.1

[32] Doener, M.F., Nix, W.D., 1986. A method for interpreting data from depth-sensing indentation instruments. J. Mater. Res. 1, 601–609. 1.1.1, 3.2.3, 5

[33] Durban, D., Baruch, M., 1976. On the problem of a spherical cavity in an infinite elasto-plastic medium. J. Appl. Mech. December, 633–638. 7

[34] Eason, G., Shield, R. T., 1960. The plastic indentation of a semi-infinite solid by a perfectly rough punch. ZAMP, 11, 33. 3.3

[35] Elmustafa, A.A., Eastman, J. A., Rittner, M. N., Weertman, J. R., Stone, D. S., 2000. Inden-tation size effect: large grained aluminum versus nanocrystalline aluminum-zirconium alloys. Scripta Mater. 43, 951–955. 7, 7

[36] Elmustafa, A.A., Stone, D.S., 2002. Indentation size effect in polycrystalline F.C.C. metals. Acta Mater. 50, 3641–3650. 4, 5.5, 7, 7

[37] Elmustafa, A.A., Stone, D.S., in press. Mater. Sci. Engng. A. 6.4

[38] Follansbee, P.S., Sinclair, G.B., 1984. Quasi-static normal indentation of an elasto-plastic half-space by a rigid sphere-I. Analysis. Int. J. Solids Struct. 20, 81–91. 6

[39] Giannakopoulos, A.E., Larsson P.-L., Vestergaard R., 1994. Analysis of Vickers indentation. Int. J. Solids Struct. 31, 2679–2708. 1.1.1, 1.1.2, 3.1.1, 3.3, 3.3, 4, 4.1, 4.1, 5.5, 6, 7.2

[40] Hardy, C., Baronet, C.N., Tordion, G.V., 1971. The elasto-plastic indentation of a half-space by a rigid sphere. Int. J. Num. Meth. Engng. 3, 451–462. 6

[41] Miscellaneous papers by H. Hertz. Eds. Jones and Schott, London, Macmillan 1996. 1.1, 1.1.2, 3.1.2

[42] Hill, R., 1950. The mathematical theory of plasticity. Oxford University Press, New York. 1.1, 1.1.2, 1.1.2, 1.1.2, 1.1.2, 5.1, 5.1, 6.2.3, 7.1.1, 7.1.1, 7.1.1, 7.1.1, 7.1.1, 7.1.1, 7.1.2, A.1, A.1.2, A.1.2

[43] Hill, R., Storåkers, B., Zduneck, A.B., 1989. A theoretical study of the Brinell hardness test. Proc. R. Soc. Lond. A423, 301–330. 1.1, 1.2.1, 1.2.1, 1.2.1, 1.2.1, 5.3, 6

[44] Hirst, W., Howse, M.G.J.W., 1969. The indentation of materials by wedges. Proc. R. Soc. Lond. A311, 429. 1.1.2, 4.2, 5.1

[45] Huang, Y., Xue, Z., Gao, H., Nix, W.D., Xia, Z.C., 2000. A study of microindentation hardness tests by mechanism-based strain gradient plasticity. J. Mater. Res. 15, 1786–1796. 7, 7

[46] Johnson, K.L., 1985. Contact mechanics. Cambridge University Press, London. (document), 1.1, 1.1.1, 1.5, 1.6, 1.1.2, 1.7, 1.2.1, 3.3, 5.3, 6, 6.2.3

[47] Johnson, K.L., 1970. The correlation of indentation experiments. J. Mech. Phys. Solids. 18, 115–126. 1.1, 4.2, 5.1, 5.1, 7, 7, 7.4.1

[48] King, R.B., 1987. Elastic analysis of some punch problems for a layered medium. Int. J. Solids Struct. 23, 1657–1664. 1.1.2

[49] Kramer, D., Huang, H., Kriese, M., Robach, J., Nelson, J., Wright, A., Bahr, D., Gerberich, W.W., 1999. Yield strength predictions from the plastic zone around nanocontacts. Acta Mater. 47, 333–343. 7, 7

[50] Larsson, P.-L., Giannakopoulos, A.E., Söderlund, E., Rowcliffe, D.J., Vestergaard, R., 1996. Analysis of Berkovich indentation. Int. J. Solids Struct., 33, 221–248. 1.1.1, 1.1.2, 4, 4.1, 5.5, 6

[51] Larsson, P.-L., 2001. Investigation of sharp contact at rigid-plastic conditions. Int. J. Mech. Sci. 43, 895–920. 1.1.1, 1.1.2, 1.2.1, 4, 4.1, 6

[52] Lee, C.H., Masaki, S., Kobayashi, S., 1972. Analysis of ball indentation. Int. J. Mech. Sci. 14, 417–426. 6

[53] Li, H., Bradt, R.C., 1993. The microhardness indentation load/size effect in rutile and cassiterite single crystals. J. Mater. Sci. 28, 917–926. 4, 6.4, 7, 7

[54] Li, H., Ghosh, A., Han, Y.H., Bradt, R.C., 1993. The frictional component of the indentation size effect in low load microhardness testing. J. Mater. Res. 8, 1028–1032. 6.4

[55] Lockett, F.J., Indentation of a rigid-plastic material by a conical indenter. J. Mech. Phys. Solids, 11, 345. (document), 1.1.2, 1.1.2, 1.7, 4.1

[56] Lubliner, J., 1990. Plasticity theory. Macmillan Publishing Company, USA. 7, 7.1.1, 7.1.1, 7.1.1, 7.1.1, 7.1.1, 7.1.2, A.1, A.1.1, A.1.2

[57] Malvern, L. E., 1969. Introduction to the mechanics of a continuous medium. Prentice-Hall Inc., USA. A.1, A.1.2, A.1.2, A.1.2

[58] Marsh, D.M., 1964. Plastic flow in glass. Proc. R. Soc. Lond. A279, 420. 1.1.2, 4.2, 5.1

[59] Mata, M., Anglada M., Alcalá, J., 2002a. Contact deformation regimes around sharp indentations and the concept of the characteristic strain. J. Mater. Res. 17, 964–976.

[60] Matsuda, K., 2002. Prediction of stress-strain curves of elastic-plastic materials based on the Vickers indentation. Philos. Mag. A 82, 1941–1952. 5

[61] Matthews, J.R. Indentation hardness and hot pressing. Acta Met., 28, 311. 1.1.1, 5.3

[62] Mesarovic, S., Fleck, N., 1999. Spherical indentation of elastic-plastic solids. Proc. R. Soc. Lond. A. 455, 2707–2728. 1.1, 1.1.2, 1.2.1, 1.2.1, 6

[63] Mulhearn, T.O., 1959. The deformation of metals by Vickers-type pyramidal indenters. J. Mech. Phys. Solids. 7, 85–96.

[64] Norbury, A.L., Samuel, T., 1928. The recovery and sinking-in or piling-up of material in the Brinell test. J. Iron Steel Inst. 17, 673. 1.2.1, 5.3

[65] Oliver, W.C., Pharr, G.M., 1992. An improved technique for determining hardness and elastic modulus using load and displacement sensing indentation experiments. J. Mater. Res. 7, 1564–1583. 1.1.1, 1.1.1, 3.2.3, 3.3, 5

[66] Puech, P., Pinel, S., Jasinevicius, R.G., Pizani, P.S., 2000. Mapping the three-dimensional strain field around a microindentation on silicon using polishing and Raman spectroscopy. J. Appl. Phys. 88, 4582–4585. 7, 7

[67] Randall, N.X., 2002. Direct measurement of residual contact area and volume during the nanoindentation of coated materials as an alternative method of calculating hardness. Philos. Mag. A 82, 1883–1892.

[68] Samuels, L.E., Mulhearn, T.O., 1957. An experimental investigation of the deformed zone associated with indentation hardness impressions. J. Mech. Phys. Solids. 5, 125–134. 7

[69] Sawa, T., Tanaka, K., 2001. Simplified method for analyzing nanoindentation data and evaluating performance of nanoindentation instruments. J. Mater. Res. 16, 3084–3096. 1.1.1, 3.2.3, 3.2.3

[70] Sneddon, I.N., 1965. The relation between load and penetration in the axisymmetric Boussinesq problem for a punch of arbitrary profile. Int. J. Engng. Sci. 3, 47–57. 1.1, 1.1.1, 1.1.1, 1.1.2, 3.1.2

[71] Söderlund, E., Rowcliffe, D.J., 1994. Analysis of penetration curves produced by depth-sensing indentation systems. J. Hard Mater., 5, 149–177. 1.1.1

[72] Storåkers, B., Biwa, S., and Larsson, P.-L., 1997. Similarity analysis of inelastic contact. Int. J. Solids Structures 34, 24, 3061-3083. 1.2.1

[73] Tabor, D., 1951. Hardness of Metals. Claredon Press, United Kingdom. 1.1.2, 1.1.2, 1.2.1, 3.3, 3.3, 4, 6.1.1, 7.1.2

[74] Tunvisut, K., O'Dowd, N.P., Busso, E.P., 2001. Use of scaling functions to determine mechanical properties of thin coatings from microindentation tests. Int. J. Solids Struct. 38, 335–351. 5, 5.5

[75] Tunvisut, K., Busso, E.P., O'Dowd, N.P., Brantner, H.P., 2002. Determination of the mechanical properties of metallic thin films and substrates from indentation tests. Philos. Mag. 82, 2013–2029.

[76] Venkatesh, T.A. , Van Vliet, K.J., Giannakopoulos, A.E., Suresh, S., 2000. Determination of elasto-plastic properties by instrumented sharp indentation: guidelines for property extraction. Scripta Mater. 42, 833–839. 1.1.1

[77] Woodcock, C.L., Bahr, D.F., 2000. Plastic zone evolution around small scale indentations. Scripta Mater. 43, 783–788. 7, 7

[78] Xu, Z.-H., Rowcliffe, D., 2002. Method to determine the plastic properties of bulk materials by nanoindentation. Philos. Mag. A 82, 1893–1902. 5

[79] Yoshioka, M., 1994. Plastically deformed region around indentations on Si single crystal. J. Appl. Phys. 76, 7790–7796. 7, 7

[80] Yu, W., Blanchard, J.P., 1996. An elastic-plastic indentation model and its solutions. J. Mater. Res., Vol. 11, No. 9, 2358–2367. 1.1.2, 4.1